Master's thesis

NTNU
Norwegian University of Science and Technology
Faculty of Natural Sciences
Department of Materials Science and Engineering

Silje Nornes Bryntesen

# Synthesis of NMC111 cathodes for Lithium-ion batteries

## The effect of Chloride and Atmospheric conditions

Master's thesis in Chemical Engineering
Supervisor: Hilde Lea Lein
June 2019

NTNU
Norwegian University of
Science and Technology

Silje Nornes Bryntesen

# Synthesis of NMC111 cathodes for Lithium-ion batteries

## The effect of Chloride and Atmospheric conditions

Master's thesis in Chemical Engineering
Supervisor: Hilde Lea Lein
June 2019

Norwegian University of Science and Technology
Faculty of Natural Sciences
Department of Materials Science and Engineering

NTNU
Norwegian University of
Science and Technology

# Preface

This thesis has been completed in partial fulfillment of the requirements for the degree of Master of Science in Chemistry at NTNU. It has been a project under the Department for Materials Science and Engineering over the course of three years. All experiments in this thesis are developed and preformed by the author.

The author expresses her sincere gratitude to all contributors at the Department of Materials Science and The Functional Materials and Materials Chemistry Research Group (FACET) for being a part of such an inspiring group, and for all valuable inputs and discussions during project meetings. In particular, I would like thank my supervisor Hilde Lea Lein for her excellent guidance the last months of my work. I would also like to thank Fride Vullum-Bruer for welcoming me into the Department of Materials Science and Engineering and for her support and guidance throughout the years of this thesis. Another thank should be dedicated to Glencore Nikkelverk for providing chemicals and Ph.D. Senior Specialist Oluf Bøckman for the collaboration and enthusiasm towards this project. I am utterly grateful for the complete understanding and patience these people showed, which allowed me to finish this work in my own time.

Truly valuable help was received from Postdoctoral Fellow Nils P. Wagner with his hands on lab experience and excellent knowledge in electrochemistry. Moreover, PhD candidate Elise Ramleth Østli is sincerely thanked for informative discussions related to the electrochemical analysis. My fellow student Hans Olav Meløy deserves a thank you for fruitful discussions, help with BET measurements and for generally spreading enthusiasm in the lab.

On a personal level, I would like to thank my friends and colleagues at NTNU, who has made this journey the best so far. A special thanks is also devoted to my family, who has been supportive throughout the six years of my study. Lastly, to my Tyler Gene Harrison, thank you for all the motivational speeches and cups of coffee you have provided me with the last year.

*Silje Nornes Bryntesen*
*28th of May 2019*

# Abstract

Li-ion batteries (LIBs) with high energy density are dependent on the powder properties of the active cathode materials. These intrinsic and extrinsic powder properties are influenced by the synthesis conditions. Production of the newly commercialized $LiNi_{1/3}Co_{1/3}Mn_{1/3}O_2$ (NMC111) cathode material should be simple and cheap, but usually requires strict control of conditions, such as atmospheres and precursors.

In cooperation with Glencore Nikkelverk, nickel- and cobalt chloride solutions ($NiCl_2$ and $CoCl_2$) was tested as precursors for the synthesis of electrochemical active NMC111 powders. Untraditional powder synthesis routes in air-atmosphere based on a hydroxide co-precipitation method and a hydrothermal method was introduced. These were compared to powders synthesized from traditional co-precipitation route in inert nitrogen ($N_2$) atmospheres. The effect of chloride (Cl) precursors were also investigated. The crystal structure and crystal size of prepared active powders were characterized by X-ray diffraction (XRD) and analyzed through Rietveld refinements. Morphology and particle size were estimated using Scanning Electron Microscopy (SEM). Calculations of the surface area of particles were done by $N_2$-adsorption measurements and Brunauer-Emmett-Teller (BET) theory. The electrochemical characterization of the synthesized cathode powders was carried out on coin cells using Li-metal anodes. The resistance of the cells was analyzed with an Electrochemical Impedance Spectroscopy (EIS). The cycling stability was compared to currently outperforming NMC111 based cathodes and commercial demands, followed by suggestions for further optimization.

Differences in powder characteristics resulted in different electrochemical activities. The presence of Cl anions ($Cl^-$ in solutions during co-precipitation of the hydroxide phase had a clear impact on size, morphology and surface area. All powders synthesized in inert atmospheres obtained phase pure layered NMC111. These showed the best overall electrochemical performance, particularly in terms of initial discharge capacity and average coulombic efficiency over 80 cycles ($\sim$99.3 %). Inert-synthesized powders using Aq-precursors obtained a cation mixing and an average particles size (APS) of 7.8 % and 200 nm, respectively; this was higher and lower relative those using Cl-precursors (2.4 % and 400 nm, respectively). The latter displayed the highest initial discharge capacity (143 mAh/g at 0.2C) and capacity retention after 80 cycles (76 %). This should be ascribed to its relatively low cation mixing, particle dimensions, and morphology which allowed efficient Li diffusion and stable structures during cycling. Further, all batteries showed low electrochemical performances compared earlier reported NMC111 materials.

The air-sensitivity during co-precipitation reaction was found to be significant. No pure phased NMC111 powders were obtained in presence air due to manganese (Mn) oxidation. Secondary phases had a large impact on cycling performance as all air-synthesized powders showed extremely low initial discharge capacities. The air-synthesis that included a hydrothermal step showed less secondary phases compared to powders made in ambient pressures. It was concluded that a limited supply of oxygen suppressed the oxidation of Mn. Moreover, the Li did not completely react with the hydroxide precipitate under high pressure conditions at 120 °C, resulting in a spinel phase (58.8 %). The Li reaction however fully occurred in traditional high temperature calcination step at 480 °C. A 5 h heat-treatment at 850 °C formed areas of small particles constructed into large aggregates. Such morphology gave low surface areas and less electrolyte-contact, seen as extremely large variations in the coulombic efficiencies for each cycle. The highest phase purity of NMC111 obtained from air-synthesis combined 1) the use of Cl precursors to obtain a preferred particle size, 2) a hydrothermal step to decrease the oxygen concentration and Mn-oxidation, 3) a Li reaction in ambient pressures during calcination ensuring a complete reaction, with 4) a 15 h heat-treatment. Out of the air-synthesized active materials, this powder gave the best overall cycling performance with an initial discharge capacity of 80 mAh/g at 0.2C and capacity retention of 87 % after 80 cycles. This is however far below the expected capacities for NMC111 cathode material.

The findings and further suggestions will hopefully contribute to bringing powder synthesis using Cl precursors to the marked, enabling cheap and efficient synthesis' of batteries with high energy density, low cost, and increased safety; which is essential for a futuristic society dependent on renewable energy sources.

# Sammendrag

A kunne oppnå Li-ion batterier (LIBer) med høy energy tetthet, avhenger blandt annet pulveregenskapene til det aktive katodematerialet. Disse ekstrinsike og intrinsike egenskapene blir dannet under syntesen. For å oppnå optimale pulveregenskaper krever slik produksjon ofte streng kontroll av forholdene. To slike parametere er atmosfære og valg av forløpere.

I samarbeid med Glencore Nikkelverk, ble nikkelklorid og kobaltklorid løsninger testet som forløpere i produksjon av NMC111 katoder. En utradisjonell syntesemetode i luft ble introdusert. Denne var basert på en utfellingsmethode og en hydrotermisk metode. Effekten av klorid (Cl) og luft under utfellingssteget ble undersøkt ved å sammenlikne resultatene med en tradisjonell utfellingsmetode, som tok i bruk vandige forløperløsninger og en inert atmosfære. Krystallstruktur og krystallstørrelse ble undersøkt ved hjelp av røntgendiffraksjon (XRD), og videre analysert ved hjelp av Rietveld raffinering. Morfologi og partikkelstørrelse ble undersøkt ved hjelp av sveipelektronmikroskopi (SEM). Overflatearealet ble beregnet ved hjelp av nitrogen adsorpsjon og Brunauer-Emmett-Teller (BET) teori. Katodenes elekrokjemiske egenskaper var testet ved å lade og utlade halvceller galvanostatisk. Motstanden i halv-cellene ble målt ved å bruke elektrokjemisk impedans spektroskopi (EIS). Syklingsstabiliteten ble sammenliknet med kommersielle NMC111 katoder, og metoder for optimalisering ble introdusert.

Ulike pulveregenskaper resulterte i varierende elektrokjemiske aktiviteter. Partikkelstørrelse, morfologi og overflatearealet ble tydelig påvirket av Cl anioner i løsningen under utfellingen. Alle pulverne som ble syntetisert i inert atmosfære viste en fase-ren NMC111. Disse viste også høyes initial utladningskapasitet, og høyest gjennomsnittlig colombisk effektivitet over 80 sykler (99.3 %). Inert-syntetiserte pulver som brukte standard vandige løsninger, ga en høyere kation miksing og en mindre gjennomsnittlig partikkelstørrelse (7.8 % og 200 nm) relativt til pulver laget med Cl-forløpere (2.4 % og 400 nm). Den sistnevnte viste høyest initial utladningskapasitet (143 mAh/g ved 0.2C) og bedre bevaring av kapasiteten etter 80 sykler (76 %). Dette er grunnet pulverets relativt lave kation miksing, partikkel dimensjoner og morfologiske egenskaper. Dette promoterer Li diffusjon og stabile strukturer under den elektrokjemiske syklingen. Allikevel hadde alle celler lave elektrokjemiske egenskaper sammenliknet med tidligere rapporterte NMC111 katoder.

Alle prøvene som ble syntetisert i luft var sensitive for Mn oksidasjon, og ingen av dem oppnådde en faseren NMC111. Sekundærfaser hadde en stor innvirkning på syklingen, da alle disse viste seg å oppnå lav initial kapasitet. Ett hydrotermisk steg ble inkludert i en av syntesene, og reduserte mengder sekundærfaser. Dette begrenset tilgangen på oksygen og undertrykte oksidasjonen av Mn. Videre ble det konkludert at Li ikke reagerte fullstendig med det utfelte hydroksidet under høyt trykk, ved 120 °C. En kort varmebehandling (5 timer) ved 850 °C frte til små partikler. Disse agglomererte og dannet mindre overflateareal og mindre kontakt med elektrolytten. Dette resulterte i store variasjoner i den coulombiske effektiviteten mellom syklene. De optimaliserte parameterne for syntese i luft kombinerte 1) Cl-forløpere, 2) ett hydrotermisk steg, 3) Li reaksjon i kalsineringssteget, og 4) en 15 timers varmebehandling. Dette resulterte i de beste egenskapene i henhold til faserenhet og elektrokjemisk sykling. Med en utladningskapasitet på 80 mAg/h ved 0.2C, hvor 87 % var bevart etter 80 sykler, viste den allikevel svært lavte verdier i forhold ett kommersielt NMC111 katode materiale.

Funnene og de videre anbefalingene vil forhåpentligvis bidra til økt bruk av Cl-forløpere, og muliggjøre mer miljøvennlige og mer effektive syntesemetoder av batterier med høy energi tetthet, lav kostnad og høy sikkerhet. Dette er avgjørende for ett velfungerende samfunn basert på fornybare energikilder.

# Contents

# List of Tables

# List of Figures

# Chapter 1

# Background

## 1.1 Motivation

Today, the dominant source of global energy production are fossil fuels, with crude oil, coal and natural gas being the most common. These natural resources are gradually being depleted as the demand for energy increases and equates to a large emission of by-products with $CO_2$ being the bulk. $CO_2$ contributes to the excessively high values of greenhouse gasses in the atmosphere. With environmental pollution follows ecological destruction, which has increasingly aggravated in recent years. Finding new unlimited energy sources based on clean, efficient and renewable technology has become an urgent matter. The need for a technological green shift is upon us. [1, 2]

The most common renewable energy sources includes windmills, tidal energy and photovoltaic devices. Their energy supply is discontinuous, depending on fluctuations in the availability of the energy source, and are thus often classified as intermittent energy sources. In order to build an energy-sustainable economy and prevent overcompensation of the power-grids, the energy harvested requires an intermediate power storage. [1, 3] Since the technological ability to store energy is far behind the demand for energy production, efficient energy storage is declared as a bottleneck for the green shift. Effective and sustainable storage technologies that are able to meet the energy requirements of the modern day are in high demand. Also, owing to the aim of minimizing the carbon footprint, further measures have been done by replacing gasoline powered cars with full/hybrid electrical cars (EV/BHV). [4] Consequently, the production of electric cars has expanded in recent years. Including the increasing necessity of portable electronics in everyday-life, we are currently dealing with an ever-growing demand for not only high-energy storage technology, but also smaller, lighter and safer systems. [5, 6] Already in the 90s, the Environmental Protection Agency (EPA) estimates Americans to purchase nearly 3 billion batteries each year. [7]

The main energy storage system of today is rechargeable batteries. These are uninterrupted power sources that are able to store energy in the form of chemical energy, and facilitate high energy conversion rates when needed. Further, their geometries and properties can be adjusted to fit a specific application area. The most commercialized rechargeable battery, and still predicted to be dominating portable energy storage systems for many years to come, is the lithium-ion battery (LIB).

Already in the 1970's scientist saw the potential for lithium metal (Li) as an electrode material component. [8] After only a quick peak in a chemistry book one can find the answer why. Lithium cations ($Li^+$) have one of the smallest ionic radii of any single charged ion and is the lightest elemental metal on earth. Also, Li has the lowest reduction potential with its electrode potential of -3.04 V versus the standard hydrogen electrode. [9] These factors provide Li with its high gravimetric capacity of 3859 mAh/g as well as volumetric capacity (2061 mAh/cm$^3$). However, due to safety issues concerning the use of Li as an anode, commercial LIBs do not use metallic Li, but rather graphite as the anode.

The most used LIB uses a layered $LiCoO_2$ as a cathode and graphite as an anode. This was commercialized by Sony and revolutionized the battery industry in the 1990's. [10, 11] Since then, many other cathode materials have been developed and implemented while the main anode material used is still graphite. Cobalt (Co) has a high price, toxicity, safety and ethical issues [12] which led to attempts of substituting it with other elements (Fe, Mn, Ni and Al). As a result, the now widely used $LiNi_{1/3}Co_{1/3}Mn_{1/3}O_2$ (NMC111) was introduced as a new cathode material in 2001 by Ohzuku and Makimura [13]. Since 2003, NMC111 is considered to be one of the best candidates for the positive electrode material for batteries found in hybrid electric vehicles; by Amine and co-workers [14]. Even so, electrical vehicles' driving range (150—400 km) is still far behind the traditional cars driven by the internal combustion engine (500—700 km). [15]

The green shift also forces industries such as Glencore Nikkelverk to delve into battery technology. From an industrial perspective it is interesting to research well-known battery materials such as NMC111. Chloride (Cl) containing precursors is sometimes preferred due to price, non-toxicity and availability. [16] Usually Cl solutions needs leaching, and are then made into sulphate solutions before they are used as battery precursors. [17] The direct use of Cl precursors are often avoided the synthesis of battery materials. The lack of research on such precursor materials led to the aim of this work.

## 1.2 Aim of Work

As a move towards the battery technology, Glencore Nikkelverk in collaboration with NTNU, wanted to test their nickel- and cobalt chloride solutions ($NiCl_2$ and $CoCl_2$, respectively) as precursors for cathode materials. Thus, the aim of this work is to investigate the influence of Cl precursors on powder properties and battery performance. To reach this goal, the well-known co-precipitation synthesis of NMC111 in inert atmospheres is used. The precursors morphology, phase purity and electrochemical performance are compared to pure standard aqueous(Aq)-based solutions from Sigma Aldrich.

A sub-goal is to investigate the possibilities for making a phase pure NMC111 through a untraditional co-precipitation of synthesis in air. Manganese is highly oxidizing in the presence of oxygen. This thesis aim to give an understanding of how the oxygen level affect the formation an active NMC111 phase and how this ultimately affect the battery performance. An optimization of the air synthesized active NMC powder is then tested in terms of phase purity, morphology and electrochemical performance. This is done by varying the pressure conditions during the Li-reaction and length of heat-treatments. The synthesis method of active NMC111 powders is then appraised in terms of powder characteristics and electrochemical performances.

# Chapter 2

# Introduction

## 2.1 Fundamentals of Rechargeable Batteries

A battery is an electrochemical cell that converts chemical energy from redox-reactions into electrical energy. It contains a separator, an electrolyte, and two electrodes connected through an external load circuit. The electrolyte conducts ions between the electrodes and are an electric insulator. The separator prevents short-circuiting of the cell by physically separating the electrodes. The electrodes are named according to the redox-reactions occurring. In a primary battery, the galvanic cell convention, defines the cathode as the electrode where reduction occurs, whereas the anode is where the oxidation takes place. A secondary battery is rechargeable and the electrode terms become relative to the direction of the current. Upon discharge, the anode is oxidized and the cathode is reduced, while it is opposite during charge. This report applies fixed terms on electrodes derived from their state of discharge.

### 2.1.1 Working principle of Li-ion batteries

The cell configuration of a LIB often consists of two layered electrodes, an electrolyte, and a separator, as shown in figure 2.1. The electrolyte is normally a solution of Li salt mixed in an organic solvent seen in figure 2.2, and the anode is usually graphite based. The cathode, being the source of $Li^+$ ions ($Li^+$), is normally a transition metal (TM) oxide ($LiMO_2$ where M= Co, Mn, Ni) mixed with a polymeric binder and an electrically conductive agent. In such a cell, the operating voltage is approximately 3.7 V. [18] The anodic reaction 2.2 cathodic reaction 2.1 and total chemical reaction 2.3 converting chemical energy to electric energy in a conventional LIB is written as [6]:

$$\text{Cathode reaction} \qquad Li^+ + CoO_2 + e^- \xrightleftharpoons[\text{Charge}]{\text{Discharge}} LiCoO_2 \tag{2.1}$$

$$\text{Anode reaction} \qquad LiC_6 \xrightleftharpoons[\text{Charge}]{\text{Discharge}} Li^+ + C_6 + e^- \tag{2.2}$$

$$\text{Total reaction} \qquad CoO_2 + LiC_6 \xrightleftharpoons[\text{Charge}]{\text{Discharge}} LiCoO_2 + C_6 \tag{2.3}$$

During discharge, $Li^+$ are extracted from the graphite anode. An equal number of electrons are given to an outer circuit connected to the electrical load. The electrolyte carries $Li^+$ towards the cathode surface where it is intercalated into the structure. The TMs in the $MO_2$ material are simultaneously reduced to ensure charge neutrality. This way, the $LiMO_2$ material is reduced (cathode) and the graphite is oxidized (anode) during discharge. During charge, an external potential is applied to initiate the reverse reaction. The $Li^+$ deintercalates from the cathode while the TMs are oxidized. $Li^+$ diffuse towards the anode, where they intercalate and are reduced back to Li. Hence, electrical energy is stored in the form of chemical potential. [5]

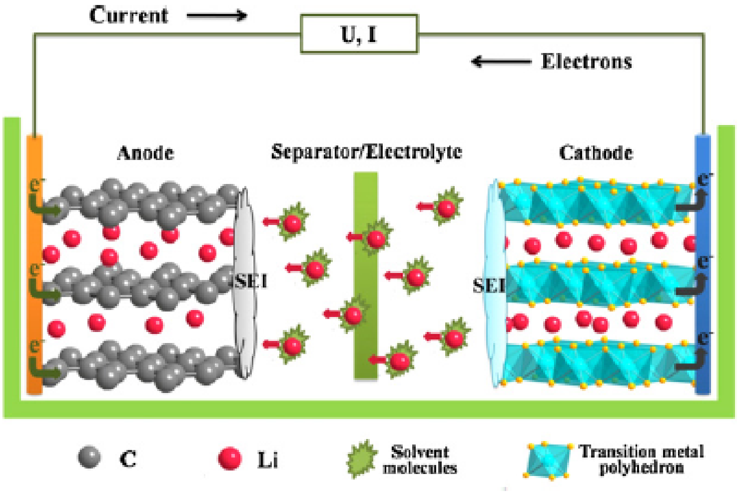

**Figure 2.1:** The configuration of the first LIB cell, with a graphite anode, $LiCoO_2$ cathode and Li conducting electrolyte. The working principle is shown in the state of charge. [19]

### 2.1.2 Terminology and Figures of Merit

There are some essential terms within the world of electrochemistry that should be defined to ease the readability of this thesis. According to Goodenough *et. al.* [20], some of the most important terms to interpret are:

- Cell voltage
- Specific capacity
- Energy density (gravimetric and volumetric)
- Rate capability
- C-rate
- Cycle life
- Shelf life
- Safety

The *cell voltage* or cell potential (V) is a result of a potential difference between two electrodes, and is a relative term. In the half-cell LIB, the redox potential of the cathode transition metals versus Li/Li$^+$ dictates the cell potential. [21] Therefore, the voltages mentioned in most LIB research, as well as here, are relative to Li/Li$^+$. The operating voltage refers to a fixed voltage range a battery can work within. For safety, an upper and lower limit called the cut-off voltage is set for the cell potential during cycling. This restricts the amount of Li$^+$ (de)intercalating the electrodes and prevent unstable structures.

Capacity defines the amount of electrical charge stored in a battery material and/or in an entire battery electrode. Capacity is measured in coulombs and usually expressed in Ah (Ampere hour). 1 Ah is 3600 coulombs, hence the capacity of one mole electroactive material that transfers one electron per process, is 1 F or 26.8 Ah. However, the practical world of energy storage and conversion uses the term practical- and theoretical *specific capacity*. The theoretical specific capacity (C$_{s,t}$) of a compound is calculated using the molecular weight (M$_w$) of active material and the number of electrons (n) contributing in the redox-reactions by the following equation [21]:

$$C_{s,t} = \frac{nF}{M_w}[mAh/g] \tag{2.4}$$

where F is the Faraday constant equal to 26 801.5 mAh/g. The specific capacity of the LIB (C$_B$)is determined by both considering the specific capacity of the anode, C$_A$ and the cathode C$_C$ by the following equation [20]:

$$C[mAh/g] = \frac{C_A C_C}{C_A + C_C} \tag{2.5}$$

The practical specific capacity (C$_{s,p}$) is the actual capacity the battery can deliver. It can be calculated using information from a voltage-time curve from galvanostatic cycling test and equation [21]:

$$C_{s,p} = \frac{iAt_c}{3600M_w}[mAh/g] \tag{2.6}$$

where i is current density ($Am^{-2}$), A is the area ($m^{-2}$), $t_c$ is the time in seconds (s) until cut-off potential, and $M_w$ is the molecular weight (g/mol). The practical capacity also depends on electrode design, cell configuration, kinetic limitations of the electrochemical reactions, temperature conditions, and C-rate. [21]

The energy density is the density at which energy are able to be stored, and should be maximized both per weight (gravimetric energy density) and per volume (volumetric energy density). A batterys operating potential (V) and specific capacity ($C_s$) are directly related to energy density (E) [22]:

$$E = C_sV \tag{2.7}$$

Consequently, we can improve the energy density of a LIB by increasing the capacity of the anode and/or the cathode. [21] Equation 2.7 reveals that another way of increasing density is finding materials with large potential differences, hence high operating potentials. Since $Li^+$ has a low potential it is necessary with cathode materials able to work at high voltages versus $Li/Li^+$. In a completely charged battery, the chemical energy is stored as an electrochemical potential ($\mu$). The difference in electrochemical potential of the anode $\mu_A$and the cathode ($\mu_C$) results in an open circuit voltage ($V_{OC}$) [20]:

$$V_{OC} = \frac{(\mu_A - \mu_C)}{e} \tag{2.8}$$

where e is the elementary charge.

Upon charge and discharge, the anode or cathode will experience a certain degree of polarization ($\eta$). A higher $\eta$, indicates that the (de)intercalation process of $Li^+$ becomes more difficult. The output voltage ($V_{Dis}$) will be reduced while the input voltage ($V_{Ch}$) increase according to [20]:

$$V_{Ch} = V_{OC} + \eta(I_{Ch}, q) \tag{2.9}$$

$$V_{Dis} = V_{OC} - \eta(I_{Dis}, q) \tag{2.10}$$

This effect depends on the current during charging ($I_{Ch}$) and discharging ($I_{Dis}$), and the internal battery resistance which are related to the state of charge (q). [20]

The *shelf life* means how long a battery can be stored without usage and is dependent on storage temperature, degradation mechanisms and stability of the battery. The *cycle life* is defined as the total number of charge and discharge cycles the cell can sustain. For an electric vehicle battery, the cycle life is the number of cycles that deliver above 80 % of initial reversible capacity. [23] This is usually described by cycling stability, cyclability, capacity retention and reversibility, which evidently refers to the same. The two former are general terms, whereas the capacity retention is usually referring to the percentage of initial capacity remaining after a certain amount of cycles. [20] LIBs coulombic efficiency

(CE) is a common figure of merit to indicate of how many $Li^+$ the LIB is able to utilize from the previous charge and describes the capacity fade during a cycle [24]:

$$CE = \frac{C_{dis}}{C_{ch}} \times 100 \tag{2.11}$$

A deviation of CE = 100% denote a irreversible capacity loss. [24]
The *rate capability* describes the difference in capacity when cycled at high or low current hence a short or long charge time. A high rate capability results in high charge/discharge rates. High charge rates are accomplished when applying high currents which shorten the cycle. However, fast charging will reduce the specific capacity due to kinetic limitations causing a more rapid cell degradation. The redox reactions and ionic diffusion should, therefore, be fast. A combination of a high electronic- and ionic conducting electrodes with a high ionic conducting electrolyte provide high reaction rates.

The *C-rate* is a parameter governing the rates of charge and discharge. It sets what amount of current the battery will be provided with or deliver, during a certain time. The capacity is commonly rated at 1C. This means that a fully charged battery with 100 % energy efficiency, rated at 1Ah could provide 1A for 1 hour. Essentially, this means that a battery that is discharged at 1C will be fully discharged in 1 hour. [21]

Thermal runaway is the phenomenon that has caused LIBs their well-known explosions. At a critical temperature, the materials in the battery start to break down exothermically. When heat is generated faster than its ability to escape, this starts an unstoppable runaway reaction and the electrolyte will eventually ignite. [25]

The importance of these parameters are dependent on the battery application area. For stationary batteries used in, for example, electric grids that will be used over thousands of cycles, optimization of the cycle life, shelf life and efficiency are of importance. Portable batteries, however, should be safe to use, and small in terms of weight and volume since a high energy density is preferred. For all batteries, it is of interest to have environmentally friendly materials with low costs, processed in an efficient way.

## 2.2 Li-ion Battery Components

A battery are made of three components: the electrolyte, anode and cathode. Each should be carefully advised relative to the others before assembling them into a battery system.

### 2.2.1 The Electrolyte

A list of minimal requirements for an electrolyte made by Xu *et. al.* [26] states that it must:

- be a good ionic conductor and electronic insulator, to transport $Li^+$ and to separate for ionic- and electronic transport.

- have a wide stability window shown in figure 2.3 to prevent electrolyte degradation.
- be inert to the other cell components to ensure a stable system.
- be robust against various abuses, such as electrical, mechanical, or thermal.
- consist of environmentally friendly components, synthesized in a sustainable way.

The electrolytes that fulfill these requirements in a LIB is usually based on non-aqueous or aprotic solvents with a supporting electrolyte responsible for charge carrying. [27] A typical composition is lithium hexafluorophosphate ($LiPF_6$) salts dissolved in a mixture of the organic carbonates presented in figure 2.2. [28] Commercial electrolytes also contain various additives that work as flame inhibitors or stabilizing agents and can increase the electrolyte stability window. [6]

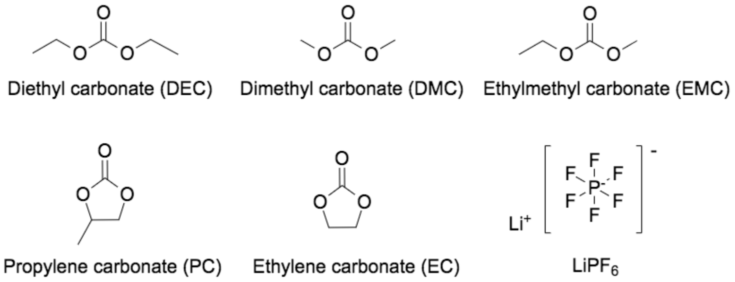

**Figure 2.2:** Overview of the common electrolytes. Adopted from Goodenough and Etacheri [6, 27].

### The Stability Window

The stability window of an electrolyte describes at what potentials an electrolyte can work without facing any crucial side reactions. Such a window is defined between the energy difference from HOMO to LUMO shown in figure 2.3. The batterys operating potential must lay within these limits. This means that the chemical potential of the anode ($\mu_A$) and the cathode ($\mu_C$) must be lower than LUMO and higher than HOMO of the electrolyte, respectively. If $\mu_C$ is below HOMO, the electrolyte is oxidized at the cathode. Likewise, if $\mu_A$ is above LUMO energy, the electrolyte will face a reduction on the anode. Such electrode/electrolyte reactions cause formations of a cathode interphase layer (CEI) and, more importantly, the well-known solid electrolyte interphase (SEI). [22]

### The SEI formation

The electrolytes shown in figure 2.2 has oxidation- and reduction potentials vs. $Li^+/Li$ close to 4.7 V and 1.0 V, respectively. However, the intercalation potential of $Li^+$ into a graphite anode lays between 0 V to 0.25 V vs. $Li^+/Li$. [27] Thus, the intercalation of $Li^+$ during charging occur at potentials outside the stability window of the electrolyte. The electrolyte is decomposing on the anode surface, forming the passivizing SEI layer. The

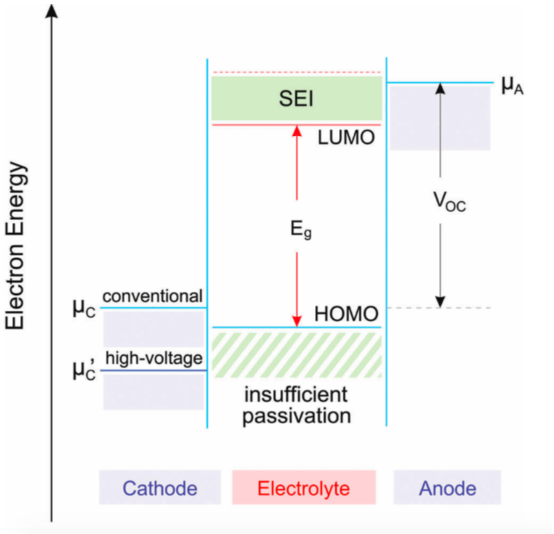

**Figure 2.3:** The stability window of a electrolyte ($E_g$) determined relative to the chemical potentials of the cathode ($\mu_C$) and anode ($\mu_A$) HOMO is he highest occupied molecular orbital whereas LUMO is the lowest unoccupied orbital. [20]

SEI formation has positive and negative side effects. First, SEI formation consumes $Li^+$ which increase internal resistance and reduce the capacity by reducing the amount of available $Li^+$. Consumption of Li in such side reactions may cause irreversible capacity losses as not enough Li is present to participate in the cycling. Internal resistance introduces a potential drop (IR drop) between the charge and discharge states. IR drop decreases energy efficiency and causes heat release. [22] Second, SEI alter the initial capacity and result in a long-term capacity fade. [27] Even so, the SEI layer is considered essential in a LIB. Since $Li^+$ have a small ionic size that can diffuse through during cycling, it protects the anode against further degradation. It also minimizes the aggregation of active particles on the electrodes, thus reduce over-potential and concentration polarization. [29]

## 2.2.2 The Anode

The anode materials closest to fulfill the above-mentioned criteria can be divided into three main categories depending on their reaction mechanism with Li/$Li^+$, namely: alloy-, conversion- and intercalating materials. The two former are not yet commercialized. Conversion materials are based on TM oxides, or metals combined with either nitrides, sulfides or phosphides (MxXy, where X = S, P, N). The alloy anodes are normally based on Si, Sn, Sb, Mg or Al. [30] These have charge densities 2-5 times higher than commercialized graphite anodes. However, volume expansion/contraction (up to 300 %) [31], and irreversible capacity loss leaves them with poor cycling stability. [32]

The intercalating/de-intercalating anodes are most used anode materials. These are commonly known as graphite anodes, owing to carbons (C) low working potential vs Li/Li$^+$, low cost, and good cycle life. Silica is another highly interesting anode material that can provide an extremely high energy density. During intercalation in pure graphite anode, Li$^+$ goes through the reaction 2.2 above. Each Li$^+$ site needs 6 C atoms and the reversible capacity is restricted to 372 mAh/g. [33] The diffusion rate for Li$^+$ intercalation in graphite is lower than other carbonaceous materials, and the formation of an SEI layer is favorable. [34]

## 2.3 Cathode Materials in Li-ion Batteries

As mentioned, the cathode materials must fulfill certain requirements regarding safety, cost, lifespan, performance, specific power, and specific energy. The materials closest to fulfilling these properties inhabit layered ($LiMO_2$)[9], spinel ($LiM_2O_4$) or olivine ($LiMPO_4$) crystal structures. [12] Commercialized cathode materials are represented relative to one another in figure 2.4 and the following section will introduce some of these. [12, 35] For a cathode material, high capacity and voltage is considered above 200 mAh/g and 4 V, respectively. [35, 36]

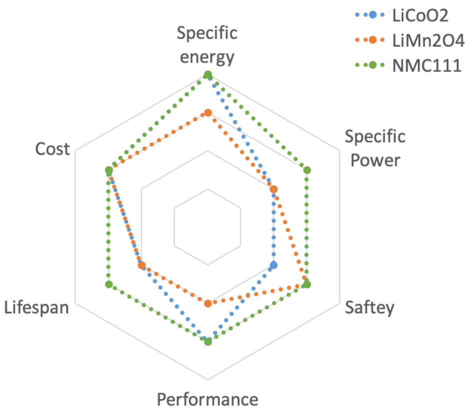

**Figure 2.4:** Overview of the most common cathodes relative properties in terms of spesific energy, spesific power, cost, safety, performance, lifespan, and cost. [35]

### 2.3.1 Spinel Oxides

Lithium manganese oxide ($LiMn_2O_4$) is a spinel-structured cathode. The structure is shown in figure 2.5. The TM cations are ordered in all layers, and Li occupy tetrahedral 8a sites.[37] Such lattice is compact and provides a high energy density.

The major issue with manganese-containing spinels is the stability when extracting a certain amount of Li. The $Mn^{3+}$ undergo redox reactions in the presence of hydrogen ions

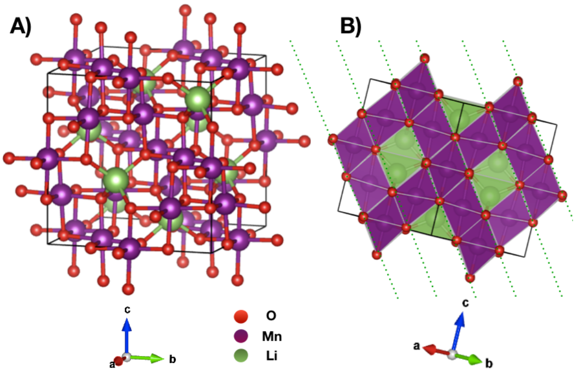

**Figure 2.5:** A) Shows the unit cell of a $LiMn_2O_4$ (LMO) crystal structure and B) a cross-section of the layers, one mixed Li and Mn and one with pure Mn. The seats for Li are shown in green, O is red and Mn is purple. The structures are made in VESTA. [38]

and form $Mn^{2+}$ and $Mn^{4+}$. $Mn^{2+}$ can dissolve from the cathode lattice into the electrolyte subsequently and deposit on the graphite anode. This will make the layer SEI layer conducting and prevent Li diffusion which is seen as severe impedance increase and capacity fade during cycling. Moreover, the practical capacity of $LiMn_2O_4$ is limited to $\sim$ 120 mAh/g at 4 V vs $Li/Li^+$ at 80 % $Li^+$ insertion/extraction. [39] The first Li intercalating will occupy the 8a tetrahedral sites shown in figure 2.5. However, the second $Li^+$ will enter the large octahedral 16c sites, corresponding to a low discharge potential plateau of 3 V. At 2.8 V, spinel structures, therefore, undergo a macroscopic structural transition from cubic spinel $LiMn2O_4$ to tetragonal spinel $Li_2Mn_2O_4$ symmetries. This is due to the JahnTeller distortion associated with the high spin $Mn^{3+}$. [37] The transformation is recognized as the plateau found below 3 V in figure 2.6. This clearly comes with huge capacity fading but also volume expansions and should be the lower cut-off voltage. [22, 39]

Another heavily investigated spinel composition is the $LiNi_xMn_{2-x}O_4$ (LMNO). This is a high-voltage cathode with an operating potential at 4.7 V. [20] Essentially, there are two factors keeping LMNO from commercialization. First, the crystal structure can be either ordered or disordered. The former has poor electrochemical properties and the synthesis of a pure disordered phase is challenging. [12] Second, at high voltages the electrolyte decomposes which leads to safety risks. [22]

### 2.3.2 Layered Transition Metal Oxides

Today, layered $LiMO_2$ are the most commercialized LIB cathodes. They adopt a $\alpha$-$NaFeO_2$ structure with space group $R\bar{3}m$. The crystal structure is shown in figure 2.7. This is a repeating $O_3$ structure of O−Li−O−TM−O−Li−O−TM−Li along the rhombohedral $[001]$ direction ($[111]$ for spinels). [40] In a unit cell with n number of anions there are 2n tetrahedral and n octahedral sites available. A perfect $R\bar{3}m$ structure has TM

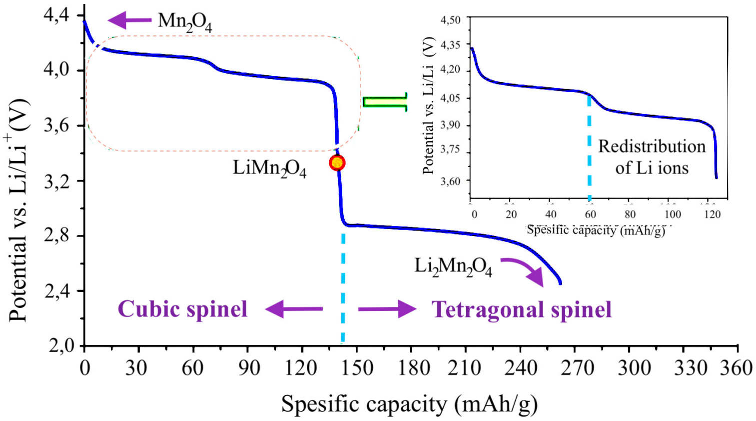

**Figure 2.6:** Specific capacity (mAh/g) are plotted against potential vs $Li^+/Li$ (V) for a lithium manganese oxide. The phase transformation between a tetragonal spinel and cubic spinel under 2.8 V is shown. [22]

sites (3a) and Li sites (3b) clearly separated in octahedral sites. [22] The 2D alternating layers of Li and $MO_2$ give a unique cycling mechanism. The main challenge of layered cathodes is to maintain a stable $MO_2$ structure during the delithiation process and a stable electrolyte at voltages above 4.3 V. [40]

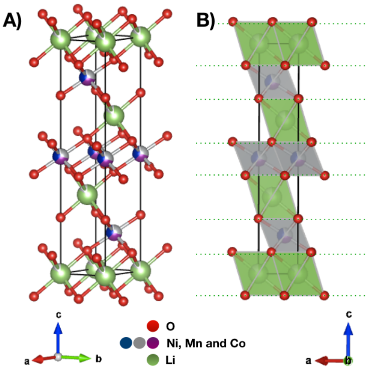

**Figure 2.7:** A) Shows the unit cell of a $LiMO_2$ crystal structure and B) a cross-section of the pure M and Li 2D layers. The seats for Li are shown in green, O is red and Mn is purple. [41] The structures are made in VESTA. [38]

Layered $LiCoO_2$ (LCO) offer a life span of only 500-1000 cycles and contains the toxic and expensive Co metal. The materials suffer from poor safety at elevated temperature in the charged state, causing the low thermal stability, shown in figure 2.10. LCO has a theoretical specific capacity of 275 mAh/g vs $Li/Li^+$. However, as figure 2.14 indicates, only 50 % of the theoretical capacity are accessible (140 mAh/g). This is explained by the electron structure shown in figure 2.8. To reach the $Co^{4+}$ state over half of the $Li^+$ must be extracted during cathode delithiation (charge). Strong repulsions develop between $CoO_2$ layers due to an overlap between the $Co^{3+/4+}$ $t_{2g}$ band and $O^{2-}$ 2p band. This causes electrons to delocalize and the high oxidation state of $Co^{4+}$ cannot be accessed without encountering chemical instability and safety concerns. [12, 39] Ni electron structure shown in figure 2.8 has less overlap, hence fully replacing Co with Ni gives a higher utilization of Li (80 %). $LiNiO_2$ is, therefore, approaching the capacity of 220 mAh/g. [40] Other challenges are however related to the $LiNiO_2$ materials. Stochiometry difficulties during powder synthesis, structural changes, and safety issues induced by an oxygen release in charged state [42] and thermal runaway are some. [39] Most of these concerns are influenced by a well-known phenomenon found in Ni-rich materials called cation mixing. [40]

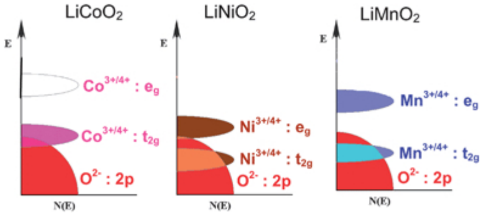

**Figure 2.8:** Electron-structure of the three different layered $LMO_2$ structures where M = Ni, Co or Mn. [39]

Cation mixing involves cations disordering between TM sites (octahedral 3a site) and Li sites (octahedral 3b site). $Ni^{3+}$ is unstable according to crystalfield theory. [40] Therefore Ni has tendency to be $Ni^{2+}$ rather than $Ni^{3+}$ in the FCC octahedral site. The ionic radius of $Ni^{2+}$ (0.69 Å) is similar to the ionic radius of $Li^+$ (0.76 Å). Owing to this similarity, $Ni^{2+}$ can occupy the 3b Li sites shown in figure 2.9. The presence of TM in the Li layer leads to a partial destructive interference in the (003) plane and increased constructive interference of the (104) plane. The degree of cation mixing can, therefore, be detected with Xray diffraction analysis. Large amounts of cation mixing are seen as a decrease in intensity of the (003) peak, and an intensity increase for the (104) peak. [43] As a result, the degree of cation mixing is inversely proportional to the intensity ratio of the (003)/(104) peaks. [40] Ni-rich cathodes usually have a higher degree of cation mixing. A restricted amount of Ni in the structure is therefore beneficial although it is the main electrochemical active species.

## 2.4 Lithium Nickel Manganese Cobalt Oxide (NMC)

The unstable structures of $LiNiO_2$ and $LiCoO_2$ can be stabilized by adding Mn into the TM layers. This idea gave rise to the now commercialized NMC cathode. In addition to being a structure stabilizer, Mn is more abundant and less toxic compared to Ni and Co and it will reduce the cost. However, being in the form of $Mn^{3+}$ it is electrochemically inactive. This will lower the theoretical capacity. Hence, Ni, Mn, and Co contribute with different

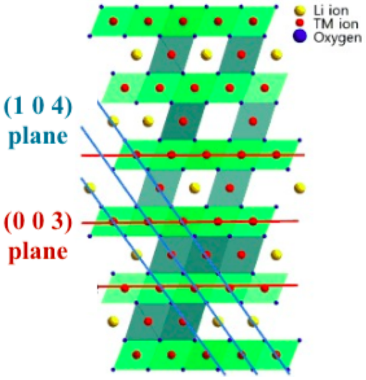

**Figure 2.9:** Partially cation mixed phase of Li and Ni atoms with labelling of (003) and (104) planes. Li sites are yellow, Ni red and coordinated O atoms dark blue. [40]

beneficial values to the battery shown in figure 2.10. While Mn stabilizes the structure and increases thermal stability, Co stabilizes the TM layers, whereas Ni increases the capacity. The ratio of the three TMs will give quite different properties without changing the crystal structure of the layered NMC.

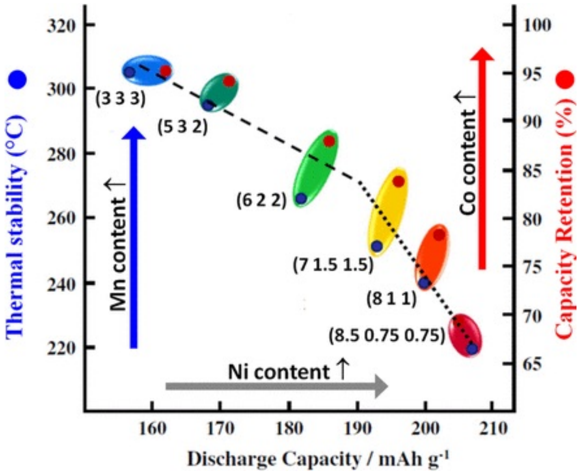

**Figure 2.10:** A map of the NMC materials discharge capacity(black), thermal stability(blue), and capacity retention(red). The content is shown in brackets in the following order: (Ni Mn Co). Reproduced from [36] and inspired by [44].

Noh *et. al.* [44], compared different ratios of x,y and z in the NMC ($Li(Ni_xCo_yMn_z)O_2$) structure and concluded that a moderate content of each TM (NMC111) was the most promising in terms of operating voltage, rate capability, cycle-ability, thermal- and structural stability, and discharge capacity. [45, 46] A moderate content of Mn and Ni will suppress cation mixing and stability issues while keeping a relatively high capacity.

### 2.4.1 The NMC111

The TMs are in the state of $Co^{3+}$, $Ni^{2+}$ and $Mn^{4+}$. As seen in equation 2.13, Co contributes with $1e^-$ and $Li^+$ per Co site. Ni can obtain multiple oxidation states and according to equation 2.12 offer $2e^-$ per metal site. Ni is, therefore, the main electrochemical active species of NMC111 and provides its high practical specific capacity of $\sim$ 200 mAh/g. [36]. This is explained by the electron structure of Ni in figure 2.8. Ni orbitals are at low energy states relative to the other TMs, making it adaptable to most electrolyte stability windows. Hence, the 2.12 reaction can occur at a relatively higher voltage (4.4 V) without any crucial side reactions.[47] A high voltage will allow more reactions to occur, which is seen as the high capacity to high voltage trend reported by Lee in 2004 [48]. The discharge capacity of NMC111 increases from 159 mAh/g when cycling between 2.8 - 4.3 V, to 177 mAh/g when cycling between 2.8 - 4.5 V. It is also reported that much of capacity obtained when cycling above 3 V is partly from oxygen reactions. [49]

$$Ni^{2+} \rightleftharpoons Ni^{4+} + 2\,e^- \tag{2.12}$$

$$Co^{3+} \rightleftharpoons Co^{4+} + 1\,e^- \tag{2.13}$$

Aging mechanisms seen NMC cathodes influence each other and are very complex. [50] Among these, the most important is related to:

- Active mass dissolution (usually of $Mn^{2+}$) [51–53]
- Formation of a cathode-electrolyte interface (CEI) between on the cathode surface during the initial cycles [35, 54–57]
- Oxidative decomposition of electrolyte at high voltages [47, 49]
- Irreversible structural reconstruction (such as cation migration) and phase transformations [41]
- Microstructure cracking during cycling [58, 59]
- Cation mixing [42, 47, 60]

A consequence of aging mechanisms will be seen as fading of electrochemical performance. More specifically it will result in low capacity retention after cycling, larger polarization, a decrease in coulombic efficiency due to side reactions consuming $Li^+$. The impedance generally also increase with cycle number. [61] The reactions will mostly be seen during charging as a high degree of delithiation induce more structural changes. volume expansions and mechanical stress. [61] The phase transformations and volume expansions are however less than those seen for anodes. Total cell failure can also occur, especially if the layer CEI layer are thick and do not conduct $Li^+$. This will give a rate-determining step that limits the whole diffusion process. [62]

Not only the cathode composition but also the powder properties should be optimized in respect to electrochemical performance. The materials crystallinity, phase purity, particle morphology, grain size, surface area, and cation distribution should be carefully considered. These are directly determined by the materials synthesis method. [63, 64]

## 2.5 Synthesis routes of NMC111

NMC111 powders are traditionally synthesized by various methods, including sol-gel, hydrothermal method, and co-precipitation. Sol-gel is well-established because it produces a pure phase at high calcination temperatures. Unfortunately, high temperatures cause undesirable particle growth. Hydrothermal methods utilize sealed conditions to obtain high pressures. It maintains crystallinity and purity while using low temperatures to avoid particle growth and saving costs. [65] The co-precipitation methods are advantageous due to its uniform powders, easy-scale up and relatively low temperature conditions. [66] However, the milder temperature conditions count for a longer reaction time [65] and the reaction conditions, such as atmosphere or precursors, should be strictly controlled to produce a phase pure material. [67]

Depending on the precursors, the precipitate will form different intermediate phases. The co-precipitation using NaOH for the co-precipitation forms a $(Ni_{1/3}Mn_{1/3}Co_{1/3})(OH)_2$ (hydroxide phase) which is highly unstable due to the presence of a $Mn(OH)_2$ phase. This will easily oxidize to MnOOH and/or $MnO_2$ during the co-precipitation. This can transform into spinel phases during heat-treatment, and cause a non-stochiometry that leads to the formation of multiple other secondary phases (also referred to as impurities). The co-precipitation of hydroxide phases is often performed in the presence of $N_2$ gas to obtain inert atmospheres. This complicates the synthesis, especially in large scale productions. One way of avoiding the highly oxidizing hydroxide phase is to use carbonate precipitation $Na_2CO_3$. [68] However, few researchers have actively tested how these Mn-impurity phases eventually influence the cycling properties of the battery, and how the presence of Cl anions ($Cl^-$) will affect these oxidizing Mn phases.

### 2.5.1 Co-precipitation

Co-precipitation of hydroxide phases to make a NMC111 normally mix nitrate [69], sulphate or acetate [65] based TM precursors with ammonia hydroxide ($NH_3 \cdot H_2O$) and NaOH at a low temperature in an inert atmosphere. According to Yang and co-workers [70], $NH_3 \cdot H_2O$ act as a ligand which decreases the concentrations of free $Ni^{2+}$, $Co^{2+}$ and $Mn^{2+}$ by complexing the TMs so a homogeneous $(Ni_{1/3}Co_{1/3}Mn_{1/3})(OH)_2$ phase will participate. Li are added in a 1:1 ratio to get a $Li(Ni_{1/3}Co_{1/3}Mn_{1/3})(OH)_2$ phase. [65] The amount of ligand will influence the powder intrinsic properties. In this aspect, Hu *et. al.* [67] reported the ideal ratio of $NH_3 \cdot H_2O$ to TMs in terms of powder properties to be 2.7:1.

The TM hydroxide phases, $Ni(OH)_2$, $Co(OH)_2$ and $Mn(OH)_2$, are regarded as impurity phases. Seen from their solubility constants, these will form separately at different pH values. The pH and presence of oxidizing species (such as oxygen) should, therefore, be strictly controlled. [48, 67]

The pH, temperature, atmosphere are all reported to have a large influence on the purity of the co-precipitate. [48] Little research is however done on how different precursors influence the formation of secondary phases and intrinsic powder characteristics of active NMC111 for usage in cathodes. Some precursors, such as $CoCl_2$, is reported to accelerate the formation of Mn-based impurities. [71] It is also well known that the anions in solutions directly influence the mechanism of particle growth. [72]

As mentioned, the particle shape and size of the active powder influence the electrochemical properties practical use, so controlling the particle morphology is very important. [65] A hydrothermal step is known to enhance the powder properties of the hydroxide powder and improve battery performance. In such high pressure conditions, small agglomerated particles will grow into grains with sharp-edge morphology and more uniform distribution. [65] A way of classifying particle shape is in terms of roundness, sphericity, and angularity. This was nicely illustrated by Sims [73] in 1998 and the shapes are supplemented in the Appendix in figure A.1.

Another powder property that might influence the electrochemical properties are the single- and polycrystallinity of particles. Cho and coworkers [74] proposed that single crystal materials enhance the battery cycling performance due to higher surface areas which cause better contact with the electrolyte and shorter diffusion paths for $Li^+$. A typical ideal shape of a single-crystalline NMC111 material illustrated by Juan *et. al.* [75] is represented here in figure 2.11. The single crystals have high angularity and sphericity where each surface (or facet) corresponds to a crystal plane (104, 012 and 001). The size of each facet, and the chemical potential of Li ($\mu_{Li}$) and oxygen ($\mu_O$) influence the stability of the NMC111. The unfavored oxygen release already becomes spontaneous for delithiation above 40 % for the (012) surface. As no oxygen release occurs $<$ 60 % deltitiation at the (104) surface, one should choose a synthesis route that favor single crystals and formation of a large (104) surface. [75]

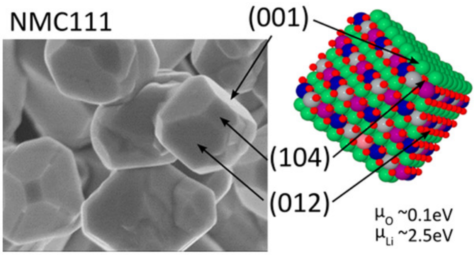

**Figure 2.11:** Particle shape of single-crystal NMC according to Juan and co-workers [75]. The $\mu_{Li}$ and ($\mu_O$) to the electrical potential of the Li and oxygen, respectively.

## 2.6 Characterization techniques

Intrinsic and extrinsic powder properties influence powders electrochemical performance. Thus, morphology, particle size, particle size distribution, and phase purity should be considered when evaluating a synthesis method for cathode materials. X-Ray Diffraction (XRD), Scanning Electron Microscopy (SEM) and nitrogen($N_2$)-pyhsisorbtion are well-known methods for these purposes. [21]

### 2.6.1 X-ray Diffraction

X-Ray diffraction (XRD) is a well-established characterization technique in the field of materials characterization to obtain information on the structure at an atomic scale of crystalline samples. In crystalline materials, the atoms, ions or molecules are arranged in a regular manner. These arrangements diffract x-rays in different manners which ultimately gives information about the materials structure ordering. [76]

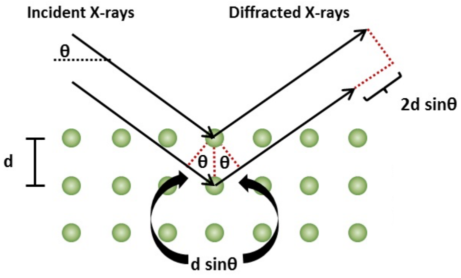

**Figure 2.12:** Schematic representation of the Bragg's equation. Illustration inspired by [77].

The principle behind XRD is shown in figure 2.12. Incident X-rays with a known wavelength ($\gamma$) hit the sample. The crystal planes diffract the beam with a specific angle ($\theta$). All diffracted X-rays will travel their own optical path length depending on the distance between lattice planes (d) and incident angle of the beam. X-rays that are scattered from the sample interfere either constructively or destructively. The angles at which constructive interference occurs are measured and described by Bragg's law in equation 2.14. This way, the Bragg equation allows determining the distance between the lattice planes of the material [78].

$$n\gamma = 2dsin\theta \tag{2.14}$$

Analysis of an XRD diffractogram may be used for [76, 77]:

- Qualitative analysis: A diffractogram is often though as the fingerprint of a sample. The diffractogram can be compared with databases and identify the crystalline material.

- Calculating the relative amounts of phases present for samples containing secondary phases or impurities.
- Detecting dimensions of unit cell lattice parameters. Smaller crystalline sizes will shift to lower $2\theta$ values.
- Determining crystallite size and strain as these usually affect the peak width.

XRD analysis is also possible to use for structural evolution *in situ* or *ex situ* at specific states during battery cycling. *In situ* battery analysis collect data during the cell cycling at the same environment that material reacts. The *ex situ* involves disassembling of the cell and extraction of the electrode for further analysis. [79]

### 2.6.2 Scanning Electron Microscopy

Scanning electron microscopy produces high resolution and high magnification images of samples by scanning the surface with a focused beam of electrons. The impact of the electrons on the sample atoms causes a variety of electron and photon emissions. The intensity of the signals contains information about topography and composition of the sample. With a lateral resolution down to 2 nm, it is often used in combination of software for evaluation of morphology and crystallite size. [80] The type of emission chosen for detection depends on the desired result. For topographical analysis mode, secondary electron emitted by atoms inelastically scattered by the electron beam is detected. The SEM sample preparation is minimal, however, non-conducting samples need a thin conducting layer of either carbon or gold. [81]

### 2.6.3 Nitrogen-physisorbtion

Nitrogen($N_2$)-physisorbtion and Brunauer, Emmett and Teller (BET) theory is commonly used to generate $N_2$-adsorption data and evaluate a specific surface area. The most common 6 step process for obtaining adsorption- and desorption isotherms in figure 2.13. [82] First, $N_2$ is pumped into a sample tube at its boiling point temperature (-196 °C) where it condenses (adsorps) on the solid with an assumption of monolayer coverage. An adsorption isotherm is obtained and used to find the volume adsorbed on the external and the accessible internal pore surfaces. From the amount of gas adsorbed and the size of gas molecules, the BET surface area is calculated. It is usually expressed in units of area per mass of sample ($m^2/g$). By including the desorbition step, an desorbtion isotherm is obtained which can be further used in calculations of pore size distribution. [83]

### 2.6.4 Electrochemical Characterization

The most common way of measuring the electrochemical performance of new material is charging and discharging of the electrode. The experiments are usually carried out with cyclic voltammetry (CV) or galvanostatic cycling. These two methods mainly obtain the same information. Galvanostatic cycling measures the practical capacity at a fixed current density (C-rate), whereas CV uses a constant potential sweep rate (V/s). A constant current allows more time for the electrochemical processes to react to completion whereas CV

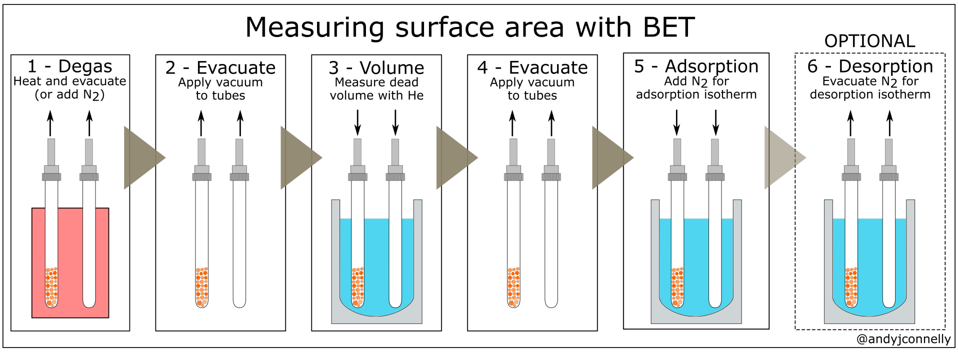

**Figure 2.13:** The 5 step process of $N_2$-pysisorbtion used to obtain an adsorption- and desorbtion isotherm. Figure obtained from [82]

force the change of potential regardless of the state of charge of the electrode. The kinetic limitation may thereby restrict some of the capacity from being accessed. [79]

To avoid overcharging, the charge and discharge cycles are terminated when it reaches a particular potential. An overcharge will continue the (dis)charge after all active material has been utilized. At this point, other components will start breaking down to provide electrons and reduce cycle capability. [79]

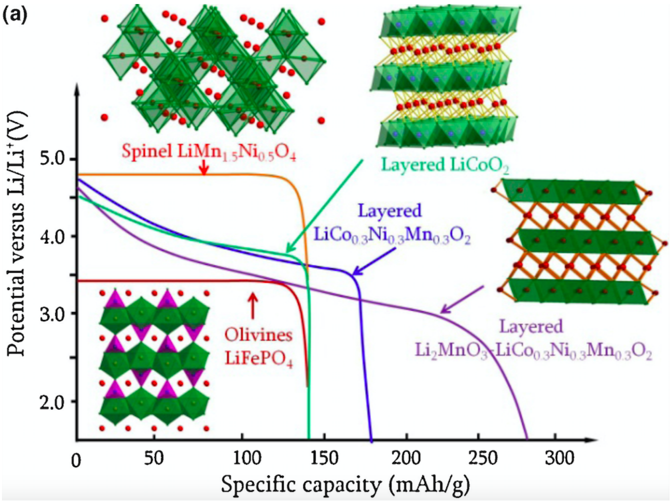

**Figure 2.14:** The discharge profiles and crystal structures of most common materials. Capacity (mAh/g) is plotted against potential vs $Li^+/Li$ (V). [22]

Galvanostatic profiles are usually presented in potential plots called the charge-discharge profile. Here, the specific capacity is plotted against the potential (vs $Li/Li^+$). [79] The crystal structures of material causes distinct plateaus that be used as a tool to characterize the cathodes (de)intercalation mechanisms and structure changes during cycling. The typical discharge profiles of four different cathode materials are presented in figure 2.14. [22] Another way of presenting galvanostatic cycling data is through a differential capacity (dQ/dV) plot. Here, the inverse of the derivative of the potential times the specific capacity curve is plotted against the potential. The plateaus in charge-discharge profiles are now seen as peaks. Each peak corresponds to an active redox couple, and these are shown in figure 2.15 for Li-rich NMC. Small variations for each cycle account for reversible reactions whereas the area under peaks are the capacity of that particular process. This way, such plots provide information about the interplay between anionic/cationic redox couples governing the kinetics and thermodynamics of the cathode. [79, 84] The figure 2.15 also shows the anionic redox reactions ($O^{2-}$). However, cationic reactions are without hysteresis kinetically faster than sluggish anions. Anionic redox increases the capacity but will cause a hysteresis, poor kinetics, and voltage fade. [84]

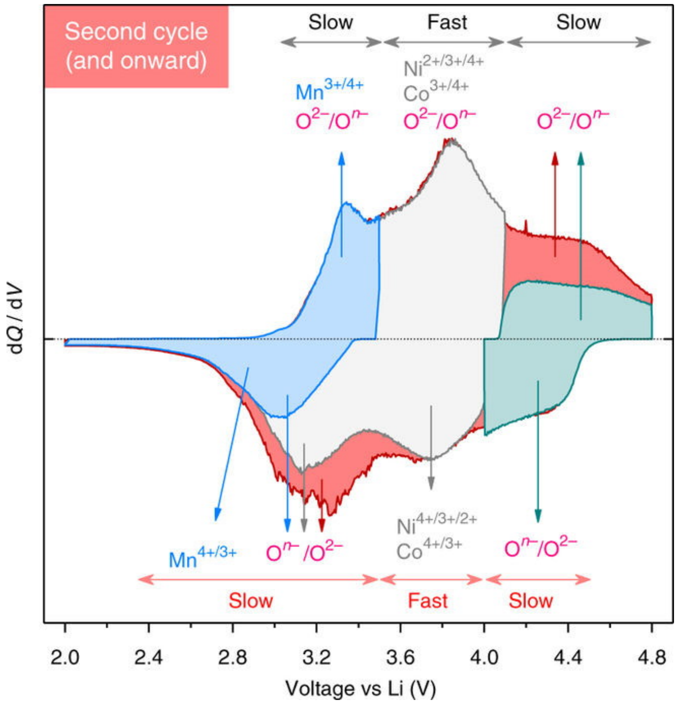

**Figure 2.15:** The dQdV-plot for a typical Li-rich NMC111. The electrochemical kinetics (based on impedance measurements) and peaks corresponding to the anionic and cationic redox reactions. Small capacity is contributed from $Mn^{3+/4+}$ at low potentials with a peak at 3.2 V (blue). Further charging to 4.1 V will give a peak at 3.8 from cationic oxidation (gray). For higher potentials up to 4.8 V (red and green), the main contribution to capacity will be from anionic reactions. Upon discharge at high potentials (4.8 V), the charge compensation is split in two. This is causing hysteresis. The data is based on work from Assat and co-workers [84].

### 2.6.5 Electrochamical impedance spectroscopy

The battery state and behavior are characterized by the interplay of a large number of physical processes, occurring on very different time scales, from microseconds to years [85]. These processes are measured by imposing an alternating signal (current or potential) with a certain amplitude in a frequency range from kilohertz (kHz) to millihertz (mHz). The impedance spectrum is then plotted in a typical Nyquist plot shown in figure 2.16a. Three main processes are clearly distinguished. From low to high frequencies, these are the Warburg impedance representing mass transport ($Z_w$), charge transfer in the electrochemical double layer ($R_{ct}$ and $C_d$) and ohmic resistance from the bulk electrolyte ($R_e$). An equivalent circuit depending on the system complexity is used to interpret the Nyquist plot. Each component in the circuit represents a particular process contributing to the cells overall voltage drop. The Randall circuit is shown in figure 2.16b is the simplest representation of a battery. [86]

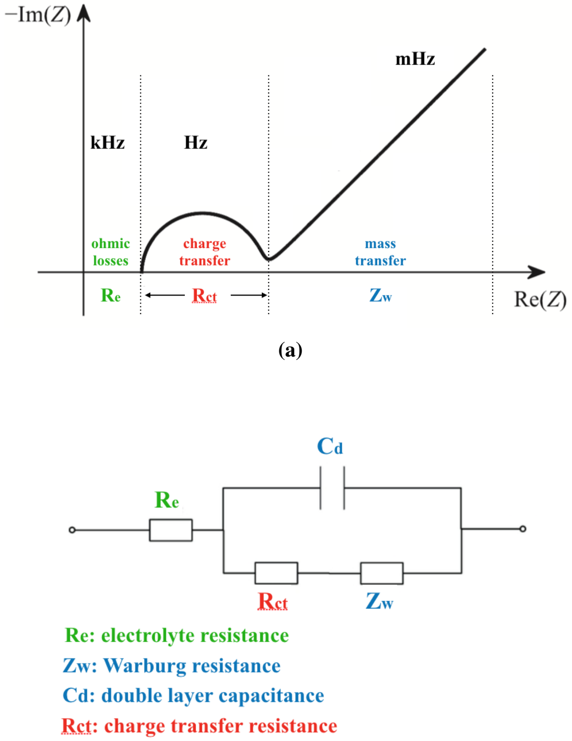

(a)

(b)

**Figure 2.16:** Typical a) Nyquist impedance spectrum in a frequency range from millihertz to kilohertz, revealing different electrochemical processes, and b) the corresponding Randall equivalent circuit. Diffusion prosesses dominat at low frequensies. Charge transfer processes are revealed at high frequencies. The figures are adopted from [86].

# Chapter 3

# Experimental

The following section gives a detailed description of the experimental work. It is divided into four main parts: The powder synthesis, cathode material preparation, cell assembly, and characterization methods. The powder synthesis is the only part where parameters were varied between the samples.

First, the purity and linear formula of all chemicals used during powder synthesis, cathode preparation, and cathode assembling are presented in table 3.1.

## 3.1 Powder Synthesis

The powder synthesis is divided into two sections depending on atmosphere conditions during the co-precipitation reaction. An overview of the synthesis conditions and the respective sample names is presented in figure 3.1 and main variables are summed up below.

1. Synthesis in air
    - Pressure condition during Li-reaction
    - The order of Li-addition
    - Length of heat-treatment
2. Co-precipitation synthesis in $N_2$ (inert) atmosphere

For clarity, the purity and CAS number of all solutions are presented in table 3.1. The powder synthesis' was performed using the two different combinations of TM solutions (_Cl and _Aq) showed in table 3.2. This was done to observe the effect of Cl-containing precursors. For samples named _Aq, the precursors were dissolved in distilled water. These samples were also referred to as the aqueous(Aq)-based TM solutions. Here, the $Ni(NO_3)_2$, $Mn(NO_3)_2$ and Co acetate tetrahydrate (Co-Ac) solutions were dissolved in distilled water with concentrations of approximately 3.7 mol/L, 2.9 mol/L, and 3.7 mol/L, respectively. The Co-Ac solution was then standardized by thermogravimetry (as described below) to find the exact amount of cations in the solutions and ensure correct stoichiometry. Samples

**Table 3.1:** List of names and linear formula of chemicals used, CAS number[87], producer and purity.

| **Chemical** | **Linear formula** | **CAS number** | **Producer** | **Purity [%]** |
|---|---|---|---|---|
| Lithium hydroxide monohydrate | $LiOH \cdot H_2O$ | 1310-66-3 | Sigma-Aldrich | $\geq 98.0$ |
| Lithium nitrate | $LiNO_3$ | 7790-69-4 | Sigma-Aldrich | 99.995 |
| Nickel(II) nitrate hexahydrate | $Ni(NO_3)_2 \cdot 6H_2O$ | 13478-00-7 | Sigma-Aldrich | $\geq 98.5$ |
| Nickel(II) chloride | $NiCl_2$ | 7718-54-9 | Glencore Nikkelverk | $\geq 99.99$ |
| Cobalt(II) chloride | $CoCl_2$ | 7646-79-9 | Glencore Nikkelverk | $\geq 99.99$ |
| Cobalt(II) acetate tetrahydrate | $(CH_3COO)_2Co \cdot 4H_2O$ | 6147-53-1 | Sigma-Aldrich | $\geq 98.0$ |
| Manganese nitrate tetrahydrate | $Mn(NO_3)_2 \cdot 4H_2O$ | 20694-39-7 | Sigma-Aldrich | $\geq 97.0$ |
| 25 % Ammonium hydroxide | $NH_4OH$ | 1336-21-6 | Sigma-Aldrich | $\geq 99.99$ |
| Ethanol | $C_2H_6O$ | 64-17-5 | VWR Chemicals | $\geq 96$ |
| Carbon black | C | 1333-86-4 | Solvey | |
| 1-Ethyl-2-pyrrolidone (NEP) | $C_6H_{11}NO$ | 2687-91-4 | Sigma-Aldrich | $\geq 99$ |
| Poly-1,1-difluoroethene (PVDF) | $(CH_2CF_2)_n$ | 24937-79-9 | Imerys | |
| Lithium hexafluorophosphate in ethylene-/dimethyl carbonate | $LiPF_6$ (1M) in EC/DMC (1:1) | 21324-40-3 | Sigma-Aldrich | $\geq 99.99$ |
| Lithium foil | Li | 7439-93-2 | Alfa Aesar | 99.9 |
| Aluminum foil | Al | 7429-90-5 | Alfa Aesar | 99.45 |

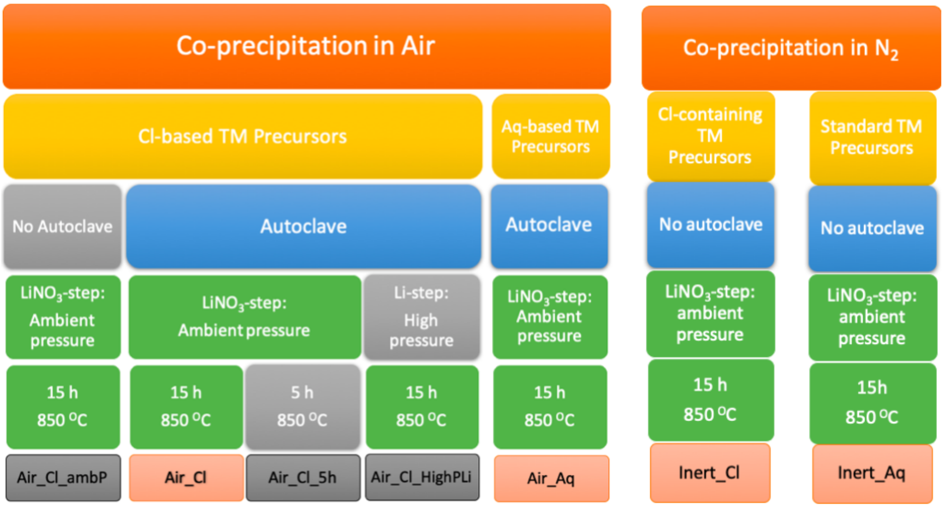

**Figure 3.1:** A flow chart representing the synthesis conditions of all seven samples. They are divided into two categories depending on the synthesis atmosphere during the precipitation, being either inert or air (red). These are divided into subcategories dependent on the TM precursors (yellow). These are either chloride (Cl) based or purely aqueous (Aq) based. Green box describes the main synthesis conditions and sample names. The samples are named Air_Cl, Air_Cl_HighPLi, Air_Cl_5h, Air_Cl_AmbP, Air_Aq, Inert_Cl, and Inert_Aq. The additional (_HighPLi, _5h and _AmbP) refers to the changed Li addition, heat-treatment and pressure condition, respectively.

named _Cl used $NiCl_2$(178 g/L) and $CoCl_2$ (199 g/L) solutions from Glencore Nikkelverk instead of the abovementioned Ni and Co precursors.

**Table 3.2:** The Ni, Mn and Co precursors used as the TM precursor solutions for powder synthesis. For _Aq, the chemicals are mixed in distilled water. Cl refers to the TM precursors mixed dissolved in HCl.

| Precursor name | Ni | Co | Mn |
|---|---|---|---|
| _Aq | $Ni(NO_3)_2$ | Co acetate tetrahydrate | $Mn(NO_3)_2$ |
| _Cl | $NiCl_2$ | $CoCl_2$ | $Mn(NO_3)_2$ |

## 3.1.1 Thermogravimetry

The Co-Ac tetrahydrate solution was standardized using a thermogravimetric method. The following procedure was performed on four parallels. Four porcelain crucibles with Kao wool were heat treated previously using the heat treatment program in figure 3.2 to ensure removal of organic material and water. The Co-Ac tetrahydrate solution (20 mL) was added to each crucible. These crucibles were weighed again, and heat treated again with the same program. At the end of the program, the crucibles were immediately moved from the furnace into a desiccator. After being cooled down to room temperature, the four crucibles were weighed again.

Cobalt tetraoxide ($Co_3O_4$) was assumed to be thermodynamically favored at the chosen standardization temperature (800 °C) and was used to calculate the weight of cation per gram solution. The concentration of the metal cation in solution (mol cation/gram solution) was determined by the mass of the initial solution and the mass of the formed $Co_3O_4$.

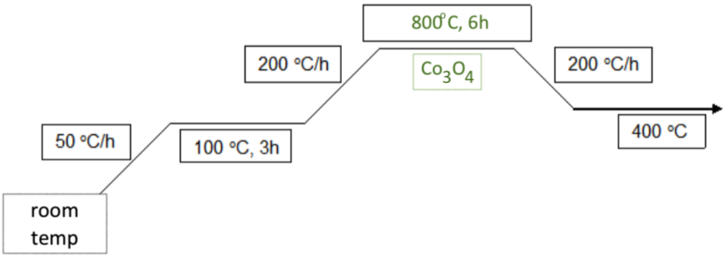

**Figure 3.2:** Heat treatment program used for the termogravimetric standardization of the Co-Ac tetrahydrate solution.

## 3.1.2 Powder synthesis in air

The five synthesis methods tested in air was named Air_Cl, Air_Aq, Air_Cl_5, Air_Cl_HighPLi and Air_Cl_ambP. The synthesis of Air_Cl will be used as a reference for explaining the other synthesis routes.

### Synthesis of Air_Cl powder

The horizontal arrows (including the green arrow named Air_Cl) in figure 3.3 illustrates the synthesis steps of Air_Cl:

1. Samples named _Cl used the solutions from Glencore Nikkelverk ($NiCl_2$ and $CoCl_2$ as Ni and Co precursors, respectively). These were mixed with a standardized $Mn(NO_3)_2$ solution in a molar ratio of 1:1:1 and stirred for a few minutes. A 25 % ammonia hydroxide ($NH_4OH$) solution was slowly added so pH reached $> 11$ while stirring for 3 h at 50 °C. The solution was kept stable at these conditions and stirred for 20 h. A brown precipitate and dark purple solution were obtained.
2. This precipitate was washed heavily with distilled water filtration (6 times) and centrifuging (10 times).
3. Further, the precipitate was transferred to a Teflon liner (120 mL), which was filled up with $NH_4OH$ to 67 % of its volume capacity. This was placed in a 120 mL stainless steel autoclave (Parr), sealed and heated to 120 °C. The powder was under

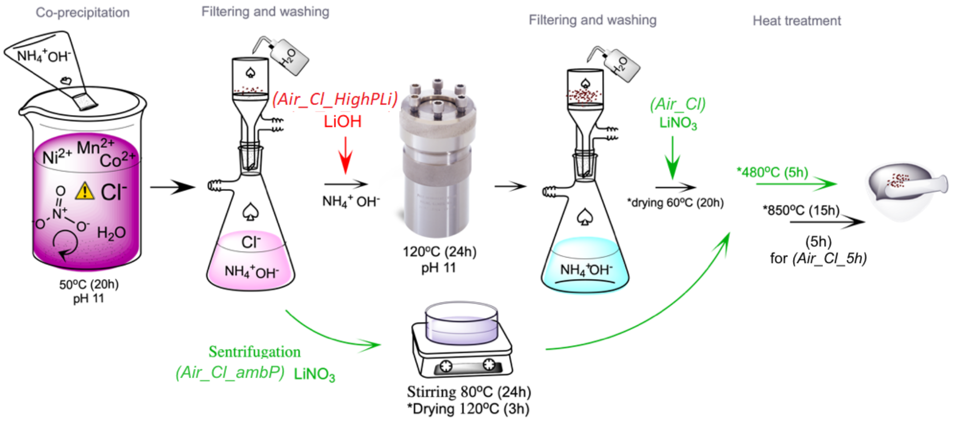

**Figure 3.3:** An illustration of the synthesis route for Air_Cl; this synthesis follows the horizontal arrows including the green $LiNO_3$ vertical arrow named Air_Cl). The Air_Cl_HighPLi follows the same route, except the green vertical arrow, was replaced with an early LiOH addition (in red named Air_Cl_HighPLi). The synthesis of Air_Cl_5h follows the same route as Air_Cl, except it had a shorter heat-treatment of 5 h (italic black). In the synthesis route of Air_Cl_AmbP, the autoclave and second filtering step were excluded; the deviating part of this synthesis is described by the bent arrows colored green. Air_Aq is not shown as it would only differ from the Air_Cl route is that Cl is not present in the solution.

this auto-generated pressure for 24 h, then cooled to room temperature naturally. A brown precipitate and clear colorless solution were obtained.

4. The precipitate was washed by filtration with distilled water.

5. The washed powder was then dried at 60 °C in vacuum overnight and weighted. A solid $LiNO_3$ precursor was added to the hydroxide precipitate ($(Ni_{1/3}Co_{1/3}Mn_{1/3})(OH)_2$) in a ratio of 1:1 relative to the TM ions. These powders were thoroughly mixed with mortar & pestle (M&P) to form the precipitate ($Li(Ni_{1/3}Co_{1/3}Mn_{1/3})(OH)_2$)

6. The mixed powder was then calcined at 480 °C for 5 h to remove impurities.

7. Further, it was heat-treated at 850 °C for 15 h (5 hours for Al_Cl_5h) to transform into the NMC111 oxide. All heat-treatments used a heating and cooling rate of 200 °C/h.

8. The powder was then crushed using M&P, analyzed with XRD, and used as active cathode material in a LIB half-cell.

### Change of precursor (Air_Aq)

For the synthesis of Air_Aq, $Ni(NO_3)_2$ and Co acetate precursors were used instead of $CoCl_2$ and $NiCl_2$. The first filtration and washing step were reduced (from 5 times to 1 time) and the centrifuge step was skipped. The Air_Aq is not shown in the figure 3.3 since the synthesis route would look identical to the route for Air_Cl; except the Cl would not be present.

**Change of Li-addition step (Air_Cl_HighPLi)**

For Air_Cl_HighPLi, the Li precursor is changed from $LiNO_3$ to LiOH. Also, Li was added after the first washing in (red, described in step 2) instead of after the second washing (green, described in step 5) in figure 3.3. This way, the Li reaction occurred in high-pressure conditions at 120 °C. Two parallels where higher temperatures (160 °C and 175 °C) were tested and are added in Appendix B.

**Change in pressure conditions (Air_Cl_ambP)**

The green in figure 3.3 represent Air_Cl_ambP. Here, step 3 and 4 described above was skipped. Instead of using the autoclave the precipitate was mixed with the $NH_4OH$ and stirred at 80 °C for 24 h. Then, it was dried at 120 °C for 3 h. From the addition of $LiNO_3$ in step 5, it followed the same procedure as Air_Cl.

**Heat-treatment (Air_Cl_5h)**

The Air_Cl_5h had a 5 h heat-treatment at 850 °C in synthetic air. This is shown in black in figure 3.3.

### 3.1.3 Co-precipitation in inert atmosphere

The second category of powder synthesis represent the two samples Inert_Cl and Inert_Aq. Both syntheses were performed two times to ensure reproducible results (Inert_Cl_2 and Inert_Aq_2). The inert atmosphere was obtained by pumping $N_2$ gas into a 25 % $NH_4OH$ solution (200 mL) inside a three-neck distillation flask. The flask was placed in a water bath at 50 °C. A pH meter and thermometer was placed in the third neck of the flask. These two neck holes were sealed and the system was left for 1 h to ensure an inert $N_2$ atmosphere. The third neck was used for the addition of the TM solution and NaOH. The synthesis route and parameters are illustrated in figure 3.4. The differences between the two samples were the precursor solutions for Ni and Co shown in table 3.2, and extra filtering and sieving step for the synthesis using a TM solution containing Cl.

The precursors described in table 3.2 was mixed in a ratio of 1:1:1 into two different TM solutions. The TM solution was dripped slowly (rate?) into the distillation flask during heavy stirring (750 rpm). A NaOH (4 M) solution was added simultaneously to keep pH 11.

Inert_Cl and Inert_Aq was filtered 10 times and 1 time, respectively. During the washing process of Inert_Cl, the filtered water was tested with $Ag(NO_3)$ to detect any Cl. The precipitate was dried at 60 °C overnight and crushed with M&P. An extra sieving step was added for Inert_Cl to remove contamination from the filtration paper from the extra washing steps. The obtained precipitate was weighted. $LiNO_3$ was blended into the precipitate with M&P. Then, it was first calcined at 480 °C (5 h), blended in M&P, and heat-treated at 850 °C (5 h) in synthetic air. The rate of temperature change was set to 200 °C/h.

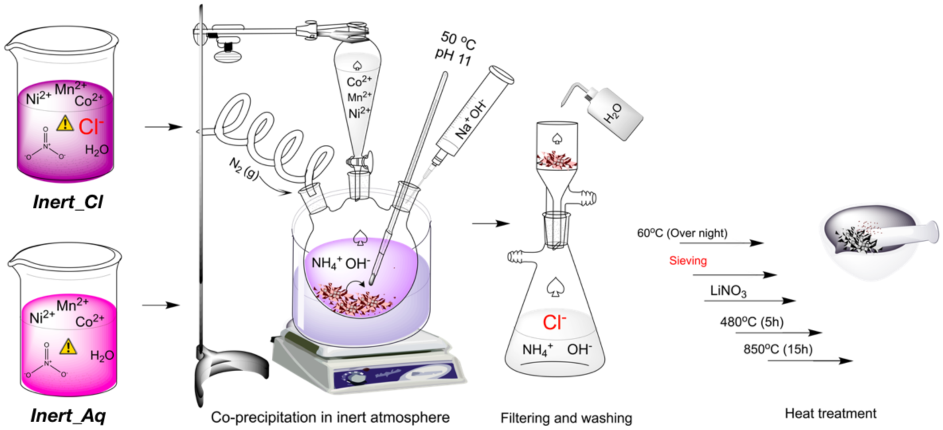

**Figure 3.4:** The experimental setup of the Inert_Aq and Inert_Cl powder synthesis in an inert atmosphere. In the Inert_Cl synthesis, the presence of $Cl^-$ accounted for multiple filtration steps, followed by an extra sieving step (shown in red).

## 3.2 Cathode Preparation

The seven powders described above were treated in the same way after synthesis and all are referred to as the active powder in this section. The active powder was made into a slurry with a 1:20 wt % solution of polyvinylidene difluoride (PVDF Keynar, reagent grade) binder in N-ethylpyrrolidone (NEP) and vacuum dried Super-P carbon black (60 °C overnight) as conductive additive. The active powder, carbon black and binder were mixed with a weight ratio of 85:10:5, respectively. The slurry was transferred to a metal jar containing a metal ball. This was shaken using a Retsch MM400 shaker mill for 30 minutes at a frequency of 25 $s^{-1}$. Aluminum foil (0.025 mm thickness) was cleaned with ethanol and used as a current collector. The slurry was tape-casted onto the metal foil with a metal-bar giving a 100 $\mu$m wet film thickness. The cast was dried overnight (60 °C) then in vacuum (120 °C for 5 hours). The cathodes were cut out in circles with a diameter of 16 mm and weighted. The weight of the Al foil (13.906 mg) was subtracted to calculate the amount of active cathode material (85 % of the cathode material mass). From all seven casts, three parallel electrodes was used to make three coin-cells.

## 3.3 Cell Assembly

The coin cells were assembled in a Glovebox (MBRAUN UNIlab) with Ar atmosphere and $H_2O$ and $O_2$ levels $\geq 0.1$ ppm. The case, spacer and cap were made of stainless steel (SUS216L alloy). The cells used (CR2016 Hohsen Coin Cell) were 1.6 mm thick with a diameter of 20 mm. The battery components and order of assembly are presented in figure 3.5. First, a plastic gasket was placed inside the lid to ensure hermetic sealing of the cell. The cathode was then placed with active material facing upwards. Thereafter, a microporous separator (Celgard 2320) with 20 µm thickness was cut out in a 17 mm diameter circle and placed between the cathode and Li metal anode. The electrolyte (1 M $LiPF_6$ in EC/DEC) was applied with a pipette before (20 µL) and after (20 µL) placing the separator to ensure complete soaking. The Li metal anode was cut out with a diameter of 14.0 mm from a 0.75 mm thick Li foil (99.9 %, Alfa Aesar). It was brushed to remove surface oxide layers. The Li metal was then pressed onto a stainless steel space filler (SUS316L alloy) with a diameter and thickness of 16 mm and 0.3 mm, respectively. This was placed over the separator with the Li metal facing down. The lid was pressed on top with a crimping machine. The coin cells rested for at least 12 hours before electrochemical cycling. [65]

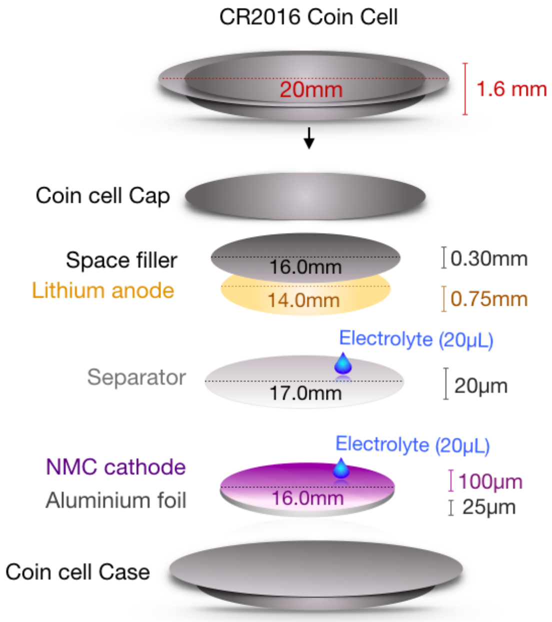

**Figure 3.5:** All the components used for cell assembly of the CR2016 coin cell are shown in the correct order. These components are the coin cell cap, space filler, anode, separator, electrolyte, cathode, current collector and coin cell case. The known diameter and height, or amount of each component are included.

## 3.4 Characterization Methods

### 3.4.1 XRD

The XRD measurements were performed on a Bruker D8 DaVinchi Diffractometer using a Cu K$\alpha$ radiation source, and a fixed slit size of 0.2. The XRD scan program used was done from a $2\theta$ value of 10° to 75°. The powder samples were prepared by mixing in ethanol (96 %) and dripping on to a flat silicon (Si) crystal sample holder. Analysis of the obtained XRD plots was performed using DIFFRAC.EVA software from Bruker. The Rietveld analysis was performed on DIFFRAC.TOPAS version 5.0 from Bruker. The reference scans used for matching were found in PDF 2019+ database, and are found in Appendix table A.1.

### 3.4.2 SEM

The SEM imaging was performed after powder synthesis using a Zeiss Supra 55VP apparatus with a working distance (WD) of ~ 8-10 mm and a Everheart-Thornley Secondary Electron Detector. The accelerating voltage was 3 kV for the Air_Cl, Air_Aq Air_Cl_HighPLi and Air_Cl_5h powders, and 10 kV for Air_Cl_ambP, Inert_Cl, and Inert_Aq powders. The scan time was 20.2 s per image. Powders were scanned at high and low magnifications (500, 1K, 10K, and 20, 40K or 50K). The software (ImageJ version 1.52a) was used to indicate variations in particle size (VPS) and the average particle size (APS). Four scales were done on a minimum of randomly selected 50 particles. These were used as an indication of relative average particle sizes (APS) and particle size distribution (PSD) obtained by the synthesis methods.

### 3.4.3 BET

The surface area of sample Air_Cl, Inert_Cl, Air_Cl_5h, Air_Aq and Air_Aq (480 °C) (before 15 h 850 °C heat-treatment) was calculated by using the nitrogen($N_2$)-physisorbtion and the BET theory model. The analysis was done as shown in figure 2.13 excluding the desorbtion step. First, the samples were degassed to remove adsorbed water overnight at 250 °C in vacuum. The tubes were filled with $N_2$ to reduce the amount of humidity affecting the sample after drying and weighted. The apparatus used for $N_2$-physisorbtion was Micromeritics TriStar 3000. The adsorbtion isotherms were detected by adsorbing $N_2$ to the known sample mass, at liquid nitrogen temperatures (-196 °C). The adsorbed $N_2$ per sample mass was plotted against the relative pressure of the gas. BET theory modeled the adsorbed species as multiple layers and the total surface area was calculated assuming a monolayer coverage. [83] A filling rod was applied for the analysis of Air_Aq (480 °C) due to a low sample mass (0.0119 g).

### 3.4.4 Galvanostatic Cycling

All cells were tested electrochemically through galvanostatic charge/discharge cycling. Li metal was used as a counter electrode, so the potentials measured were relative to Li/Li$^+$. All electrochemical tests were done at a computer-controlled Lanhe CT2001A potentiostat in room temperature. The principle of these tests was to send a controlled current through the coin cells while measuring the voltage response. A cutoff voltage lower than the normal (3.0 - 4.3 V) was chosen to detect the presence or absence of spinel phase transformations. A long-term performance testing was done on all cells to investigate capacity stability. The long-term cycling performance program was as follows:

- During cycling of the coin cells, the charge/discharge rates (C-rates) varied. 1C was defined as the current density needed to completely charge/discharge a cell with a theoretical capacity of 160 mAh/g in 1 hour.
- The cells were cycled between 2.5 V (discharged state) and 4.3 V (charged state).
- A relative low current density of 0.1C (16 mAh/g) was chosen for the first Li$^+$ intercalation cycle to ensure an effective SEI formation. Thereafter, the current rate was fixed at 0.2C (32 mAh/g) for 200 cycles.
- The active mass of each cathode was added so its specific capacity was calculated continuously during testing.
- The coin cells are initially in their discharged states, as the cathode is the source of Li$^+$. Hence, all programs started with an initial charge cycle to extract all Li from the cathode structure.

### 3.4.5 EIS

Electrochemical impedance measurements (EIS) were tested on charged half-cells using Biologic VMP3 instrument with the EC-lab V10.40. The cells were first charged potentiostatically by applying 3.5 V until no current was flowing and an equilibrium state was reached. The frequency range was from 500 kHz to 0.01 Hz with a sinus amplitude of 10 mV.

# Chapter 4

# Results

The sequence of results will be in the following format; phase characterization of active powders, powder morphology and particle characteristics and electrochemical performance of the resulting cathode.

## 4.1 Phase characterization of active powder

The first two subsections are divided dependent on the atmosphere during the co-precipitation of the active powder. Starting with air-synthesized powders, different synthesis routes and parameters are tested due to difficulties in obtaining phase pure NMC111. These impure powders will be referred to as NMC, whilst pure phased materials will be referred to as NMC111. For the inert synthesis, a pure NMC111 phase is obtained, so the focus will be on the effect of Cl. Lastly, a third subsection will sum up the quantitative results obtained from the Rietveld analysis'.

### 4.1.1 Synthesis in air atmosphere

The Rietveld analysis of Air_Cl_HighPLi shown in figure 4.1 estimates it to contain a 58.8 % spinel phase. The formation of the spinel phase indicates stochiometric errors, and that the Li-reaction is incomplete in high pressure conditions at 120 °C. The two other temperatures tested (160 °C and 175 °C) also obtained a spinel phase. Their XRD patterns (before and after the heat treatment at 850) are seen in figure B.1 in the Appendix B. The Li that did not react is therefore likely to have been washed out after the hydrothermal step. Thus, the addition of Li must occur before the filtration step to obtain NMC111.

Since the Li does not react in high pressure conditions, synthesis excluding the hydrothermal step (Air_Cl_ambP) is tested. Interestingly, this results in high amounts of unwanted secondary phases shown in the XRD spectra in figure 4.2. Most secondary phases are observed prior to heat-treatment, but disappear during the 15 h heat-treatment.

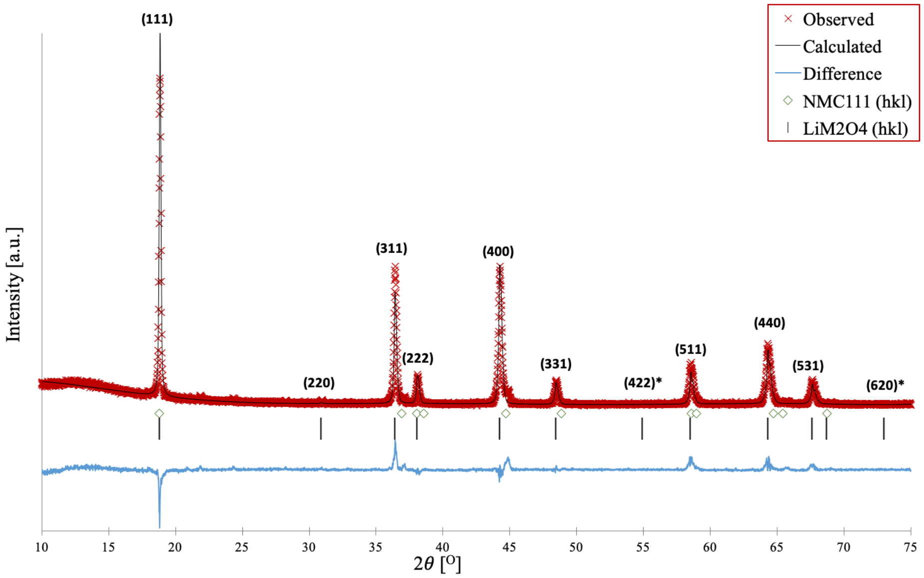

**Figure 4.1:** Rietveld refined XRD pattern for synthesis having a high pressure Li-reaction (Air_Cl_HighPLi).

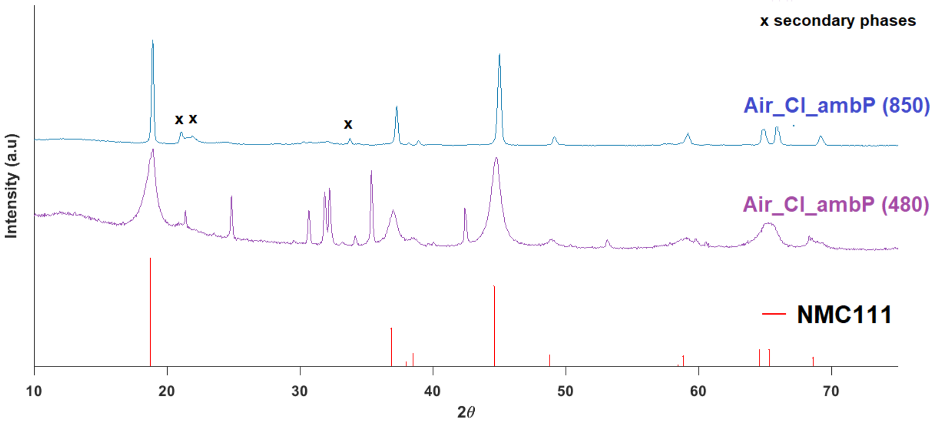

**Figure 4.2:** The XRD diffractograms of synthesized samples without a hydrothermal step before (Air_Cl_ambP (480)) and after (Air_Cl_ambP (850)) the 15 h heat-treatment at 850 °C. The peaks that neither match with the index or are marked with a cross (x) are referred to as impurity phases.

The secondary phases are mainly between 10-30 $2\theta$, zoomed in figure 4.3. These match indexes of multiple Mn-oxidation states including $Mn_3O_4$, $MnO_2$ and $Li_2MnO_3$. Here on, these will be referred to as secondary phases or impurities. The formation of these phases indicates that Mn oxidizes not only during the co-precipitation but also after. It is now assumed that hydrothermal conditions prevent further oxidation of Mn after the co-precipitation, and should therefore be included in all further synthesis performed in air.

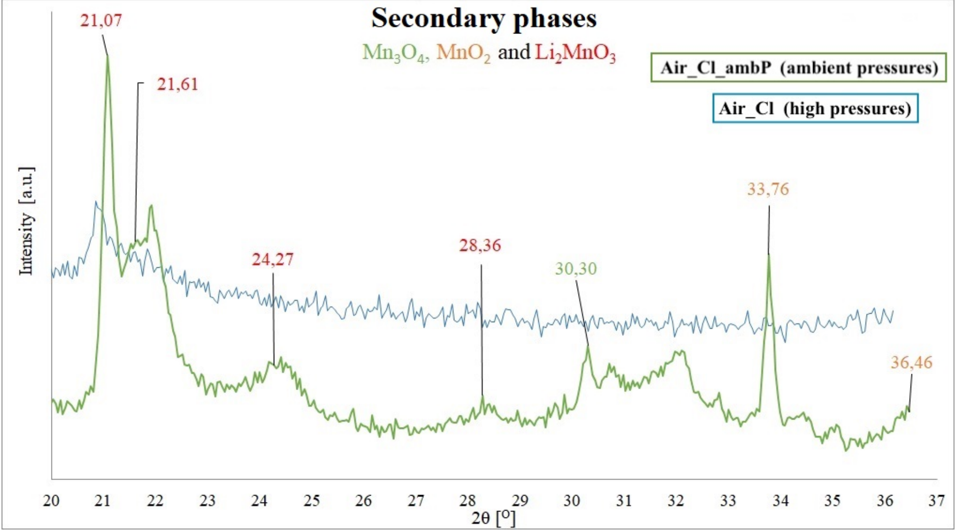

**Figure 4.3:** The XRD diffractograms of the secondary phases found at $2\theta$ values between 20-30 for Air_Cl_ambP (green) and Air_Cl (blue). Secondary phases are $Mn_3O_4$ (green), $MnO_2$ (yellow) and $Li_2MnO_3$ (red). The peaks that are not identified are referred to as impurity phases or secondary phases. The index references are found in Appendix A table A.1

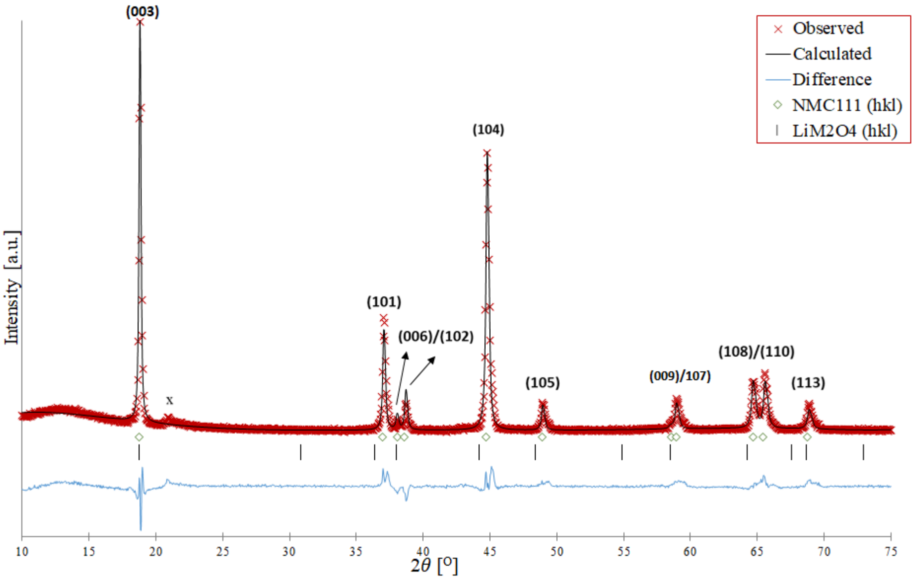

**Figure 4.4:** The Rietveld refinement of the XRD pattern for the purest NMC phase obtained in air (Air_Cl).

As seen for the powder (Air_Cl_HighPLi) above, the Li does not fully react during the hydrothermal step. However, the synthesis of Air_Cl_ambP shows that this step is necessary as it reduces the development of unwanted secondary Mn phases (figure 4.3). To support this theory, a third route (Air_Cl) investigates the combination of a hydrothermal step to eliminate the unwanted phases, with the ideal Li reaction in ambient pressures. Consequently, Air_Cl obtains the NMC111 phase with the highest purity synthesized in air. Rietveld analysis of the XRD pattern shown in figure 4.4 estimates a cation mixing of 8.7 %. One impurity is detected at 21-22 $2\theta$ and does not fit in the refinement. This peak matches that expected from a $Li_2MnO_3$ phase. [88]

The same synthesis as for Air_Cl is performed using Aq-based TM precursors (Air_Aq). These two have similar impurities shown in 4.5. Thus, the Cl-precursors are not a source of impurities. After thorough investigation of the spectra's (003)/(104) peaks and $2\theta$ values, Air_Aq and Air_Cl are estimated to have the approximate same values of cation mixing.

Figure 4.5 also present Air_Cl (480°C) and Air_Aq (480°C) before the 15 h heat-treatment at 850 °C. The layered NMC111 phase is not obtained until after this complete heat-treatment. Within the squares are areas that strongly deviate from the layered NMC111 phase. A dominant spinel phase is seen at 480 °C, and undergoes a phase transformation into a layered material at 850 °C. [89] The extreme impurities formed in the powder synthesized at ambient pressures before the heat-treatment (Air_Cl_ambP (480°C)) no longer eventuate. Only a small peak is detected around 21 $2\theta$. This supports the previous theory; the formation of Mn secondary phases occur both during and after the co-precipitation at

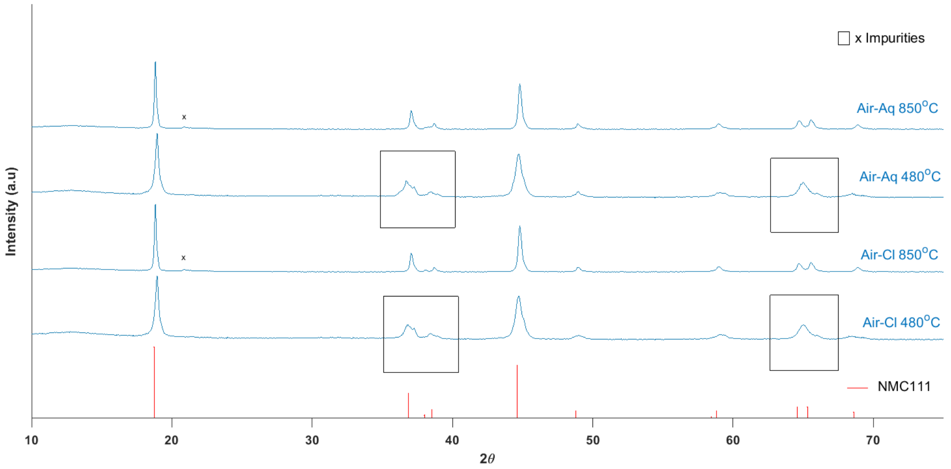

**Figure 4.5:** The normalized XRD patterns for powders made in an air synthesis with Cl (Air_Cl) and without Cl (Air_Aq) before (480°C) and after (850 °C) the 15 h heat-treatment.

ambient pressures. In addition, phases are generated independently of precursors.

A 15 h heat treatment is also needed for obtaining a phase pure NMC111 (Air_Cl). The powder made with a shorter heat-treatment of 5 h (Air_Cl_5h) shows more impurities. Referring to figure 4.6, both the 15 h and 5 h heat treatments transform the spinel phased powder (Air_Cl 480°C) into a layered NMC. However, the impurity phases found in the 5h heat-treated sample are more dominant. Most are observed at approximately 20-30 $2\theta$ and recognized as the $Li_2MnO_3$ phase. This phase is also found in the Air_Cl_ambP in figure 4.3.

### 4.1.2 Synthesis in inert atmosphere

The Rietveld refinements of the XRD diffractograms obtained from the inert synthesized active powders (Inert_Cl and Inert_Aq) are shown in figure 4.7. Both powders match the indexes for a preferred layered NMC111 phase. The purity of the favorable NMC111 structure is reflected in the (006)/(102) and the (108)/(110) reflection pairs. A clear splitting of these peaks appear from the oxygen sub-lattice, which has a distortion in the c-direction. [90] The two inert-synthesized powders display a clear splitting as seen in figure 2.7. This means that an ideal $\alpha$-$NaFeO_2$ structure with a space group of $R\bar{3}m$ has been produced. [22]

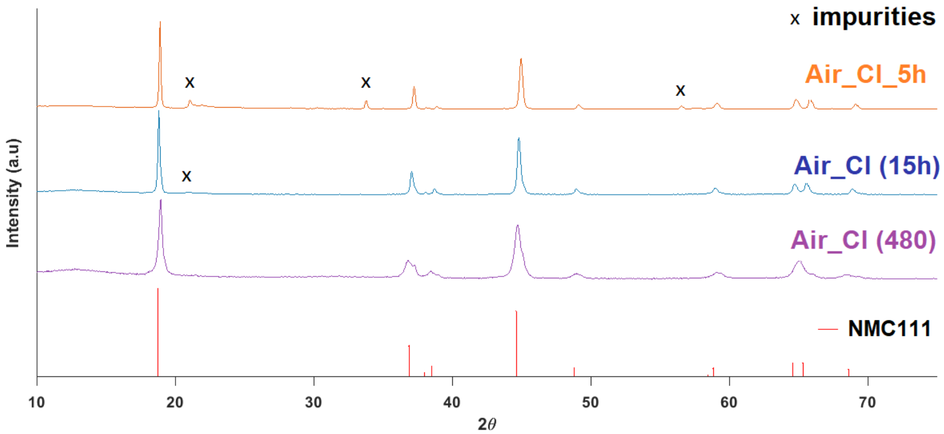

**Figure 4.6:** The normalized XRD patterns for powders synthesized in air using Cl precursors. The purple pattern (Air_Cl 480) shows the powder after the heat treatment at 480 °C. The blue (Air_Cl 15 h) and yellow (Air_Cl 5 h) represents the powders after 15 h and 5 h heat-treatmentt at 850°C, respectively. The impurity peak (x) at 21 2$\theta$ matches an index expected for a $Li_2MnO_3$ phase. [88]

### 4.1.3 Quantitative phase characteristics

The Rietveld analysis' are performed on the powders with the least amount of secondary phases. All of the Rietveld refinements show a good agreement between the observed and calculated XRD patterns. The four Rieveld refinements from above are used to calculate information in table 4.1. The amount of $Ni^{2+}$ in the $Li^{+}$-layers are found to be 2.4 % and 7.8 % for Inert_Cl and Inert_Aq, respectively. The quantitative data in table 4.1 also shows that these inert synthesized powders have a lower cation mixing relative to the Air_Cl made in air (8.7 %). This is due to the secondary phases that form when Mn oxidizes in air. Also, from table 4.1, Inert_Cl has smaller lattice parameters (a and c) in the unit cell, but has a four times larger crystal size relative to that using Aq-based precursors (Inert_Aq).

The unit cell volume for a typical NMC111 crystal is 100.6 Å$^3$, thus the Inert_Aq has the cell volume closest to the desired value (100.87 Å$^3$). The Air_Cl_HighPLi has a larger unit cell volume (103.1 Å$^3$) and is closer to the value expected of a $LiNiO_2$ material (102.3 Å$^3$). The high cell volumes seen in the spinel phased Air_Cl_HighPLi are in accordance with the $LiMn_2O_4$ structures, as these typically have a larger unit cell volume. [45, 91] The Air_Cl (99.98 Å$^3$) and Inert_Cl (99.76 Å$^3$) has unit cells smaller than that of a NMC111 phased structure and is more similar to that expected of a $LiCoO_2$ structure. [45]

## 4.2 Powder morphology and particle characteristics

The following section shows the morphology and particle size of samples from SEM analysis. This is then divided into categories depending on the type of precursors and heat-treatment used. Next follows the BET surface area of the powders. Low magnification

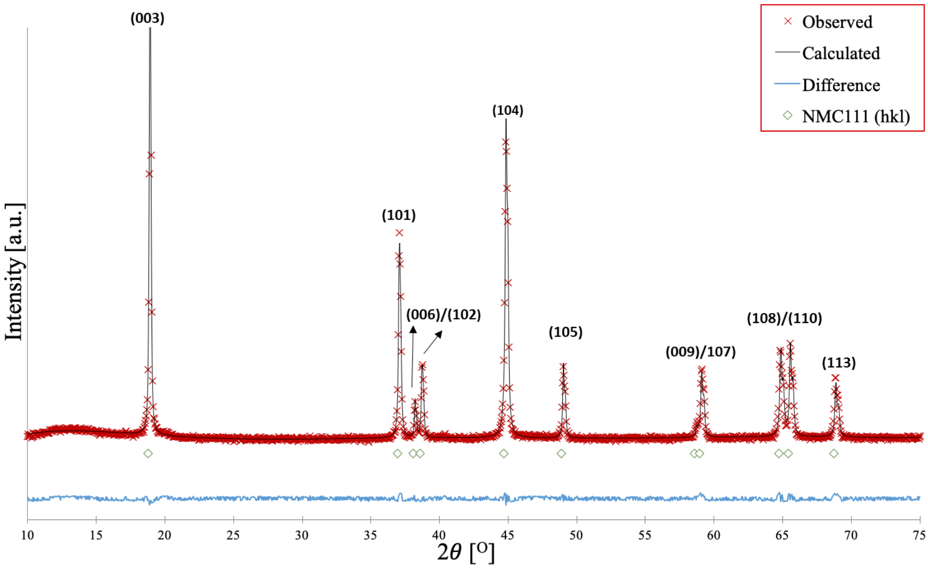

(**a**) Inert_Cl

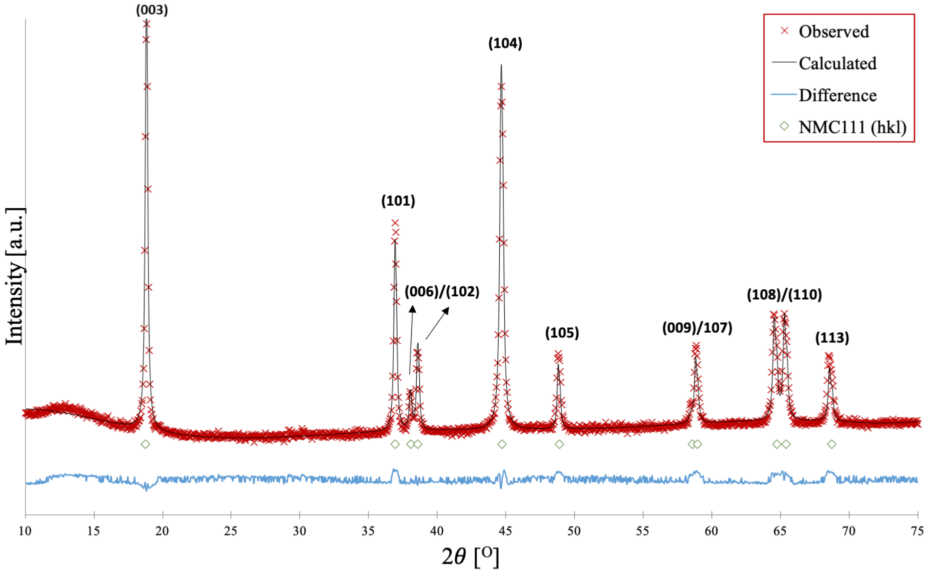

(**b**) Inert_Aq

**Figure 4.7:** The Rietveld refinements of phase pure NMC111 powders synthesized in an inert atmosphere with a) Cl-precursors (Inert_Cl) and b) pure Aq-based precursors (Inert_Aq).

**Table 4.1:** The crystal size [nm], lattice parameters [Å], cell volume [Å$^3$], Rwp [%] and cation mixing [%] from the Rietveld refinements presented above. This includes Air_Cl_HighPLi, Air_Cl, Inert_Aq and Inert_Cl powders. Uncertainties are shown in (brackets).

| **Sample** | **a [Å]** | **c [Å]** | **Cell Volume [Å$^3$]** | **Crystal size [nm]** | **Rwp [%]** | **Ni in Li layer [%]** |
|---|---|---|---|---|---|---|
| Air_Cl_HighPLi | 2.8966(2) | 14.191(2) | 103.1(2) | - | 13.96 | - |
| Air_Cl | 2.84943(13) | 14.2198(15) | 99.99(14) | 114.0(8) | 7.13 | 8.7 |
| Inert_Cl | 2.8511(3) | 14.1712(3) | 99.76(3) | 413.3(30) | 3.33 | 2.4 |
| Inert_Aq | 2.8608(9) | 14.2318(11) | 100.87(10) | 100.6(4) | 5.41 | 7.8 |

SEM for the air-synthesized powders showed similar results; these will be represented by one common figure. However, all high magnification SEM images used to determine particle size and shape are represented.

## 4.2.1 Morphology and particle size

The average particle size (APS), particle size distribution (PSD), and particle shape estimated from SEM images are presented in table 4.2. The shape of particles are defined according to its sphericity, roundness and angularity. Those with a high angularity may also be referred to as single-crystals. The table used for shape classification is attached in Appendix A in figure A.1. [73, 92]

**Table 4.2:** The estimated average particle size (APS) and particle size distribution (PSD). The particle shape is described in terms of angularity vs. roundness, and the degree of sphericity. The measurements below are estimated and are only applicable when compared against each other. Image J software is used to obtain this information from the SEM images.

| **Sample** | **PSD [nm]** | **APS [nm]** | **Angularity** | **Sphericity** |
|---|---|---|---|---|
| Inert_Cl | 200 - 500 | 400 | Sub-angular | low |
| Inert_Aq | 100 - 200 | 200 | Sub-round | low |
| Air_Cl | 200 - 500 | 400 | Angular | high |
| Air_Aq | 100 - 200 | 200 | Sub-round | high |
| Air_Aq (480°C) | 50 - 100 | 100 | Angular | low |
| Air_Cl_HighPLi | 200 - 500 | 400 | Angular | high |
| Air_Cl_5h | 50 - 400 | 200 | Angular | high |
| Air_Cl_ambP | 200 - 500 | 400 | Sub-angular | low |

### The influence of precursors and atmosphere

The influence of precursors is investigated by comparing Inert_Cl with Inert_Aq, and Air_Cl with Air_Aq. The two former and the two latter have identical synthesis methods with the only variable being the precursor. The precursors are clearly affecting the morphology and particle growth. The Cl-precursors obtained a PSD of approximately 200-500 nm and a APS of 400 nm. This is higher than those using purly Aq-based precursors with a PSD of 100-200 nm and an APS of 200 nm. Powders using Cl-precursors also generally show a higher degree of angularity. This is shown by comparing the SEM of the Inert_Cl with the Inert_Aq in figure 4.8 and by comparing Air_Cl (figure 4.9a) with Air_Aq (figure 4.10). The particle shapes are described in table 4.2.

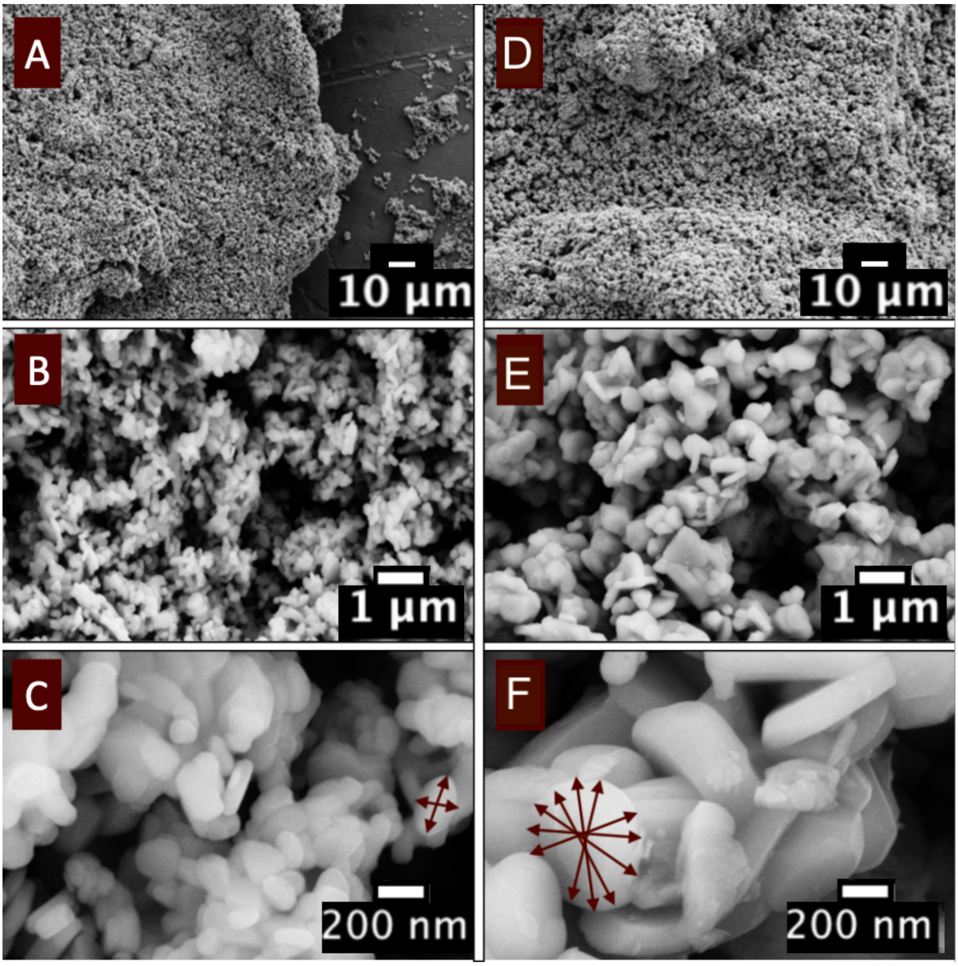

**Figure 4.8:** The SEM images for the powders synthesized in inert an atmosphere with and without Cl. The sample without Cl-precursors (Inert_Aq) are represented in the left column with increasing magnification (A, B and C, respectively). The right column shows the powder produced with Cl-precursors (Inert_Cl), with an increasing magnification (D, E and F, respectively). The arrows illustrate the diameter of a particle, and how the APS is measured.

How the atmosphere influences the morphology and the particle size is shown by comparing Inert_Cl with Air_Cl and Inert_Aq with Air_Aq. The results reveal that the atmosphere does not affect the APS and the PSD. However, the presence of an inert atmosphere will to some extent decrease the particles sphericity and angularity. The powder synthesized at an ambient pressure (figure 4.9d) has a less distinct angular shape and less spherical particles than those using hydrothermal conditions (figure 4.9a, 4.9b and 4.9c).

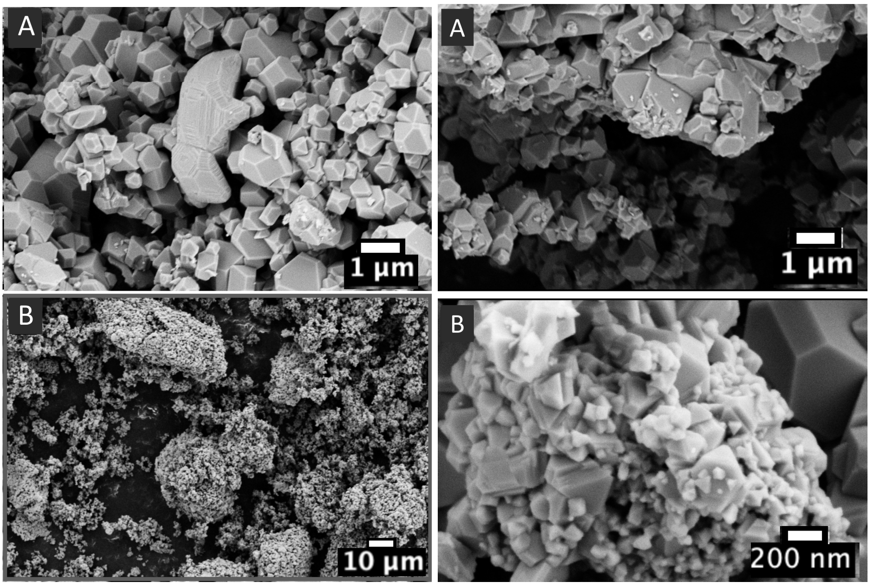

**(a)** Air_Cl

**(b)** Air_Cl_5h

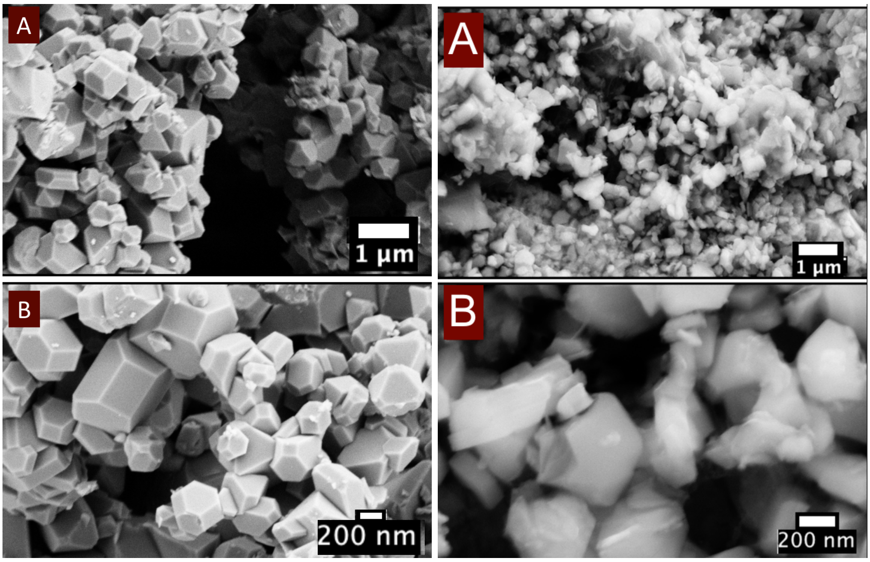

**(c)** Air_Cl_HighPLi

**(d)** Air_Cl_ambP

**Figure 4.9:** The SEM of air-synthesized powders with a) Cl precursors, high-pressure conditions and a 15 h heat-treatment (Air_Cl), b) a 5 h heat-treatment (Air_Cl_5h), c) with high pressures during Li-reaction (Air_Cl_HighPLi), and d) synthesis in ambient pressures (Air_Cl_ambP). It is important to notice that the scale bars are not comparable. All samples showed similar low-similar images as the one shown in a) image B.

### The influence of heat-treatment

The sample with a short heat treatment (15 h) at 850 °C in figure 4.9b has small particles of around 20 nm, that are aggregated in large spheres of 500 nm. Figure 4.10 shows the powder before and after the 15 h heat-treatment at 850 °C for synthesis in air without Cl (Air_Aq). First, the particles have a low sphericity and high porosity (seen in B, figure 4.10a). During the 850 °C heat-treatment, these are transformed into round particles with a high sphericity. Also, the APS increases from approximately 100 nm to 200 nm while the PSD increases from being relatively narrow at ∼ 50 - 100 nm to ∼ 100 - 200 nm.

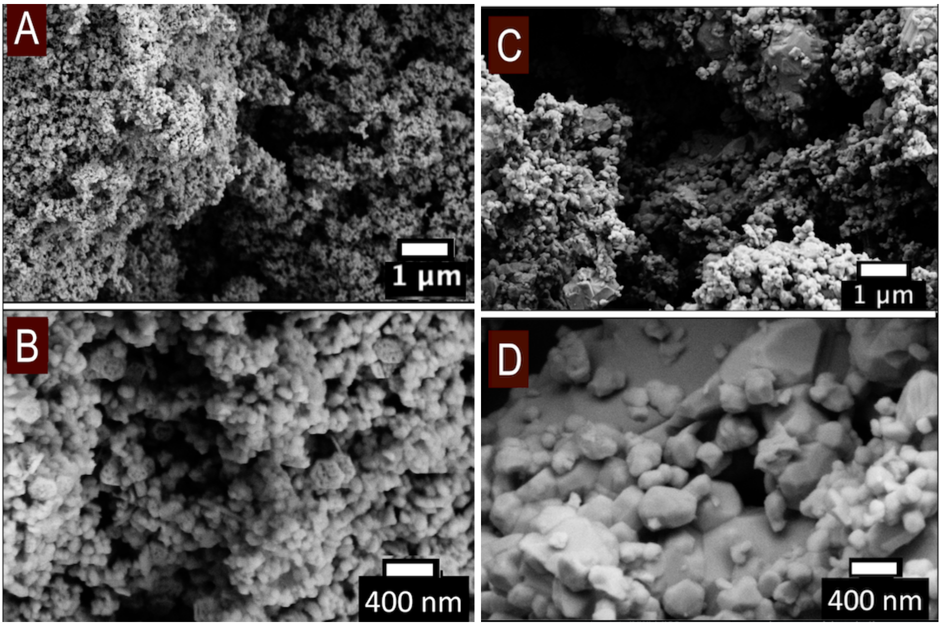

**(a)** Air_Aq (480 °C) **(b)** Air_Aq (850 °C)

**Figure 4.10:** All images represent the Air_Aq, made with standard Aq-based TM precursors in air. The images in column a) are taken after the 6 h heat-treatment at 480 °C. Column b) represent the Air_Aq after a 15 h heat-treatment at 850 °C. Images with a low (A and C) and high (B and D) magnification are shown. Image B shows particles with high porosity.

### 4.2.2 Surface area

The surface areas ($m^2/g$) are calculated by utilizing the BET theory model. All samples with NMC phases are shown in table 4.3. This includes Inert_Cl, Inert_Aq, Air_Cl, Air_Cl_5h, and Air_Aq. The Air_Aq before the 15 h heat-treatment at 850 °C (Air_Aq (480°C)) is also presented.

The results in table 4.3, show that the BET surface area of Inert_Cl (1.1552 $m^2/g$) and Air_Cl (2.0263 $m^2/g$), is lower than Inert_Aq (4.5790 $m^2/g$) and Air_Aq (2.5667 $m^2/g$), respectively. Thus, samples made in the presence of Cl have a lower BET surface area than those using Aq-based precursors. The BET surface area of Air_Aq is reduced from 23.8778 $m^2/g$ to 2.5667 $m^2/g$ during the 15 h heat-treatment at 850 °C. All BET surface areas are inversely proportional to the APS values estimated from the SEM data. Air_Cl_5h is an exception, having a low APS (200 nm) and a low surface area (0.6443 $m^2/g$).

**Table 4.3:** The surface area ($m^2/g$) is calculated by utilizing the BET theory model for sample Inert_Cl, Inert_Aq, Air_Cl, Air_Cl_5h, Air_Aq and Air_Aq (480 °C).

| **Sample** | **Surface area [$m^2/g$]** | **Margin of error [$m^2/g$]** |
|---|---|---|
| Inert_Cl | 1.16 | ± 0.03 |
| Inert_Aq | 4.58 | ± 0.04 |
| Air_Cl | 2.03 | ± 0.02 |
| Air_Aq | 2.57 | ± 0.03 |
| Air_Aq (480°C) | 23.88 | ± 0.38 |
| Air_Cl_5h | 0.64 | ± 0.01 |
| Air_Cl_ambP | 2.01 | ± 0.03 |

## 4.3 Electrochemical performance

To get an overview of the data in this section, the discharge capacities for all synthesis routes are presented in table 4.4. The three parallel coin cells for each synthesis are represented by **coin cell 1** due to similarities; this is true for the synthesis' above the line in table 4.4. The charge/discharge data of coin cell 2 and 3 which deviate from **coin cell 1** are marked(*) and are supplied in the Appendix. The data with complete cell failure for all three parallels (Air_Cl_HighPLi) is given in the Appendix B as **coin cell 1**. Both Inert_Cl and Inert_Aq have one parallel synthesis. These (Inert_Cl2 and Inert_Aq2) **Coin cell 1** from each of these are found in the Appendix B in figure B.3 and B.2, respectively.

**Table 4.4:** All assembled coin cells are described below. The loading of active material [mg] per electrode, and the discharge capacities (DisCap [mAh/g]) from cycle 1-50 are shown. **Coin cell 1** is the representative for all three coin cells. Samples marked (*) will be found in the Appendix. The cells that short circuit before completing their first charge are marked ”No activity”.

| **Synthesis name** | **Coin cell** | **Active material [mg]** | **DisCap [mAh/g] (Cycle 1-50)** |
|---|---|---|---|
| Air_Cl | 1 | 3.3640 | **86-75** |
| | 2 | 3.3889 | 89-64 |
| | 3 | 3.5310 | 84-71 |
| Air_Aq | 1 | 3.2240 | **85-37** |
| | 2* | 4.5945 | Fail 26th cycle |
| | 3 | 4.5328 | No activity |
| Air_Cl_ambP | 1 | 4.4210 | **46-39** |
| | 2 | 4.4102 | No activity |
| | 3 | 4.5045 | No activity |
| Air_Cl_5h | 1 | | **80-37** |
| | 2 | 3.9512 | 76-29 |
| | 3 | 4.5066 | No activity |
| Air_Cl_HighPLi | | 3.9411 | **129-83** |
| Inert_Cl | 1 | 2.1552 | **143-132** |
| | 2 | 2.4375 | 142-130 |
| | 3* | 2.0940 | 134-106 |
| Inert_Aq | 1 | 2.6924 | **133-97** |
| | 2 | 2.6977 | 133-90 |
| | 3 | 2.6921 | 130-94 |
| Inert_Cl.2 | 1* | 3.6992 | **144-119** |
| | 2 | 3.8131 | 142-115 |
| | 3 | 2.973 | 140-129 |
| Inert_Aq.2 | 1* | 4.2279 | **140-111** |
| | 2 | 4.4310 | 141-110 |
| | 3 | 4.3011 | 139-107 |
| Air_Aq_HighPLi | 1* | 4.2279 | **Fail 3rd cycle** |
| | 2 | 4.4214 | Fail 2nd cycle |
| | 3 | 4.6531 | No activity |

### 4.3.1 Air-synthesized active cathode materials

The figures 4.11, 4.12 and 4.13 illustrate the galvanostatic cycling data from the five samples syntesized in air (Air_Cl, Air_Aq, Air_Cl_5h, Air_Cl_HighPLi and Air_Cl_ambP). None of these obtained a phase pure NMC111 and all exhibited a low initial specific capacity relative to that expected of NMC111 at 0.1 C (16 mA/g). [48] The coin cell made of the Air_Cl powder has the highest stability of those synthesized in air as displayed in figure 4.11. It has a minimal polarization in the charge and discharge cycles, and has a specific initial discharge capacity of 86 mAh/g. After 50 cycles, the discharge capacity drops to 75 mAh/g.

Figure 4.12b shows the galvanostatic cycling data of Air_Cl_5h, which is heat-treated for

5 h. It has a low initial capacity that declines rapidly after the first cycle. The typical shape of an NMC discharge curve loses its integrity at cycle 5 before it disappears completely after cycle 50. The same is shown for sample Air_Aq after cycle 10 in figure 4.12a. This steep slope appears when no TMs are oxidizing to generate current.

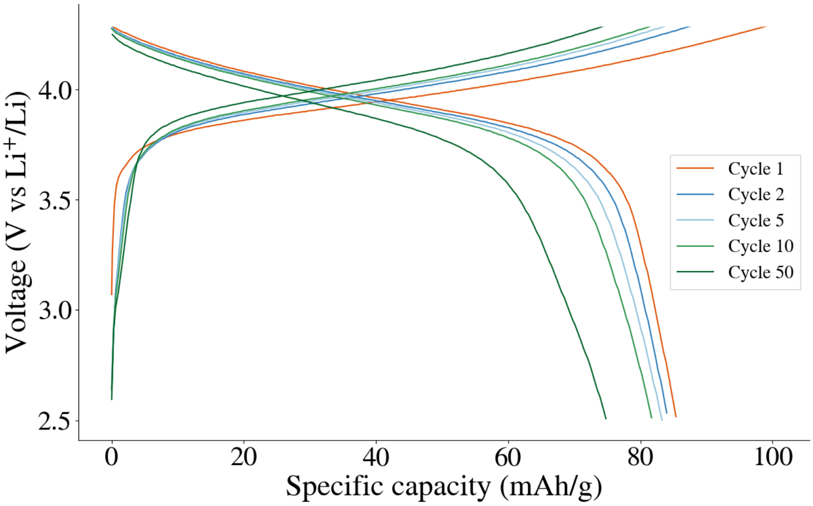

**Figure 4.11:** A charge/discharge plot of the impure NMC powder synthesized in air using Cl-precursors, a hydrothermal step (before the Li-addition) and a 15 h heat-treatment (Air_Cl), The specific capacity [mAh/g] is plotted against voltage (V vs Li/Li$^+$) for cycle 1 at 0.1C and cycle 2, 5, 10 and 50 at 0.2C.

Figure 4.13a of Air_Cl_HighPLi has an initial discharge capacity of 129 mAh/g. After 100 cycles the discharge capacity drops to 83 mAh/g, with a small voltage drop. This displays a classical spinel-shaped charge/discharge plot. Due to the plateau in the discharge curve below 3 V, the practical discharge capacity will be 80 mAh/g. In the area $\sim$ 3.9 - 4.2 V, there are two additional plateaus. These correspond to the two 8a tetragonal sites that Li$^+$ will (de)intercalate with in the $Li_xMn_2O_4$ structure for $x < 1$. [93] The charge capacity drops rapidly between cycle 2-50 and has a broad plateau near 3 V with respect to cycles 50-100.

The galvanostatic cycling data of the Air_Cl_ambP synthesized at ambient pressures is shown in figure 4.13b. It has a relatively low initial discharge capacity (46 mAh/g) and a small capacity drop (6 mAh/g) over 50 cycles.

All cells show a voltage increase and decrease over multiple charge and discharge cycles, respectively. The galvanostatic cycling tests were also used to find the change in coulombic efficiency and specific capacity over 80 cycles. This is seen in figure 4.14. [89] The initial cycle exhibits the highest specific capacity and the lowest coulombic efficiency; this

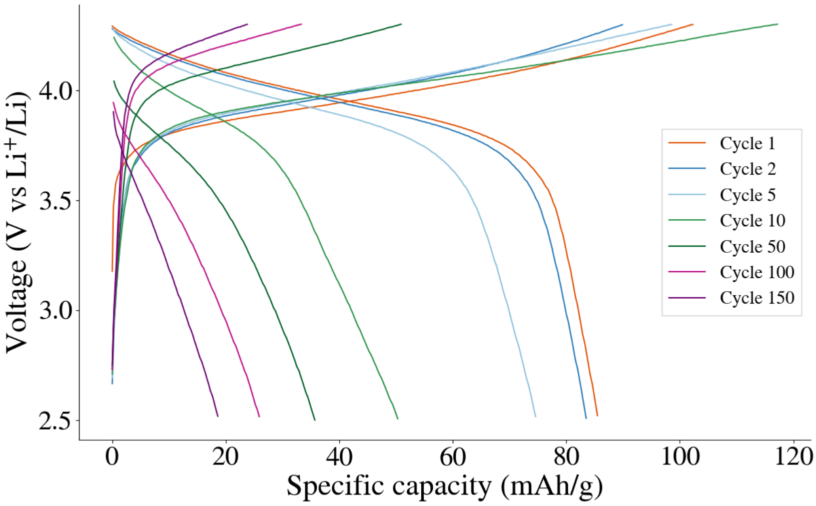

**(a)** Air_Aq

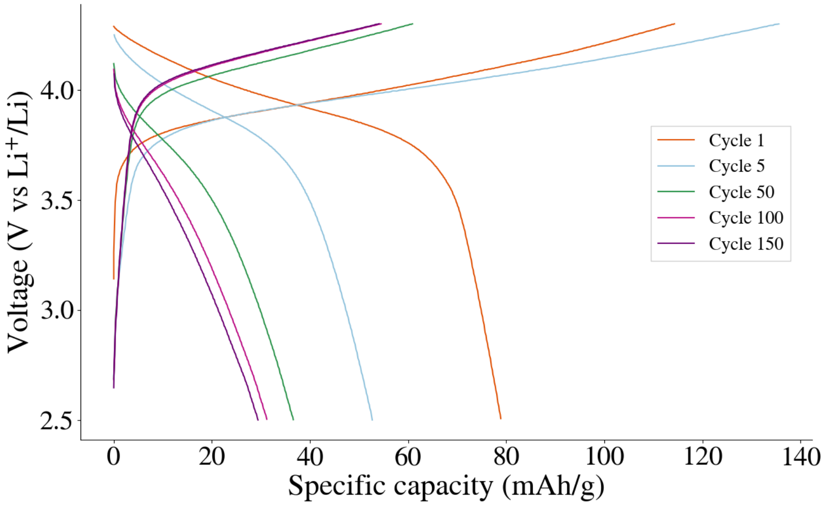

**(b)** Air_Cl_5h

**Figure 4.12:** Charge/discharge plot of cells using active material synthesized with different conditions relative to that of Air_Cl. The changes are a) pure Aq-based precursors (Aq_Air) and b) a 5 h heat-treatment (Air_Cl_5h). The specific capacity [mAh/g] is plotted against voltage (V vs Li/Li$^+$) for cycle 1 at 0.1C and cycle 2, 5, 10, 50, 100 and 150 at 0.2C.

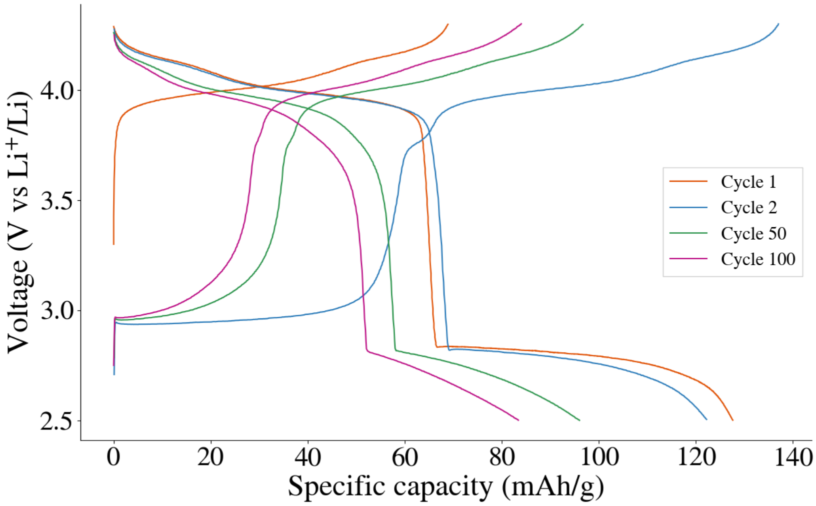

**(a)** Air_Cl_HighPLi

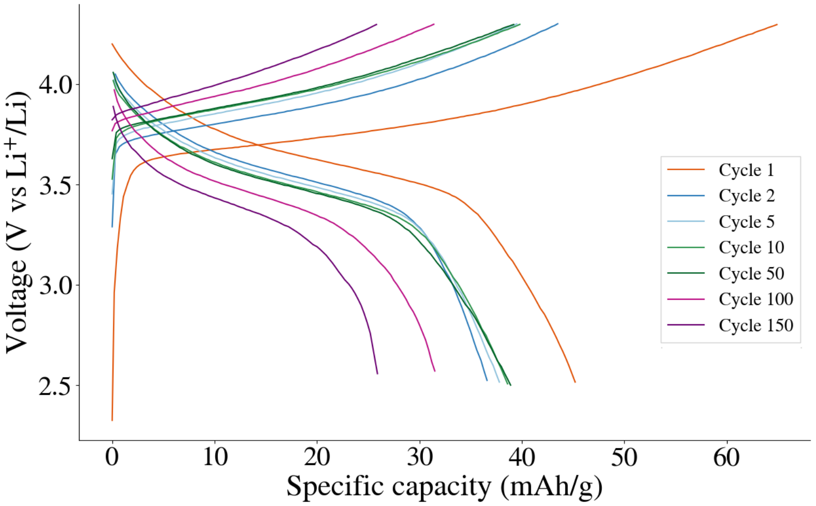

**(b)** Air_Cl_ambP

**Figure 4.13:** A charge/discharge plot of cells using active material synthesized with different conditions relative to that of Air_Cl. The changes are a) high pressures (Li_Cl_HighPLi) and b) ambient pressures (Air_Cl_ambP) during the Li-reaction. Specific capacity [mAh/g] is plotted against voltage (V vs Li/Li$^+$) for cycle 1 at 0.1C and cycle 2, 5, 10, 50, 100 and 150 at 0.2C.

is true for all coin cells. The coulombic efficiency of Air_Cl_ambP is shown in purple in figure 4.14. The first cycle shows a coulombic efficiency as low as 70 %, but increases up to ∼ 96 % in the 6th cycle, before it stabilizes at 98 % after ∼ 20 cycles. A deviating factor is found for the Air_Cl_5h; the columbic efficiency fluctuates dramatically between cycles. The average coulombic efficiency is low (56.4 %) and indicates the presence side reactions that are consuming Li. This instability is reflected in the low specific capacity (orange circles). The capacity retention of Air_Cl is highest, being 82 % after 80 cycles. Air_Cl_ambP (green circles) has the highest stability with the lowest initial capacity. The spinel-phased Air_Cl_HighPLi has the highest average capacity of the impure powders when cycling between 2.5 and 4.3 V.

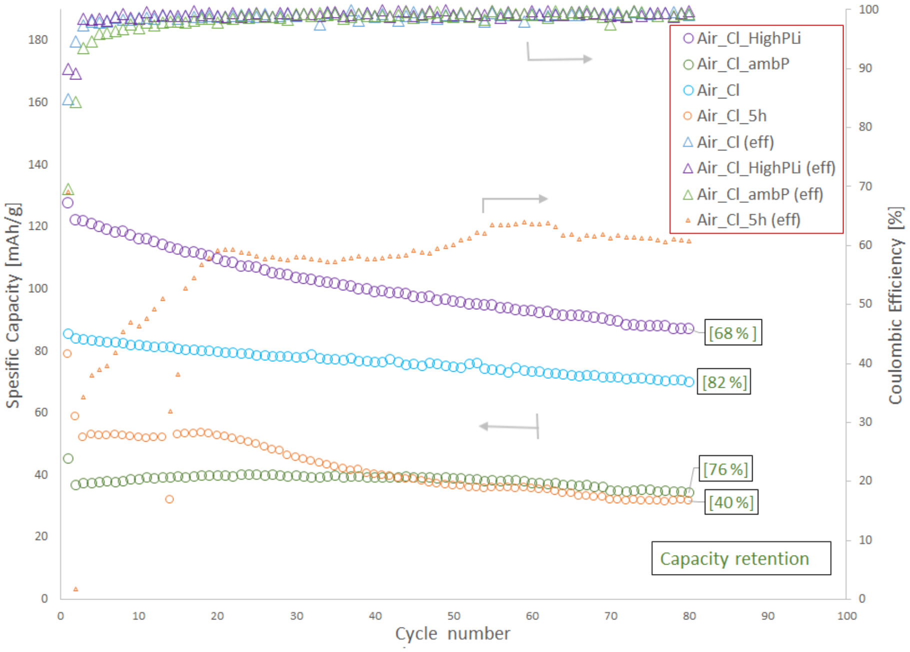

**Figure 4.14:** The data are obtained from cells using air-synthesized impure NMC and spinel powders as active cathode materials. The circles and triangles are plotted relative to the right (specific capacity [mAh/g]) and the left (coulombic efficiency [%]) y-axis', respectively. The strongly fluctuating data has a smaller marker (Air_Cl_5h). The capacity retention [%] after the 80th cycle is included (black boxes).

### 4.3.2 Inert-synthesized NMC111 cathode material

Figure 4.15 displays the galvanostatic cycling plots of the pure NMC111 powders made in inert atmospheres. With an initial discharge capacity of 143 mAh/g between 2.5 and 4.3 V, the powder made in the presence of Cl (Inert_Cl) holds the best cycling performance of all cells. Furthermore, the voltage plateau drops for each discharge and charge cycle. This is due to a polarization taking place during cycling, which creates an increasing overpotential. A higher polarization, hence overpotential, are seen for Inert_Aq.

Cycle 1, 2 and 50 from the galvanostatic cycling data for inert-synthesized powders (figure 4.15) is shown in a dQ/dV-plot in figure 4.16. This plot shows the voltages at which the redox reactions occur. For Inert_Aq (figure 4.16a), the peak height of cycle 50 is reduced to almost half of the initial cycle. Also, during the charge and discharge cycles, there is a respective peak-shift to higher and lower potentials. The area under the graph represents the specific capacity, which falls continuously with an increasing cycle number. The charge and discharge curve for Inert_Aq are not symmetrical and the main peaks are found at voltages 3.8 V and 3.7 V, respectively. Due to this mismatch, the redox reactions are not fully reversible. The Inert_Cl cell (figure 4.16b) mostly shows the same trends as Inert_Aq, however, these are weaker and thus indicates more reversible redox reactions. The highest peak is found at 3.7 V for all cycles during charge and discharge. The charge curves show a small shift towards 3.9 V after 50 cycles.

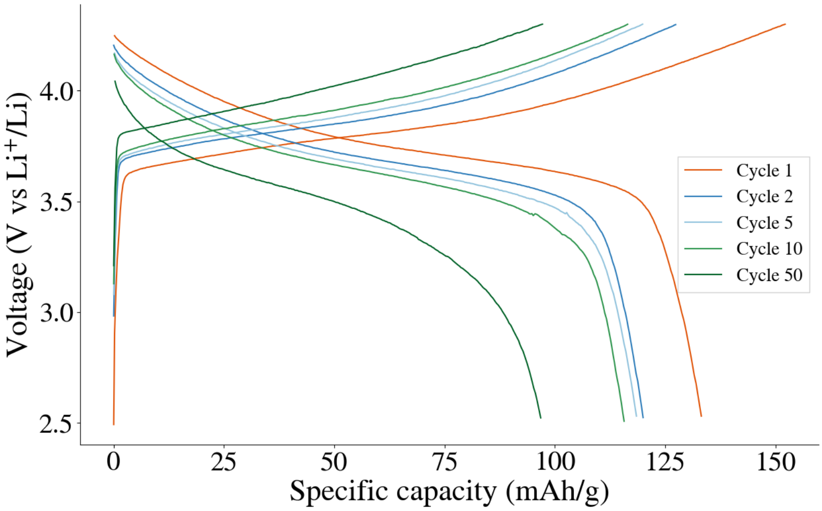

**(a)** Inert_Aq

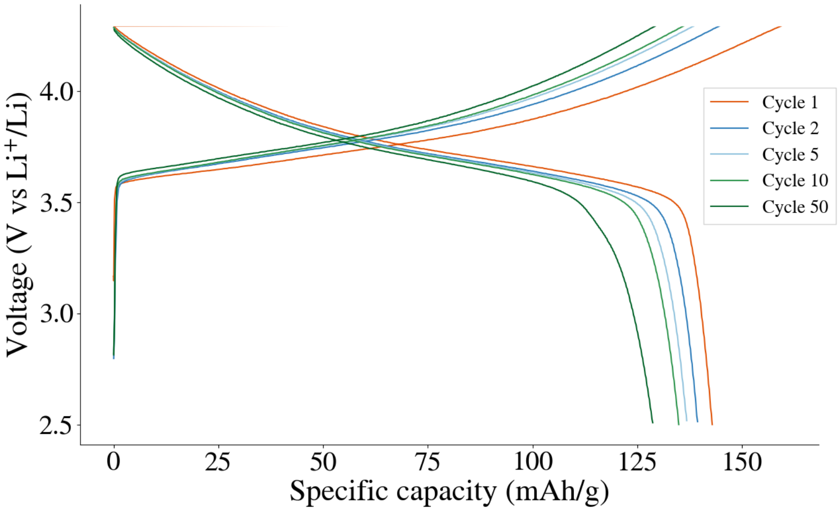

**(b)** Inert_Cl

**Figure 4.15:** A charge/discharge plot for coin cells using pure NMC111 powders synthesized in an inert atmosphere using a) standard Aq-based precursors and b) Cl-precursors. These show the specific capacity and voltage drop for cycle 1 at 0.1C and cycle 2, 5, 10 and 50 at 0.2C.

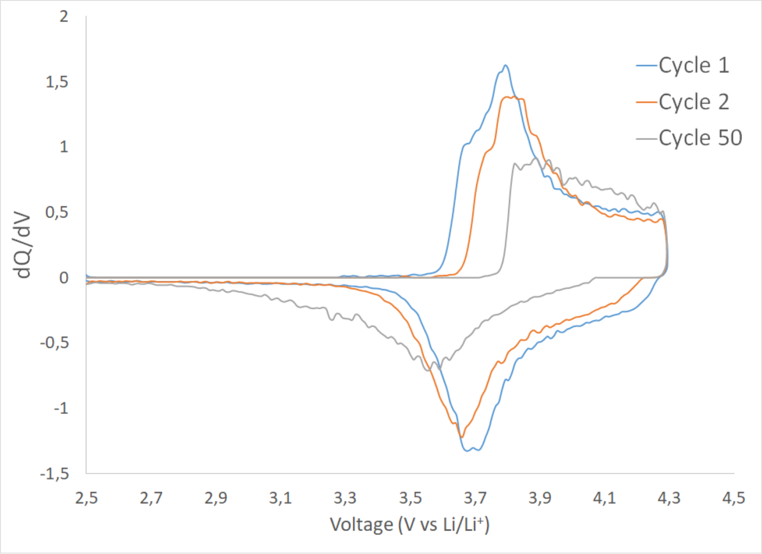

**(a)** Inert_Aq

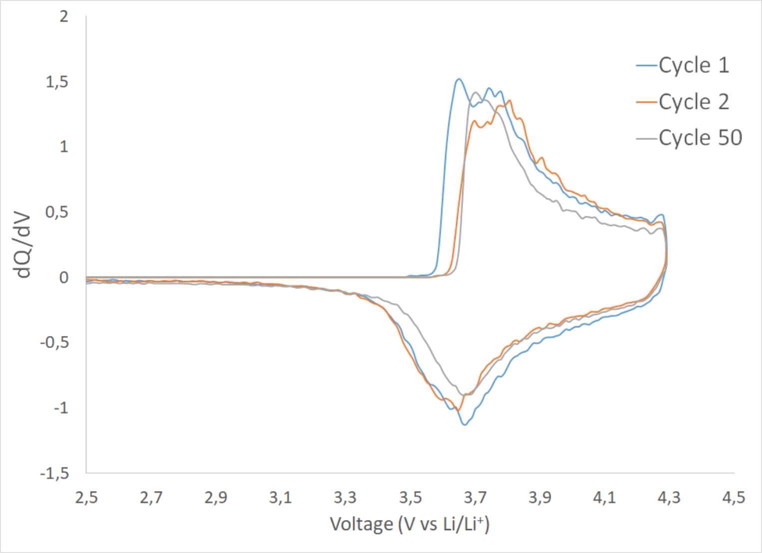

**(b)** Inert_Cl

**Figure 4.16:** The dQ/dV-plot of cycle 1, 2 and 50 for cells using the active powders a) Inert_Cl and b) Inert_Cl.

The coulombic efficiency (triangles) in figure 4.17 for cells using inert-synthesized NMC111 is on average ∼ 99.3 %. Consequently, there are no major side reactions present. However, for the first two cycles, the coulombic efficiency is between ∼ 88-95 %, which indicates a shortage of Li available for cycling. [47] The specific capacity is also relatively stable over 80 cycles, with a capacity retention of 76% and 70 % for Inert_Cl and Inert_Aq, respectively.

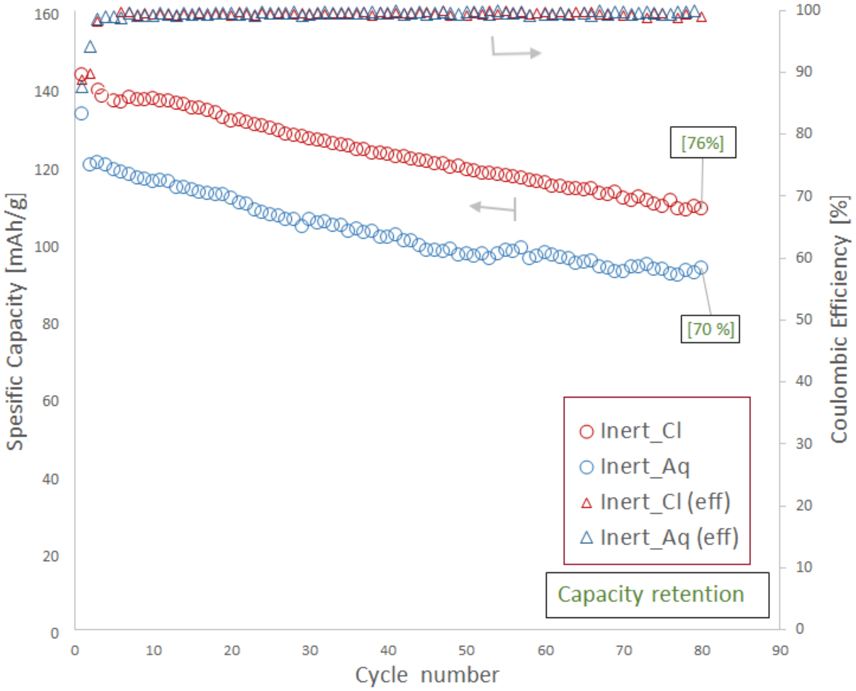

**Figure 4.17:** The data from cells using inert-synthesized pure NMC111 powders as active cathode materials. Red markers are with Cl-precursors whereas blue is without Cl. The circles and triangles are plotted relative to the left (specific capacity [mAh/g]) and right (coulombic efficiency [%]) y-axis', respectively. The capacity retention [%] after the 80th cycle is included (black boxes).

### Cell resistance

The EIS testing (figure 4.18) is performed on cells with the highest phase purity of NMC111 and with the best cycling performance (Inert_Cl and Inert_Aq). The pre-charge step (figure 4.18b) of Inert_Cl and Inert_Aq display similar charge capacities of 159.4 mAh/g and156.1 mAh/g, respectively. The pre-charging of Inert_Aq starts at lower voltages than Inert_Cl. However, it has a steeper positive gradient during charge and eventually ends at higher voltages. The data from the EIS measurements are plotted in figure 4.18a. It shows the typical Nyquist plot for the two cells at 25 °C and $\sim$ 3.4 V. The curving of the plot exhibits a loop followed by a tail (Warburg element) which corresponds to the typical Randall circuit mentioned in Chapter 2. The EIS is intended for a relativity measurement between the two samples, and therefore no attempts have been made to find an equivalent circuit fit. Overall, the half circle of Inert_Cl in the Nyquist plot are smaller due to lower resistance. The cathode charge transfer resistance are smaller for Inert_Cl (333.4 $\Omega$) than for Inert_Aq (410.3 $\Omega$). [94] The ohmic resistances measured at high frequencies are approximately equal for the two cells, being slightly lager for Inert_Cl (24.8 $\Omega$) than for Inert_Aq (22.3 $\Omega$). Linear regression of the two Warburg elements at low frequencies shows that these are slopes with the approximate same values.

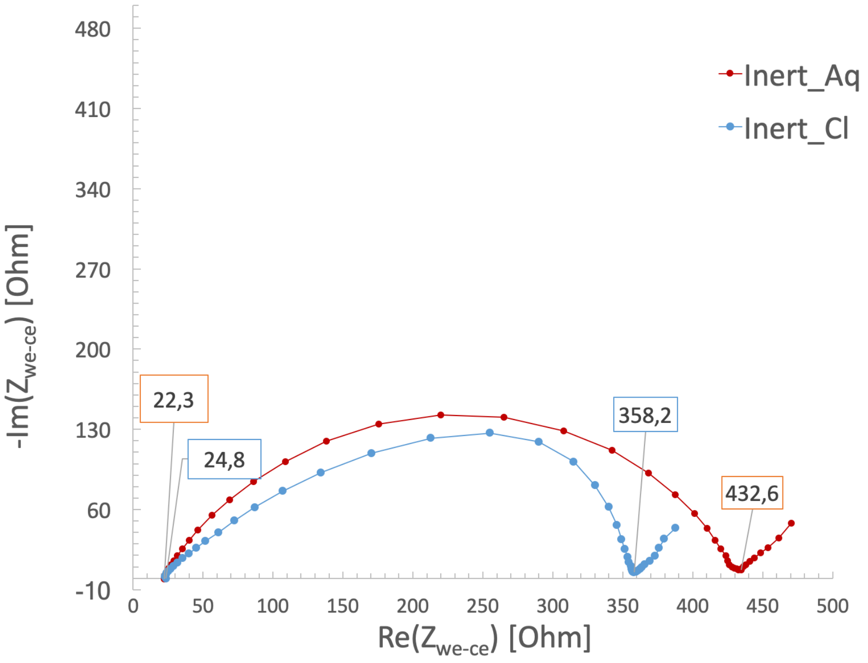

**(a)** The framed data points are the resistance values used for calculating the charge transfer resistance (Ω).

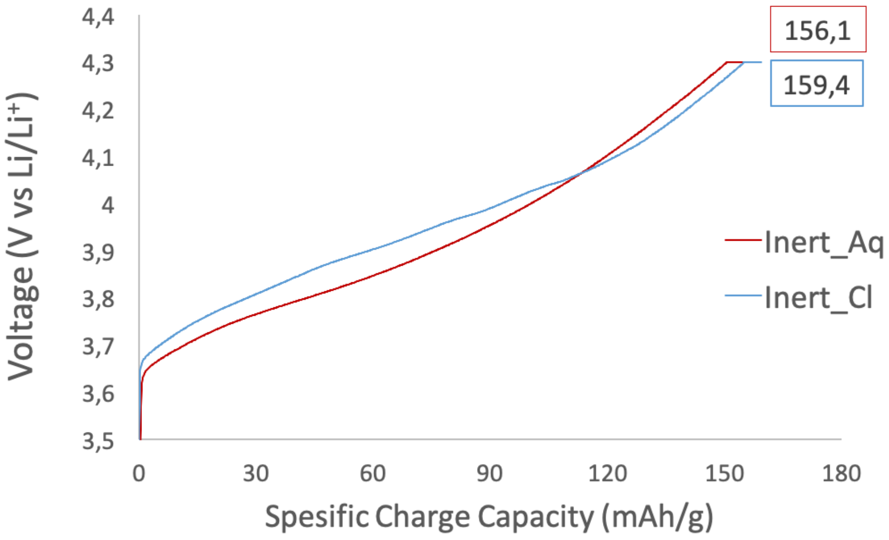

**(b)** The framed data points show the initial charge capacity (mAh/g).

**Figure 4.18:** The data from EIS analysis of the Inert_Cl and Inert_Aq half-cells show a) the Nyquist plot from the EIS measurements, and b) the potentiostatic pre-charging step.

### 4.3.3 Summary of results

The analysis performed on each of the seven samples, and their main results are represented in a flow chart in figure 4.19.

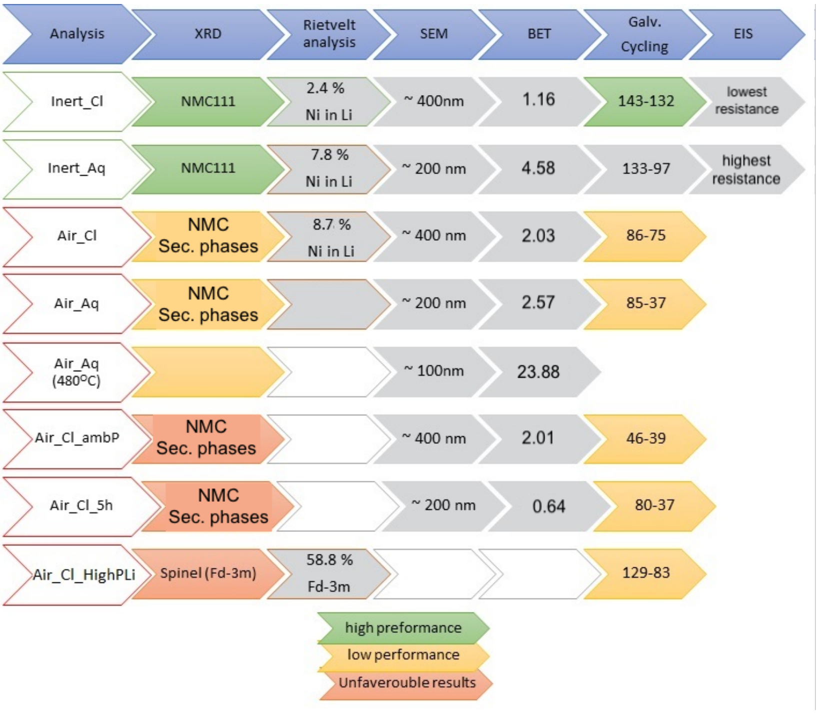

| Analysis | XRD | Rietvelt analysis | SEM | BET | Galv. Cycling | EIS |
|---|---|---|---|---|---|---|
| Inert_Cl | NMC111 | 2.4 % Ni in Li | ~ 400nm | 1.16 | 143-132 | lowest resistance |
| Inert_Aq | NMC111 | 7.8 % Ni in Li | ~ 200 nm | 4.58 | 133-97 | highest resistance |
| Air_Cl | NMC Sec. phases | 8.7 % Ni in Li | ~ 400 nm | 2.03 | 86-75 | |
| Air_Aq | NMC Sec. phases | | ~ 200 nm | 2.57 | 85-37 | |
| Air_Aq (480ºC) | | | ~ 100nm | 23.88 | | |
| Air_Cl_ambP | NMC Sec. phases | | ~ 400 nm | 2.01 | 46-39 | |
| Air_Cl_5h | NMC Sec. phases | | ~ 200 nm | 0.64 | 80-37 | |
| Air_Cl_HighPLi | Spinel (Fd-3m) | 58.8 % Fd-3m | | | 129-83 | |

**Figure 4.19:** The figure illustrates the analysis techniques preformed on all samples, with main results. Cycling data is reported in mAh/g. The colored boxes represent the different performances, and is validated relative to values expected from other literature. A gray box framed in colors means that the performance is validated relative to another sample.

# Chapter 5

# Discussion

This chapter addresses the electrochemical characterization of the assembled batteries in terms of the synthesized cathode material. The first section evaluates the inert-synthesized NMC111 as a cathode material in rechargeable LIBs batteries focusing on the effect of TM-precursors. Secondly, the synthesis process in air will be examined, with a particular interest in the aspects causing an impure NMC111. Both sections relate the extrinsic and intrinsic powder properties to their electrochemical performance. Thereafter, the evaluation of errors and the suggested future work will be evaluated. First off, trends found in the results are summarized as follows:

- **Particle size:**
  Air_Cl ∼ Inert_Cl (400 nm) > Inert_Aq ∼ Air_Aq (200 nm)

- **Surface area:**
  Air_Cl_ambP > Inert_Aq > Air_Aq > Air_Cl > Inert_Cl > Air_Cl_5h

- **Crystal size [nm]:**
  Inert_Cl (413.3) > Air_Cl (114.0) > Inert_Aq (100.6)

- **Cation mixing [%]:**
  Air_Cl_ambP > Air_Cl_5h > Air_Aq ∼ Air_Cl (8.7 %) > Inert_Aq (7.8 %) > Inert_Cl (2.4 %)

- **Initial discharge capacity [mAh/g]:**
  Inert_Cl (143) > Inert_Aq (133) > Air_Cl_HighPLi (129) > Air_Cl (86) Air_Aq (85) > Air_Cl_5h (80) > Air_Cl_ambP (46)

- **Capacity retention after cycle 80[%]:**
  Air_Cl (82 %) > Inert_Cl = Air_Cl_ambP (76 %) > Inert_Cl (70 %) > Air_Cl_HighPLi (68 %) > Air_Cl_5h (40 %)

- **Initial coulombic efficiency [%];**
  Air_Cl_HighPLi (90.0 %) > Inert_Cl (88.8 %) > Inert_Aq (87.7 %) > Air_Cl (83.6 %) > Air_Cl_ambP (69.6 %) > Air_Cl_5h (69.5 %)

All batteries have some common features from the galvanostatic cycling data shown in the results chapter. One of the clearest trends are the increasing overpotentials seen over multiple cycles. Here, a higher voltage is required for the same amount of Li to intercalate the structure and provide a constant current. This leads to polarization and is seen as an increased overpotential (shaded blue and orange) in figure 5.1. At higher cycle numbers, the cutoff voltage might be reached before enough Li intercalate, which will cause a capacity loss, and a lower capacity retention.

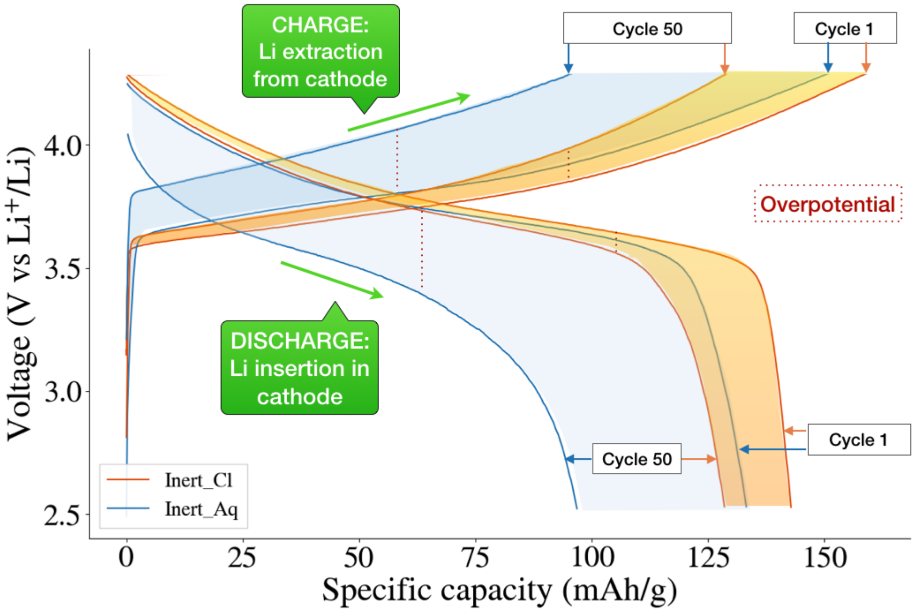

**Figure 5.1:** The galvanostatic cycling data of cycle 1 and 50 for Inert_Aq and Inert_Cl, with emphasis on the overpotentials developed. The charge and discharge directions are annotate in the figure.

Another trend, is the large capacity drop after the first cycle. From figure 4.14 and 4.17 there is also a low coulombic efficiency during the first cycles. These two phenomena are connected and are caused by an interphase formation on the cathode electrode interface (CEI). [35, 54–57] The coulombic efficiency is related to the loss of Li during a cycle, and is therefore used to detect the presence of major side reactions. From figure 4.14, all batteries seem to form a stable layer after about the 5th cycle. This is seen as a stabile coulombic efficiency, with Air_Cl_5h being an exception.

## 5.1 Co-precipitation in inert atmospheres

Relative to other reports with co-precipitation reactions, the inert synthesized NMC111 (Inert_Cl and Inert_Aq) has a low capacity retention and initial discharge capacitiy (figure 5.1). For example, NMC111 powders synthesized through a traditional co-precipitation in inert atmosphere is earlier reported to obtain an initial discharge capacity of 167 mAh/g between 3 and 4.3 V at 0.1 C. [66]. Since the cutoff voltage used here is lower (2.5 V), one should expect higher capacities for Inert_Cl and Inert_Aq. The above-mentioned report [66] explained the high electrochemical performance being a result of the powders morphological qualities giving high tap-densities. High tap-densities are obtained with a uniform distribution of spherical powders and is reported as a key factor for not only high capacities but also for the mass production of NMC111. [48, 66, 67]. Seen from SEM, such morphological characteristics giving high tap densities are not obtained in this research, and may contribute to the low initial discharge capacity. The initial coulombic efficiency of 88.8 % is comparable to other NMC materials that were also obtained through co-precipitation methods. This indicates predictable CEI formations. [90]

From the XRD in figure 4.5, one can clearly see that the Cl does not encourage the oxidation of Mn and promote the formation of Mn-oxide phases as suggested by Nicholas. [71]. This is also seen when comparing a) (Inert_Cl) and b) (Inert_Aq) in figure 4.7 where both match the $R\bar{3}m$ space group of NMC111 with no secondary phases. [90] Thorough investigation of the differences between Inert_Cl and Inert_Aq, reflect the effect of Cl. Shown in figure 5.1, Inert_Cl has an initial discharge capacity (143 mAh/g) and capacity retention (76 %) relatively high compared to Inert_Aq made from Aq-based TM precursors (133 mAh/g and 70 %). The precipitation test using $Ag(NO_3)$, revealed that no trace of $Cl^-$ is left in the waste water. Thus, the different performances are an indirect result of the presence of $Cl^-$ during the co-precipitation reaction. Active NMC111 powders made in the presence of $Cl^-$ have less cation mixing and larger particle sizes. The resulting coin cells show a lower resistance and better cycling performance. It is unlikely to assume that Cl has contributed to the reduction of cation mixing. These values may, however, be explained by the high degree of washing before adding $LiNO_3$. The additional washing and sieving steps will remove impurities caused by the filtration paper, and any other chemical contamination in the solution. This ensures more accurate stochiometriy between the co-precipitated hydroxide phase and Li.

### 5.1.1 Cation mixing

The difference between the peaks (003)/(104) imply a higher degree of cation mixing for Inert_Aq than for Inert_Cl. The phenomenon of cation mixing is shown in figure 2.9. [40] The Rietveld refinements of the XRD patterns from the Inert_Cl and Inert_Aq powders are estimated to be at an amount of 2.4 % and 7.8 % $Ni^{2+}$ in $Li^+$-layers, respectively. Xiaoyu Zhang *et. al.* [60] reports that a cation mixing below 2 % does not affect the electrochemical performance for NMC111. Since all samples have larger values, this may contribute to why no cells reach the above mentioned expected capacity for NMC111.

Inert_Aq has a cation mixing almost four times the preferred limit for NMC111 (2 %). This may be the reason for a low cycling performance of Inert_Aq relative to that of Inert_Cl. Most research agree with the trends in this report, where a high cation mixing contributes to a lower diffusivity of Li. This gives a lower electrochemical performance. With a low diffusivity, Li will not have time to completely intercalate the cathode structure during discharge, or deintercalate during charge, before reaching the cutoff voltage. This drives up the overpotentials, and reduces the battery capacity causing a declining capacity retention after 80 cycles (70 %) for Inert_Aq in figure 4.14. Restrictions of Li diffusivity is a phenomenon that is better seen at higher cycling rates. A rate capability test is therefore beneficial in order to reveal more information about how the cation mixing affects the electrochemical performance of the half-cells. [90] On the contrary, Roscian *et. al.* [95] reported that $\sim 4$ % $Ni^{2+}$ in the $Li^{+}$ interlayer stabilized the structure. This prevented NMC111 from undergoing any phase transitions when deeply delithiated (at 4.5 V). [95]

### 5.1.2 Morphological characteristics

As the cation mixing in Inert_Cl is only 0.4 % above the preferred value, its low capacity retention at 76 % is likely to be related to other phenomena such as morphology and particle size. The BET surface areas from table 4.3 decreases for powders synthesized with Cl-precursors. This is in agreement with the increasing APS reported from the SEM results in table 4.2. This trend is shown for both air and inert synthesized powders, and is therefore independent of the atmosphere. The presence of $Cl^{-}$ during the co-precipitation clearly increases the rate of particle growth, and the nitrate anions (${NO_3}^{-}$) have less of an impact on the various growth steps. Hu *et. al.* [96] found similar trends where anions in the solution enhances the coarsening kinetics. ${NO_3}^{-}$ are present in higher concentrations in the Aq-based TM solutions, but researchers reports ${NO_3}^{-}$ to have a lower impact compared to other anions such as sulphate (${SO_4}^{-}$) [72]. This also substantiates the theory about $Cl^{-}$ being the anionic species present that enhances growth.

In fact, the differences in particle size could be a feasible explanation for the different electrochemcical behaviors. The capacity is earlier reported to increase with smaller particles due to more accessible active material and enhanced Li-diffusion. [90] This is inconsistent with findings for the inert-synthesized samples reported here. Figure 4.19 reveals that larger particles give the highest capacity retention. Hanafusa *et. al.* [97] and Grugenon *et. al.* [98], reports that a high specific surface area, hence a small APS, will enlarge the formation of metal-electrolyte interphases and increase the capacity fading. However, this will also accelerate the solvent degradation process and induce side reactions. Consequently, interphases with poor electronic conductivity and less contact between the grains are formed. As experimentally observed in figure 5.1, a lower capacity fading will be favored by larger particles (400 nm).

There are also uncertainties regarding the engineering of the electrode. The ratio between the active material, the binder, and the conducting material should be carefully considered. The binder (PVDF) is an insulator, and will therefore have a strong influence on the electrochemical performance. The amount of binder is not optimized for the varying particle size and surface area of the active powders, as all coin cells share the same ratio. However, particles with a higher surface area may require more binder.

Li *et. al.* [99] synthesized NMC811 with Cl-precursors and obtained a particle size (200 nm) half of that obtained here (400 nm). The report used Cl powders dissolved in water, instead of HCl, and thus had a lower concentration of Cl. Therefore, the particles discussed in their report may not grow to the same extent. There are, however, some uncertainties to this reasoning as the aforementioned report also used shorter heat-treatments. This is also known to reduce the particle growth. [100] In addition, the active material showed a better initial discharge capacity (184 mAh/g). The smaller particles alone are not likely to cause such a high electrochemical performance. A more probable cause is the higher content of Ni (NMC811), being the electrochemical active species, together with a low cation mixing (1.2 %) being half of that reported here (2.4 %).

### 5.1.3 Structure stability

All lattice parameters calculated in the Rietveld analysis from table 4.1 are in accordance with the XRD lattice refinements reported by Ohzuku and Yabuuchi [45]. This confirms the composition of the pristine material of NMC111. Yin *et. al.* [41] and Jung [47] reports that NMC111 with a $R\bar{3}m$ symmetry remain stable throughout the cycling up to 4.4 V. They report that the delithiation during charge is kept below 70 %, and a small volume expansion of 1% is detected. Since a lower cutoff voltage (4.3 V) is used here, phase transformations is unlikely to be the reason for the decreasing electrochemical performance during cycling. This is, however, only true for the cells using pure phase NMC111 as active cathode material (Inert_Cl and Inert_Aq).

On the other hand, these materials are likely to experience changes in the lattice during cycling. Such structure changes might be contributing to the large resistances registered using the EIS measurements of the Inert_Aq and Inert_Cl (figure 4.18a). [101] Small lattice expansions in the c-direction and contractions in the a-direction are the largest structure changes for layered $LiMO_2$ materials being charged to 4.2 V. [102] Wang and co-workers [102] explains it as follows, using $LiNiO_2$ as an example: As Li is removed from the cathode, the oxidation state of Ni increases. This causes a decrease in the ionic radii and will shrink the edge-sharing $NiO_6$ layers along the a-axis. The layers will simultaneously become more positively charged and expel each other along the c-axis. Although all reports classify these lattice structure changes as reversible [41, 45, 102], such changes in the local structures during cycling, as well as changes in the particle morphology, have been reported to indirectly affect the reversibility by introducing higher resistance during charging. [101]

### 5.1.4 Cell resistance

The resistance measured by EIS for a charged coin cell using Inert_Aq and Inert_Cl active powders are shown in figure 4.18a. Sabet and Sauer reported in 2019 [94] that the low frequencies in the impedance spectra are assigned to the cathodes charge transfer resistance. From figure 4.18a, the charge transfer in Inert_Aq (410.3 Ω) is slower than in Inert_Cl (333.4 Ω). The cation mixing slows down the charge transfer and Li diffusion. These values may therefore be recognized in the higher degree of cation mixing and the lower capacity retention of Inert_Aq (70 %) compared to that of Inert_Cl (76 %). The Inert_Aq shows a higher resistance overall, but the slopes of their Warburg elements are approximately equal; this represents the diffusion coefficients of Inert_Aq and Inert_Cl. This eludes to similar characteristics of the diffusion layers of the electrode surfaces.

In addition, the Inert_Aq active material also shows higher overpotentials during the galvanostatic cycling (figure 4.15a). The battery resistance is likely to cause these dominant overpotentials. Due to charging the Inert_Aq battery when it has a high resistance, a higher potential is needed to extract $Li^+$ out of the cathode structure to provide the current output set for the galvanostatic cycling. This is seen as an increasing charging plateau for Inert_Aq called an overpotential as seen in figure 5.1. The discharge follows the same trend, only with discharge plateaus. The correlation between Inert_Aq's large resistance (figure 4.18a) and high overpotentials (figure 4.15a) provide strong evidence that the charge transfer kinetics are a more probable cause for the low electrochemical performances than the previous mentioned lattice instabilities.

The resistance does not only affect the capacity retention and overpotentials, but it also affects the reversibility of the redox reaction. The resistance is not continuously measured throughout the battery cycling, however, predictions of how the resistance develops during cycling can be made from the dQ/dV-plots (figure 4.16) and the corresponding galvanostatic data (figure 4.15). A rapidly decreasing capacity and a more irreversible reaction indicates that the resistance increases in both Inert_Aq and Inert_Cl with the cycling number. However, redox reactions are clearly more reversible for Inert_Cl. The reveribility of redox reactions account for better stability, which is also recognized in the higher capacity retention of Inert_Cl.
From the dQ/dV-plots in figure 4.16 both Inert_Aq and Inert_Cl have their main peak in the voltage-range expected for Ni- and Co-redox activity. This complies with the theory from figure 2.15 (3.5 - 4.0 V). Thus, the main current measured must arise from these redox species. [84] A certain amount of the reversible capacity will also be obtained from the oxygen reactions due to the high (4.3 V) and low (2.5) cutoff voltages during charge and discharge, respectively.

## 5.2 Co-precipitation reactions in air atmosphere

As described in the results section, the cation mixing and particle sizes vary with the presence of Cl. Three phenomena gave variations in the phase purity of the active powders. These being the presence of air during the co-precipitation, the pressure conditions during the Li-reaction, and the duration of the heat-treatment. Here, the electrochemical activity of the powders will be related to these variations and compared to other literature.

### 5.2.1 Morphology and particle size

It is clear that the powders synthesized in air (figure 4.9) have more distinct spherical shapes relative to the powders from traditional inert synthesis routes (figure 4.8). This exact sphericity and angularity of powders from air-synthesis using Cl (Air_Cl, Air_Cl_HighPLi and Air_Cl_5h) are recognized in other literature as single-crystal NMC particles [75], and are shown in figure 2.11. This suggests that the presence of Cl in the solution before nucleation promote the formation of more spherical single crystals. The crystal size of the Inert_Cl (413.3 nm) found in table 4.1, is in accordance with the particle size estimated in SEM (400 nm). This also indicates the formation of single-crystals. For Inert_Aq, the

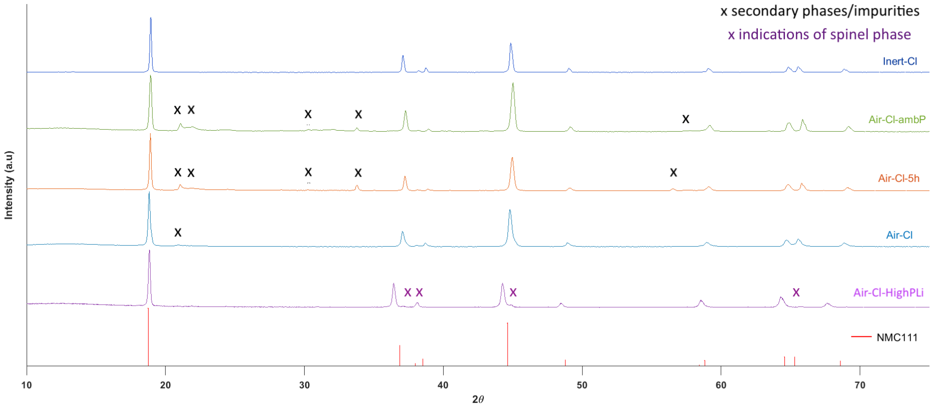

**Figure 5.2:** A comparison of the XRD patters for all active powders synthesized in the presence of Cl. No phase pure NMC111 is obtained for air-synthesized samples. The cross (x) show the secondary phases and impurities that deviate from a pure phased NMC111. Purple coloured (X) indicate the characteristic peaks of an spinel phased material in Air_Cl_HighPLi.

crystal size from XRD measurements are around 100 nm, whereas the APS are estimated to be twice the size (200 nm). This is not necessarily explained as polycrystalline materials as the XRD detect an average size and might have measured larger amounts of small particles which is easily overlooked in the SEM estimations of APS.

As mentioned, some of the active powders synthesized in air are clearly mono-crystalline. The formation of the preferred single crystals may contribute to the somewhat high capacity retention of the impure powders. It is commonly agreed that single crystals enhance the battery performance although disagreements arise when explaining why. Cho and coworkers [74] proposed that single crystal materials cycle better due to higher surface areas. This is however not the case here, as the Inert_Cl with larger crystals and lower surface areas show better performance. Reports from Li and co workers [59] and Swallow *et. al.* [58] explain the superior capacity retention of single crystal cells as a result of better material integrity. They argue that it is easier to generate microcracks in a poly-crystalline material during cycling due to the volume expansion and contraction of the crystal grains within the particle. Thus, a more stable interface is preserved in single crystal materials due to the suppression of microcracking. [59] An additional downside to microcracking is that it can isolate particles from the conducting material (carbon black). This will induce inactive areas in the cathode structure, which can explain the high irreversible capacity losses seen for the less single crystalline materials (Air_Cl_ambP in figure 4.9d). [58] The dominating mechanism can be revealed by cycling at low C-rates to rule out the kinetic limitations and to see how the polarization and capacity change.

Microcracking caused by phase transitions are not present in pure NMC111 as cycling is kept below 4.4 V. However, the secondary phases detected in the air-synthesized powders might induce phase transitions at lower voltages. This would especially be the case for the spinel-phased Air_Cl_HighPLi below 3 V. Phase transitions cause volume expansions and microcracking, which induce formation of new CEI. This will consume Li, form thicker CEI layers, or insulate parts of the active material. All these are interconnected, and will lead to an increased resistance, longer diffusion paths and decrease the rate of Li diffusion. These phenomena can explain the decreasing capacity and overpotentials for impure NMC materials seen in figure 4.14. The secondary phases will also show other properties than the main phase. These phases may be less conducting. The secondary phases are included in the weight calculation of the active material. These do not contribute to an increased capacity, and will therefore decrease the specific capacity.

The extremely low and unsteady coulombic efficiency of Air_Cl_5h in figure 4.14 is a result of major side reactions that occur during cycling. Such deviating values are often explained by the formation of mechanical stress. Stress is related to volume expansions when extracting and inserting Li. However, mechanical damage is reported to be considerably small for NMC111 compared to other compounds. [61] As samples without aggregates does not show these variations, the aggregates seen in SEM figure 4.9 for Air_Cl_5h might amplify the stress and may be more prone to fractures. Tsai and coworkers [103] reported that visible microcracks initiate close to the center of particles and propagate outward, beginning at a cycling voltage of 4.1 V. Microcracking will result in new contact areas with the electrolyte, additional CEI formation and more side-reactions. Hence, the energy input during the charging of the battery will not meet the energy output during discharge. This might be the explanation for the low colombic efficiency for the highly aggregated Air_Cl_5h found in figure 4.14. Further, the conductive pathways will break down or lead to a total disintegration of the electrode. This will have a detrimental effect on the internal resistance and eventually the capacity. [61, 104]

### 5.2.2 The effect of secondary phases

Impurity peaks are found between 20-30 2 $\theta$ for all air-synthesized samples. Thus, it is difficult to obtain a pure phase NMC111 during a co-precipitation in air. When comparing Inert_Cl and Air_Cl, the morphology, APS and PSD are approximately equal. Still, their electrochemical performance deviate. From these observations, the secondary phases seem to strongly decrease the electrochemical cycling. This is also clear in figure 5.3, which shows the phases and initial capacity for all air-synthesized samples. The sample of least secondary phases from air-synthesis (Air_Cl) obtains the highest initial discharge capacity (86 mAh/g) (also seen in results figure 4.11). This is unanimous with other research stating that the amount of secondary phases increases as the initial discharge capacity decreases. [105] The capacity of air-synthesized powders are shown in figure 5.3 are, however, extremely low relative to the expected values of an NMC111 (160 mAh/g). [14]

The impurity peaks of the XRD patterns in figure 5.2 are mainly found to be secondary phases of Mn. This is in agreement with reference [89] stating that Mn may react with the air and form Mn-based secondary phases. It is reported that during hydroxide formation, $MnO_2$ and MnOOH phases will form. The following heat-treatment will transform

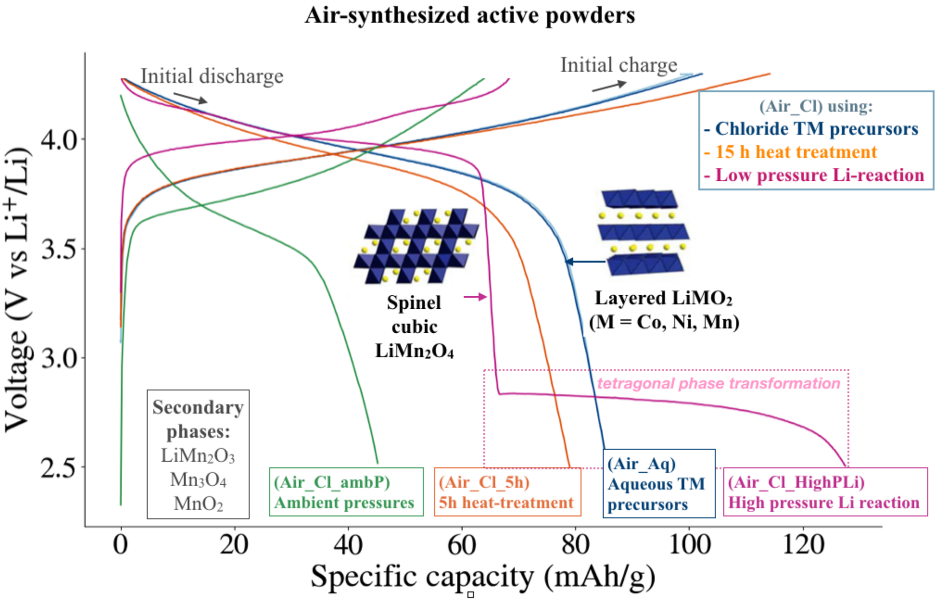

**Figure 5.3:** The initial galvanostatic cycle (at 0.1C) for all coin cells made with air-synthesized active powders, with emphasis on the phases detected. The conditions for the synthesis of Air_Cl is used as a reference. Changes in the variables listed under the reference can be seen by the curves of their respective colour. Illustrations of the spinel and layered crystal structure are placed on the powders of highest purity. The secondary phases detected for each of the air-synthesized powders are shown. The directions of charge and discharge are placed on the curves. The sample with least and most secondary phases (Air_Cl_ambP) have the highest and lowest initial capacity, respectively.

the Mn-residuals to the secondary phases recognized in the XRD diffractograms for all air-synthesized powders (figure 4.2 and figure 4.5). [89] The results are consistent with other research, concluding that a hydroxide co-precipitation synthesis of NMC111 should be performed in an inert atmosphere. [106]

A comparison between the XRD patterns of powders with the longest exposure to air (Air_Cl_ambP, figure 4.2) and in an inert atmosphere (Inert_Cl, figure 4.7) provide clear knowledge of how oxygen influence the synthesis. Earlier research [107] explains how the rate of Mn-oxidation in water changes depending on the pH, the amount of Mn and the concentration of oxygen dissolved in the solution. A higher concentration of oxygen was reported to increase the Mn oxidation. [107] Active powders made with an autoclave-step (Air_Cl and Air_Cl_HighPLi) has less secondary phases than the one excluding this step (Air_Cl_ambP). Due to the extremely large amount of secondary phases for Air_Cl_ambP shown in figure 4.2 it is evident that the formation of secondary phases also occurs after the co-precipitation reaction. For the samples here, the pH and the concentration of Mn is constant for all synthesis making the amount of oxygen in solution the only variable. Longer reaction times in the presence of air seem to cause more Mn to react with oxygen.

The hydrothermal conditions may reduce the amount of oxygen in the solution and constricts the oxidation of Mn. [89, 107]

Not only do the air-synthesized powders show a poor initial performance, but they also have an irreversible capacity loss throughout the galvanostatic cycling. A probable cause for this loss are the secondary phases detected in the XRD patterns. This induces multiple oxidation states for the TMs, and the presence of unwanted states such as $Mn^{2+}$ are more likely to appear. This state is dissolvable in the electrolyte during cycling, and results in an irreversible loss of Mn. This dissolving species is one of main drawbacks for LMNO and LMO cathodes. [89] One of the secondary phases in Air_Cl_ambP (figure 4.3) match a Li-rich tetragonal spinel phase ($Li_2MnO_3$). Such phase is reported to transform at high delitihation (charge) from $Li_2MnO_3$ to $Li_2O$. Subsequently, an irreversible capacity loss will follow. This transformation is, however, unlikely to cause the irreversible losses seen during cycling as these occur above 4.4 V; here the charging only reaches 4.3 V. [89]

However, the capacity retention of Air_Cl from figure 4.14 is still the highest among all samples (82 %). The low cutoff voltage can explain the relatively high reversible capacity of Air_Cl_HighPLi (68 %) and Air_Cl (82 %). When discharging Mn layered oxides below 3.0 V, the oxygen molecules are reported to be electrochemically reduced leading to extra capacity. Oxygen containing species accumulate on the electrode surface. Upon the second charge above 4.0 V, these residuals are electrochemically decomposed causing a higher capacity. [49] This way, the impurities of Mn oxides in powders made from air-synthesis can actually contribute to a higher reversible capacity; this is seen as a high capacity retention.

Wang [91] reported that impurity phases, such as the $Mn_3O_4$ phase detected in Air_Cl_ambP, disappeared at relatively high temperatures of 750 °C. A phase pure $LiMn_2O_4$ spinel phase was also obtained after the heat-treatment. This is however not consistent with the results found here, as most impurity phases are still present after longer heat-treatments at higher temperatures (15 h heat treatment in 850 °C).

As seen from the XRD pattern of Air_Cl and Air_Aq (figure 4.5), the powders transform to an intermediate spinel phase during the 480 °C heat treatment. After a heat-treatment at 850 °C, these turn into a main phased layered NMC. This is as expected, as a spinel phase and layered phase are favourable at $\sim$ 400 °C and 800 °C, respectively. [89] He, Sun and Yu [68] found the intermediate spinel phase to be an $(Ni_{1/3}Co_{1/3}Mn_{1/3})O_4$ phase, which are favorable at $\sim$ 500 °C. At higher temperatures (900 °C in 12 h) the formation of layered NMC111 was formed. This is consistent with the results obtained here. Although, the intermediate phase here was heat-treated for a longer time at lower temperatures (850 °C at 15 h). An impurity phase is still detected at around 21 $\theta$ for the Air_Cl in figure 4.5. Impurities may therefore disappear at higher temperatures (900 °C).

Wang *et. al.* mentioned that the highly aggregated particles may be caused by the presence of the $Mn_2O_3$ impurity phase. [91] Thus, the impurities detected in the XRD patterns for the Air_Cl_5h in figure 4.6 may promote the formation of aggregates found in the SEM images in figure 4.9b. Another contributing factor for the formation of such aggregates are the 10 h shorter heat-treatment.

### 5.2.3 The effect of heat-treatment

Active powders synthesized using Cl precursors in combination with a 15 h heat-treatment, (Air_Cl_HighPLi, Air_Cl, Air_Cl_ambP and Inert_Cl) has no visible differences in PSD or APS (table 4.2). Neither the autoclave nor an inert atmosphere show any influence on the APS. Experimental observations of the APS from the long (Air_Cl, 400 nm) and short (Air_Cl_5h, 200 nm) heat treated powders are consistent with other research; shorter heat-treatments generally result in smaller particle sizes. [3, 108]

Another trend worth mentioning, is related to the effect a 850 °C heat-treatment has on the surface area and the particle size. As the APS in table 4.2 are estimated through SEM, it is expedient to use the BET surface areas from table 4.3 as supporting data. It is known that a low surface area gives a large particle size and vice versa. [109] When comparing the particle sizes from table 4.2, with the surface areas from table 4.3, the results comply with the trend above.

Porous structures are known to obtain extreme high BET surface areas. The highly porous particles for Air_Aq before the 850 °C heat-treatment complies with the measured BET surface area of 23.88 $m^2/g$. From the SEM images in figure 4.10, it is clear that the heat-treatment at 850 °C induce a growth in APS. The highly porous non-spherical particles are reduced to sub-round spherical particles with a lower porosity. This is recognized in the decreasing BET surface area (2.57 $m^2/g$).

An exception is seen for the powder synthesized with a 5 h heat-treatment (Air_Cl_5h). The surface area is 0.64 $m^2/g$ and the APS is approximately 200 nm. This surface area is extremely low relative to the other powders, and may be explained by the aggregates seen in figure 4.9b. It is important to keep in mind that the BET theory takes into account the adsorption of $N_2$ on the particle surface. These aggregations decrease the total calculated surface area due to the compact particles that will not let $N_2$ adsorb. In fact, these aggregates may also be the explanation for the low electrochemical performance of Air_Cl_5h seen in 4.14 and 4.12. According to Lu *et. al.* [90], aggregations make it more difficult to break up during the preparation of the electrode. This is seen experimentally as a small total surface area of 0.64 $m^2/g$. Hence, less of the active material's surface area is in contact with the electrolyte. This is causing the extremely low coulombic efficiency seen in figure 4.14 for Air_Cl_5h.

### 5.2.4 The Li-reaction step

By comparing the sample without a Li-reaction in high pressure (Air_Cl) to that using high pressure (Air_Cl_HighPLi), it is clear that the latter had non-sufficient conditions for the Li reaction. A high pressure is not sufficient for the Li reaction to fully occur. This is found by comparing the sample using a traditional Li-reaction during calcination (Air_Cl), to that using high pressures (Air_Cl_HighPLi).

The XRD pattern (figure 4.1) and the cycling data (figure 4.13a) agrees that a Air_Cl_HighPLi obtained a spinel phased material. However, two rather unexpected features is seen in the spinel shaped charge/discharge curve of Air_Cl_HighPLi in figure 4.13a. Firstly, the edge seen at 3.7 V during charge seems to disappear during multiple cycles. Secondly, the shape of the first charging cycle has similar features to those of layered cathode materials. Comparing with figure 2.6, these are not related to the LMO and LMNO spinel structures and might arise from the presence of Co. [93]

Chen and co-workers [110] suggest that lower temperatures increased the cation mixing in $LiFeO_4$. They report that the mixing approaches 8 % at 120 °C, and essentially drops to zero above 175 °C. Thus, a low temperature (120 °C) may impact the structure, and is a probable cause for the incomplete reaction of Li under high pressures. However, powders synthesized at temperatures of 160 °C and 175 °C (figure B.1 also accommodates a spinel phase. Thus, stochiometric errors are conceivably the reason for these undesirable outcomes.

# Chapter 6

# Conclusion

Co-precipitation synthesis' of active NMC111 powders were tested in air and in inert atmospheres. A hydrothermal step was included in the air-synthesis to examine the ability of Li to react at high pressures. It resulted in an inadequate reaction and the formation of unwanted phases. Consequently, multiple conditions were tested to obtain layered structures of NMC. The presence of Cl during co-precipitation was investigated by doing parallel synthesis with standard pure Aq nitrate- and acetate solutions.

Powder synthesis performed in the air failed to obtain a phase pure NMC111. Unwanted secondary phases were formed during the co-precipitation step due to the oxidation of Mn. The formation increased with the concentration of oxygen in solution. Li showed poor abilities to react with the precipitate at high pressures in 120 °C seen as a formation of a spinel phase (58.8 %). This showed low cycling performance of $\sim$ 80 mAh/g. The 5 h heat treatment formed aggregates with smaller surface areas, and impure phases. This furnished unstable structures and scanted the electrolyte-contact area, which promoted microcracking and the creation of new interphases. This consumed Li and was concluded to be the cause of the large variations in coulombic efficiency between cycles. Inert atmospheres were concluded to be of significance for forming a pure phase NMC111 material with high electrochemical performance.

XRD, Rietveld analysis, and BET surface area measurements of the powder revealed that the crystal size and the particle size increased in the presence of Cl and with longer heat treatments. The degree of cation mixing decreased; probably caused by a more meticulous washing and sieving. This would remove contamination and enhance structure formation. Consequently, synthesis using Cl-precursors achieved a higher initial discharge capacity and capacity retention (143 mAh/g and 76 % after 80 cycles, respectively) opposed to the standard Aq-based precursors (133 mAh/g and 70 % after 80 cycles, respectively). With thorough washing of powder during synthesis, Cl precursors were qualified as starting materials for cathode synthesis, and the tested Glencore's $NiCl_2$ and $CoCl_2$ solutions was concluded as promising for the use in LIBs.

# Chapter 7

# Further Work

In commercialized batteries with a graphite anode, the amount of Li may be limited. All batteries in this report are cycled using Li metal as an anode. Such half-cells have an unlimited amount of Li and the effect of side reactions consuming Li will not be accounted for in the same degree as for commercialized batteries. In this aspect, a three-electrode cell set-up with Li as a reference would provide more accurate information about the mechanisms leading to failure.

The XRD measurements and SEM was taken immediately after heat-treatment, but the NMC111 powder was stored in air for a time before cell assembly. Secondary phases of Li residuals may have formed in between the two analysis and contribute to somewhat low capacity. [111] More reliable results can be obtained by storing the NMC111 powders in an inert atmosphere. Future work should include investigation of phase changes of stored samples through XRD analysis and SEM. A comparison between the before and after storing could reveal interesting results regarding degradation during storage.

As concluded by Toby in 2006 [112], the quality of a Rietveld fitting is best determined by viewing the observed and calculated patterns graphically. The difference plots can, therefore, be considered as a quality reference. It must also be kept in mind that minimizing the difference uncontrollably does not necessarily provide more reliable results. The reliability (Rwp %) of Rietveld refinements are regarded as high values if above 10 %. As table 4.1 shows, the sample Air_Cl_HighPLi has a noticeable higher Rwp (13.96 %) than the other. This should be taken into account when considering the credibility of a 58 % spinel phase in the powder. This compound, and formation of its spinel phase, should therefore be further investigated.

Further work will include the investigation of the reaction mechanism with Li in the hydrothermal step for synthesis in air. Apparently, some Li react, but not to completion. To understand whether this spinel phase is favorable due to incomplete Li reaction, or low-temperature conditions are highly crucial for understanding the reaction mechanism under these conditions. Further, testing how the powder morphology is formed during high pressure conditions is an interesting point of view. This could be done by examining the powder with XRD and SEM before and after it was introduced to the autoclave. It was however outside the scope of this work, as the aim was to obtain a pure NMC111 phase.

# Bibliography

[1] Prof. Dr. Bruno Burger. Fraunhofer institute for solar energy systems ise, 08.05.2018. URL `https://www.ise.fraunhofer.de/`. Assessed: 2019-03-20.

[2] J. Chen and X. Song. Economics of energy storage technology in active distribution networks. *Journal of Modern Power Systems and Clean Energy*, 3(4):583–588, 2015. doi: 10.1007/s40565-015-0148-5.

[3] Cuixia Cheng, Long Tan, Haowen Liu, and Xintang Huang. High rate performances of the cathode material lini1/3co1/3mn1/3o2 synthesized using low temperature hydroxide precipitation. *Materials Research Bulletin*, 46(11):2032 – 2035, 2011. ISSN 0025-5408. doi: https://doi.org/10.1016/j.materresbull.2011.07.004.

[4] Abdeen Mustafa Omer. Energy, environment and sustainable development. *Renewable and Sustainable Energy Reviews*, 12(9):2265–2300, 2008. ISSN 1364-0321. doi: https://doi.org/10.1016/j.rser.2007.05.001.

[5] Bruno Scrosati and Jrgen Garche. Lithium batteries: Status, prospects and future. *Journal of Power Sources*, 195(9):2419–2430, 2010. ISSN 0378-7753. doi: https://doi.org/10.1016/j.jpowsour.2009.11.048.

[6] Vinodkumar Etacheri, Rotem Marom, Ran Elazari, Gregory Salitra, and Doron Aurbach. Challenges in the development of advanced li-ion batteries: a review. *Energy & Environmental Science*, 4(9):3243–3262, 2011. ISSN 1754-5692. doi: 10.1039/C1EE01598B.

[7] World Wildlife Fund. *Getting strategies at the municipal solid waste source*. Island Press, Covelo California, Washington, 1991.

[8] M. S. Whittingham. Electrical energy storage and intercalation chemistry. *Science*, 192(4244):1126–1127, 1976. Export Date: 18 April 2016.

[9] Naoki Nitta, Feixiang Wu, Jung Tae Lee, and Gleb Yushin. Li-ion battery materials: present and future. *Materials Today*, 18(5):252–264, 2015. ISSN 1369-7021. doi: https://doi.org/10.1016/j.mattod.2014.10.040.

[10] K. Nagaura, T.;Tozawa. Progress in batteries and solar cells. *The Journal of the European Ceramic Society*, 9:209, 1990.

[11] Tsutomu Ohzuku, Atsushi Ueda, and Masatoshi Nagayama. Electrochemistry and structural chemistry of linio2 (r3m) for 4 volt secondary lithium cells. *Journal of The Electrochemical Society*, 140(7):1862–1870, 1993. doi: 10.1149/1.2220730.

[12] M. S. Whittingham. Lithium batteries and cathode materials. *Chemical Reviews*, 104(10):4271–4301, 2004. doi: 10.1021/cr020731c. Cited By :2946 Export Date: 27 September 2017.

[13] Tsutomu Ohzuku and Yoshinari Makimura. Layered lithium insertion material of lico1/3ni1/3mn1/3o2 for lithium-ion batteries. *Chemistry Letters*, 30(7):642–643, 2001. doi: 10.1246/cl.2001.642.

[14] J. Liu P. Nelson G. Henriksen, K. Amine. 204th meeting of the electrochemical society. *The Electrochemical Society*, Abstract 255, 2003.

[15] Do-Wook Jun, Chong S. Yoon, Un-Hyuck Kim, and Yang-Kook Sun. High-energy density coreshell structured li[ni0.95co0.025mn0.025]o2 cathode for lithium-ion batteries. *Chemistry of Materials*, 29(12):5048–5052, 2017. doi: 10.1021/acs.chemmater.7b01425.

[16] Helmut Schfer, Barbara Milow, and Lorenz Ratke. Synthesis of inorganic aerogels via rapid gelation using chloride precursors. *RSC Adv.*, 3:15263–15272, 2013. doi: 10.1039/C3RA41688G.

[17] Outotec Oyj. Technologies for producing battery raw materials, 2018. URL `https://www.outotec.com/landing-pages/battery-metals/technologies-for-producing-battery-raw-materials/`. Assessed: 2019-05-14.

[18] Yoshio Nishi. Lithium ion secondary batteries; past 10 years and the future. *Journal of Power Sources*, 100(1):101–106, 2001. ISSN 0378-7753. doi: https://doi.org/10.1016/S0378-7753(01)00887-4.

[19] Bo Xu, Danna Qian, Ziying Wang, and Ying Shirley Meng. Recent progress in cathode materials research for advanced lithium ion batteries. *Materials Science and Engineering: R: Reports*, 73(5):51 – 65, 2012. ISSN 0927-796X. doi: https://doi.org/10.1016/j.mser.2012.05.003.

[20] John B. Goodenough and Kyu-Sung Park. The li-ion rechargeable battery: A perspective. *Journal of the American Chemical Society*, 135(4):1167–1176, 2013. ISSN 0002-7863. doi: 10.1021/ja3091438.

[21] Wolf Vielstich Carl H Hamann, Andrew Hamnett. *Electrochemistry*. Second, Completely Revised and Updated Edition. WILEY-VCH, Weinheim, 2007.

[22] Chaofeng Liu, Zachary G. Neale, and Guozhong Cao. Understanding electrochemical potentials of cathode materials in rechargeable batteries. *Materials Today*, 19 (2):109–123, 2016. ISSN 1369-7021. doi: https://doi.org/10.1016/j.mattod.2015.10.009.

[23] H. Wenzl. Batteries and fuel cells — lifetime. In Jrgen Garche, editor, *Encyclopedia of Electrochemical Power Sources*, pages 552 – 558. Elsevier, Amsterdam, 2009. ISBN 978-0-444-52745-5. doi: https://doi.org/10.1016/B978-044452745-5.00048-4.

[24] A. J. Smith, J. C. Burns, S. Trussler, and J. R. Dahn. Precision measurements of the coulombic efficiency of lithium-ion batteries and of electrode materials for lithium-ion batteries. *Journal of The Electrochemical Society*, 157(2):A196–A202, 2010. doi: 10.1149/1.3268129.

[25] Karim Zaghib, Joel Dub, Aime Dallaire, Karen Galoustov, Abdelbast Guerfi, Mayandi Ramanathan, Aadil Benmayza, Jai Prakash, Alain Mauger, and Christian M. Julien. 19 - lithium-ion cell components and their effect on high-power battery safety. In Gianfranco Pistoia, editor, *Lithium-Ion Batteries*, pages 437 – 460. Elsevier, Amsterdam, 2014. ISBN 978-0-444-59513-3. doi: https://doi.org/10.1016/B978-0-444-59513-3.00019-4.

[26] Kang Xu. Nonaqueous liquid electrolytes for lithium-based rechargeable batteries. *Chemical Reviews*, 104(10):4303–4418, 2004. ISSN 0009-2665. doi: 10.1021/cr030203g.

[27] John B. Goodenough and Youngsik Kim. Challenges for rechargeable li batteries. *Chemistry of Materials*, 22(3):587–603, 2010. ISSN 0897-4756. doi: 10.1021/cm901452z.

[28] C. G. Barlowz. Reaction of water with hexafluorophosphates and with li bis(perfluoroethylsulfonyl)imide salt. *Electrochemical and Solid-State Letters*, 2 (8):362–364, 1999. doi: 10.1149/1.1390838.

[29] Seong Jin An, Jianlin Li, Claus Daniel, Debasish Mohanty, Shrikant Nagpure, and David L. Wood. The state of understanding of the lithium-ion-battery graphite solid electrolyte interphase (sei) and its relationship to formation cycling. *Carbon*, 105(Supplement C):52–76, 2016. ISSN 0008-6223. doi: https://doi.org/10.1016/j.carbon.2016.04.008.

[30] Wei-Jun Zhang. Lithium insertion/extraction mechanism in alloy anodes for lithium-ion batteries. *Journal of Power Sources*, 196(3):877–885, 2011. ISSN 0378-7753. doi: https://doi.org/10.1016/j.jpowsour.2010.08.114.

[31] Martin Winter and Jrgen O. Besenhard. Electrochemical lithiation of tin and tin-based intermetallics and composites. *Electrochimica Acta*, 45(1):31–50, 1999. ISSN 0013-4686. doi: https://doi.org/10.1016/S0013-4686(99)00191-7.

[32] Wei-Jun Zhang. A review of the electrochemical performance of alloy anodes for lithium-ion batteries. *Journal of Power Sources*, 196(1):13–24, 2011. ISSN 0378-7753. doi: https://doi.org/10.1016/j.jpowsour.2010.07.020.

[33] Antonino Salvatore Aric, Peter Bruce, Bruno Scrosati, Jean-Marie Tarascon, and Walter van Schalkwijk. Nanostructured materials for advanced energy conversion and storage devices. *Nature Materials*, 4:366, 2005. doi: 10.1038/nmat1368.

[34] Kristin Persson, Vijay A. Sethuraman, Laurence J. Hardwick, Yoyo Hinuma, Ying Shirley Meng, Anton van der Ven, Venkat Srinivasan, Robert Kostecki, and Gerbrand Ceder. Lithium diffusion in graphitic carbon. *The Journal of Physical Chemistry Letters*, 1(8):1176–1180, 2010. doi: 10.1021/jz100188d.

[35] Wangda Li, Bohang Song, and Arumugam Manthiram. High-voltage positive electrode materials for lithium-ion batteries. *Chem. Soc. Rev.*, 46:3006–3059, 2017. doi: 10.1039/C6CS00875E.

[36] Patrick Rozier and Jean Marie Tarascon. Reviewli-rich layered oxide cathodes for next-generation li-ion batteries: Chances and challenges. *Journal of The Electrochemical Society*, 162(14):A2490–A2499, 2015. doi: 10.1149/2.0111514jes.

[37] M. M. Thackeray, W. I. F. David, P. G. Bruce, and J. B. Goodenough. Lithium insertion into manganese spinels. *Materials Research Bulletin*, 18(4):461–472, 1983. ISSN 0025-5408. doi: https://doi.org/10.1016/0025-5408(83)90138-1.

[38] Koichi Momma and Fujio Izumi. Vesta3 for three-dimensional visualization of crystal, volumetric and morphology data. *Journal of Applied Crystallography*, 44 (6):1272–1276, 2011. doi: 10.1107/S0021889811038970.

[39] A. Manthiram, A. Vadivel Murugan, A. Sarkar, and T. Muraliganth. Nanostructured electrode materials for electrochemical energy storage and conversion. *Energy Environ. Sci.*, 1:621–638, 2008. doi: 10.1039/B811802G.

[40] Wen Liu, Pilgun Oh, Xien Liu, Min-Joon Lee, Woongrae Cho, Sujong Chae, Youngsik Kim, and Jaephil Cho. Nickel-rich layered lithium transition-metal oxide for high-energy lithium-ion batteries. *Angewandte Chemie International Edition*, 54(15):4440–4457, 2015.

[41] S. C. Yin, Y. H. Rho, I. Swainson, and L. F. Nazar. X-ray/neutron diffraction and electrochemical studies of lithium de/re-intercalation in li1-xco1/3ni1/3mn1/3o2 (x = 0 1). *Chemistry of Materials*, 18(7):1901–1910, 2006. ISSN 0897-4756. doi: 10.1021/cm0511769.

[42] O. Dolotko, A. Senyshyn, M. J. Mhlbauer, K. Nikolowski, and H. Ehrenberg. Understanding structural changes in nmc li-ion cells by in situ neutron diffraction. *Journal of Power Sources*, 255:197–203, 2014. ISSN 0378-7753. doi: https://doi.org/10.1016/j.jpowsour.2014.01.010.

[43] J.R. Dahn, U. von Sacken, and C.A. Michal. Structure and electrochemistry of li1ynio2 and a new li2nio2 phase with the ni (oh)2 structure. *Solid State Ionics*, 44 (1):87 – 97, 1990. ISSN 0167-2738. doi: https://doi.org/10.1016/0167-2738(90) 90049-W.

[44] Hyung-Joo Noh, Sungjune Youn, Chong Seung Yoon, and Yang-Kook Sun. Comparison of the structural and electrochemical properties of layered li[nixcoymnz]o2 (x=1/3, 0.5, 0.6, 0.7, 0.8 and 0.85) cathode material for lithium-ion batteries. *Journal of Power Sources*, 233:121–130, 2013. ISSN 0378-7753. doi: https://doi.org/10.1016/j.jpowsour.2013.01.063.

[45] N. Yabuuchi and T. Ohzuku. Novel lithium insertion material of lico1/3ni1/3mn1/3o2 for advanced lithium-ion batteries. *Journal of Power Sources*, 119-121:171–174, 2003. doi: 10.1016/S0378-7753(03)00173-3. Export Date: 27 August 2018.

[46] K. M. Shaju, G. V. Subba Rao, and B. V. R. Chowdari. Performance of layered li(ni1/3co1/3mn1/3)o2 as cathode for li-ion batteries. *Electrochimica Acta*, 48(2): 145–151, 2002. ISSN 0013-4686. doi: https://doi.org/10.1016/S0013-4686(02)00593-5.

[47] Roland Jung, Michael Metzger, Filippo Maglia, Christoph Stinner, and Hubert A. Gasteiger. Oxygen release and its effect on the cycling stability of linixmnycozo2 (nmc) cathode materials for li-ion batteries. *Journal of The Electrochemical Society*, 164(7):A1361–A1377, 2017. doi: 10.1149/2.0021707jes.

[48] M. H. Lee, Y. J. Kang, S. T. Myung, and Y. K. Sun. Synthetic optimization of li[ni1/3co1/3mn1/3]o2 via co-precipitation. *Electrochimica Acta*, 50(4):939–948, 2004. ISSN 0013-4686. doi: https://doi.org/10.1016/j.electacta.2004.07.038.

[49] Naoaki Yabuuchi, Kazuhiro Yoshii, Seung-Taek Myung, Izumi Nakai, and Shinichi Komaba. Detailed studies of a high-capacity electrode material for rechargeable batteries, li2mno3lico1/3ni1/3mn1/3o2. *Journal of the American Chemical Society*, 133(12):4404–4419, 2011. doi: 10.1021/ja108588y. PMID: 21375288.

[50] D. Li, D.L. Danilov, H.J. Bergveld, R.-A. Eichel, and P.H.L. Notten. Chapter 9: Understanding battery aging mechanisms. *RSC Catalysis Series*, 2019-January(37): 220–250, 2019. doi: 10.1039/9781788016124-00220.

[51] J.A. Gilbert, I.A. Shkrob, and D.P. Abraham. Transition metal dissolution, ion migration, electrocatalytic reduction and capacity loss in lithium-ion full cells. *Journal of the Electrochemical Society*, 164(2):A389–A399, 2017. doi: 10.1149/2.1111702jes.

[52] J. Wandt, A. Freiberg, R. Thomas, Y. Gorlin, A. Siebel, R. Jung, H.A. Gasteiger, and M. Tromp. Transition metal dissolution and deposition in li-ion batteries investigated by operando x-ray absorption spectroscopy. *Journal of Materials Chemistry A*, 4(47):18300–18305, 2016. doi: 10.1039/C6TA08865A.

[53] H. Tsunekawa, S. Tanimoto, R. Marubayashi, M. Fujita, K. Kifune, and M. Sano. Capacity fading of graphite electrodes due to the deposition of manganese ions on them in li-ion batteries. *Journal of the Electrochemical Society*, 149(10):A1326–A1331, 2002. doi: 10.1149/1.1502686. cited By 87.

[54] Wengao Zhao, Jianming Zheng, Lianfeng Zou, Haiping Jia, Bin Liu, Hui Wang, Mark H. Engelhard, Chongmin Wang, Wu Xu, Yong Yang, and Ji-Guang Zhang. High voltage operation of ni-rich nmc cathodes enabled by stable electrode/electrolyte interphases. *Advanced Energy Materials*, 8(19):1800297, 2018. doi: 10.1002/aenm.201800297.

[55] G.A. Elia, U. Ulissi, F. Mueller, J. Reiter, N. Tsiouvaras, Y.-K. Sun, B. Scrosati, S. Passerini, and J. Hassoun. A long-life lithium ion battery with enhanced electrode/electrolyte interface by using an ionic liquid solution. *Chemistry - A European Journal*, 22(20):6808–6814, 2016. doi: 10.1002/chem.201505192. cited By 22.

[56] Y. Qian, P. Niehoff, M. Brner, M. Grtzke, X. Mnnighoff, P. Behrends, S. Nowak, M. Winter, and F.M. Schappacher. Influence of electrolyte additives on the cathode electrolyte interphase (cei) formation on lini 1/3 mn 1/3 co 1/3 o 2 in half cells with li metal counter electrode. *Journal of Power Sources*, 329:31–40, 2016. doi: 10.1016/j.jpowsour.2016.08.023. cited By 38.

[57] D. Sun, Q. Wang, J. Zhou, Y. Lyu, Y. Liu, and B. Guoz. Forming a stable cei layer on lini0.5mn1.5o4 cathode by the synergy effect of fec and hdi. *Journal of the Electrochemical Society*, 165(10):A2032–A2036, 2018. doi: 10.1149/2.0211810jes.

[58] Jessica G. Swallow, William H. Woodford, Frank P. McGrogan, Nicola Ferralis, Yet-Ming Chiang, and Krystyn J. Van Vliet. Effect of electrochemical charging on elastoplastic properties and fracture toughness of lixcoo2. *Journal of The Electrochemical Society*, 161(11):F3084–F3090, 2014. doi: 10.1149/2.0141411jes.

[59] Hongyang Li, Jing Li, Xiaowei Ma, and J. R. Dahn. Synthesis of single crystal lini0.6mn0.2co0.2o2 with enhanced electrochemical performance for lithium ion batteries. *Journal of The Electrochemical Society*, 165(5):A1038–A1045, 2018. doi: 10.1149/2.0951805jes.

[60] Xiaoyu Zhang, W. J. Jiang, A. Mauger, Qilu, F. Gendron, and C. M. Julien. Minimization of the cation mixing in li1+x(nmc)1xo2 as cathode material. *Journal of Power Sources*, 195(5):1292–1301, 2010. ISSN 0378-7753. doi: https://doi.org/10.1016/j.jpowsour.2009.09.029.

[61] W. H. Woodford, Y. M. Chiang, and W. C. Carter. Electrochemical shock of intercalation electrodes: A fracture mechanics analysis. *Journal of the Electrochemical Society*, 157(10):A1052–A1059, 2010. doi: 10.1149/1.3464773. Cited By :164 Export Date: 14 September 2018.

[62] K. Edstrm, T. Gustafsson, and J.O. Thomas. The cathodeelectrolyte interface in the li-ion battery. *Electrochimica Acta*, 50(2):397 – 403, 2004. ISSN 0013-4686. doi: https://doi.org/10.1016/j.electacta.2004.03.049. Polymer Batteries and Fuel Cells:Selection of Papers from First International Conference.

[63] S. Jouanneau, K. W. Eberman, L. J. Krause, and J. R. Dahn. Synthesis, characterization, and electrochemical behavior of improved li[nixco1-2xmnx]o2 (0.1  x 0.5). *Journal of the Electrochemical Society*, 150(12):A1637–A1642, 2003. doi: 10.1149/1.1622956. Cited By :105 Export Date: 14 September 2018.

[64] T. Nukuda, T. Inamasu, A. Fujii, D. Endo, H. Nakagawa, S. Kozono, T. Iguchi, J. Kuratomi, K. Kohno, S. Izuchi, and M. Oshitani. Development of a lithium ion battery using a new cathode material. *Journal of Power Sources*, 146(1):611–616, 2005. ISSN 0378-7753. doi: https://doi.org/10.1016/j.jpowsour.2005.03.074.

[65] Feng Wu, Meng Wang, Yuefeng Su, Liying Bao, and Shi Chen. A novel method for synthesis of layered lini1/3mn1/3co1/3o2 as cathode material for lithium-ion battery. *Journal of Power Sources*, 195(8):2362–2367, 2010. ISSN 0378-7753. doi: http://dx.doi.org/10.1016/j.jpowsour.2009.10.043.

[66] Xufang Luo, Xianyou Wang, Li Liao, Sergio Gamboa, and P. J. Sebastian. Synthesis and characterization of high tap-density layered li[ni1/3co1/3mn1/3]o2 cathode material via hydroxide co-precipitation. *Journal of Power Sources*, 158(1):654–658, 2006. ISSN 0378-7753. doi: https://doi.org/10.1016/j.jpowsour.2005.09.047.

[67] Chuan-yue Hu, Jun Guo, Yong Du, Hong-hui Xu, and Yue-hui He. Effects of synthesis conditions on layered li[ni1/3co1/3mn1/3]o2 positive-electrode via hydroxide co-precipitation method for lithium-ion batteries. *Transactions of Nonferrous Metals Society of China*, 21(1):114–120, 2011. ISSN 1003-6326. doi: https://doi.org/10.1016/S1003-6326(11)60686-9.

[68] Li-Po He, Shu-Ying Sun, and Jian-Guo Yu. Performance of lini1/3co1/3mn1/3o2 prepared from spent lithium-ion batteries by a carbonate co-precipitation method. *Ceramics International*, 44(1):351 – 357, 2018. ISSN 0272-8842. doi: https://doi.org/10.1016/j.ceramint.2017.09.180.

[69] Sbastien Patoux and Marca M. Doeff. Direct synthesis of lini1/3co1/3mn1/3o2 from nitrate precursors. *Electrochemistry Communications*, 6(8):767–772, 2004. ISSN 1388-2481. doi: https://doi.org/10.1016/j.elecom.2004.05.024.

[70] Shunyi Yang, Xianyou Wang, Quanqi Chen, Xiukang Yang, Jiaojiao Li, and Qiliang Wei. Effects of complexants on [ni1/3co1/3mn1/3]co3 morphology and electrochemical performance of lini1/3co1/3mn1/3o2. *Journal of Solid State Electrochemistry*, 16(2):481–490, 2012. ISSN 1433-0768. doi: 10.1007/s10008-011-1356-1.

[71] Ambrose R. Nichols and James H. Walton. The autoxidation of manganous hydroxide. *Journal of the American Chemical Society*, 64(8):1866–1870, 1942. ISSN 0002-7863. doi: 10.1021/ja01260a034.

[72] Thien An Vu, Mary M. Reagan, Dongsheng Li, Benjamin Legg, James J. De Yoreo, Jillian F. Banfield, and Hengzhong Zhang. Kinetics of crystal growth of nanogoethite in aqueous solutions containing nitrate and sulfate anions. *CrystEngComm*, 16:1466–1471, 2014. doi: 10.1039/C3CE41685B.

[73] Ian Sims and Bev Brown. 16 - concrete aggregates. In Peter C. Hewlett, editor, *Lea's Chemistry of Cement and Concrete (Fourth Edition)*, pages 907 – 1015. Butterworth-Heinemann, Oxford, fourth edition edition, 1998. ISBN 978-0-7506-6256-7. doi: https://doi.org/10.1016/B978-075066256-7/50028-X.

[74] Dae-Hyun Cho, Chang-Heum Jo, Woosuk Cho, Young-Jun Kim, Hitoshi Yashiro, Yang-Kook Sun, and Seung-Taek Myung. Effect of residual lithium compounds on layer ni-rich li[ni0.7mn0.3]o2. *Journal of The Electrochemical Society*, 161(6): A920–A926, 2014. doi: 10.1149/2.042406jes.

[75] Juan C. Garcia, Javier Bareo, Jianhua Yan, Guoying Chen, Andrew Hauser, Jason R. Croy, and Hakim Iddir. Surface structure, morphology, and stability of li(ni1/3mn1/3co1/3)o2 cathode material. *The Journal of Physical Chemistry C*, 121 (15):8290–8299, 2017. doi: 10.1021/acs.jpcc.7b00896.

[76] Yoshio Waseda, Eiichiro Matsubara, and Kozo Shinoda. *Fundamental Properties of X-rays*, pages 1–20. Springer Berlin Heidelberg, Berlin, Heidelberg, 2011. ISBN 978-3-642-16635-8. doi: 10.1007/978-3-642-16635-8_1.

[77] Anton Paar. X-ray-diffraction (xrd). *Anton Paar*, 2019. Assessed: 2019-05-11.

[78] Yoshio Waseda, Eiichiro Matsubara, and Kozo Shinoda. *Scattering and Diffraction*, pages 67–106. Springer Berlin Heidelberg, Berlin, Heidelberg, 2011. ISBN 978-3-642-16635-8. doi: 10.1007/978-3-642-16635-8_3.

[79] Elahe Talaie, Patrick Bonnick, Xiaoqi Sun, Quan Pang, Xiao Liang, and Linda F. Nazar. Methods and protocols for electrochemical energy storage materials research. *Chemistry of Materials*, 29(1):90–105, 2017. ISSN 0897-4756. doi: 10.1021/acs.chemmater.6b02726.

[80] Y. Homma. Iiiv growth, in situ observation by scanning electron microscopy of. In K.H. Jrgen Buschow, Robert W. Cahn, Merton C. Flemings, Bernhard Ilschner, Edward J. Kramer, Subhash Mahajan, and Patrick Veyssire, editors, *Encyclopedia of Materials: Science and Technology*, pages 3678 – 3681. Elsevier, Oxford, 2001. ISBN 978-0-08-043152-9. doi: https://doi.org/10.1016/B0-08-043152-6/00656-2.

[81] David C. Joy. *Scanning Electron Microscopy*, chapter 3, pages 223–248. American Cancer Society, 2006. ISBN 9783527603978. doi: 10.1002/9783527603978.mst0012.

[82] Andy Connelly. Laboratory technique and science, bet surface area. *www.wordpress.com*, 10.05.2017. Assessed: 2019-05-10.

[83] Kenneth S. W. Sing, Douglas H. Everett, R. A. W. Haul, L. Moscou, Robert A. Pierotti, Jean Rouquerol, and Teresa Siemieniewska. *Reporting Physisorption Data for Gas/Solid Systems*, chapter 3.3.1, pages 1217–1230. American Cancer Society, 2008. ISBN 9783527610044. doi: 10.1002/9783527610044.hetcat0065.

[84] Gaurav Assat, Dominique Foix, Charles Delacourt, Antonella Iadecola, Rmi Dedryvre, and Jean-Marie Tarascon. Fundamental interplay between anionic/cationic redox governing the kinetics and thermodynamics of lithium-rich cathodes. *Nature Communications*, 8(1):2219, 2017. ISSN 2041-1723. doi: 10.1038/s41467-017-02291-9.

[85] Andreas Jossen. Fundamentals of battery dynamics. *Journal of Power Sources*, 154(2):530 – 538, 2006. ISSN 0378-7753. doi: https://doi.org/10.1016/j.jpowsour.2005.10.041. Selected papers from the Ninth Ulm Electrochemical Days.

[86] R Ferrero, Chao Wu, Alberto Carboni, Sergio Toscani, Marco De Angelis, Hindolo George-Williams, Edoardo Patelli, and Paolo Attilio Pegoraro. Low-cost battery monitoring by converter-based electrochemical impedance spectroscopy. *IEEE International Workshop on Applied Measurements for Power Systems (AMPS)*, pages 1–6, 09 2017. doi: 10.1109/AMPS.2017.8078334.

[87] Sigma aldrich, 2019. URL `https://www.sigmaaldrich.com/norway.html`. Accessed: 2019-04-25.

[88] Denis Y.W. Yu and Katsunori Yanagida. Structural analysis of li2mno3 and related li-mn-o materials. *Journal of The Electrochemical Society*, 158(9):A1015–A1022, 2011. doi: 10.1149/1.3609849.

[89] Prof. JungKi Park, editor. *Cathode Materials*, chapter 3, pages 21–87. John Wiley & Sons, Ltd, 2012. ISBN 9783527650408. doi: 10.1002/9783527650408.ch3.

[90] Huaquan Lu, Haitao Zhou, Ann Mari Svensson, Anita Fossdal, Edel Sheridan, Shigang Lu, and Fride Vullum-Bruer. High capacity li[ni0.8co0.1mn0.1]o2 synthesized by solgel and co-precipitation methods as cathode materials for lithium-ion batteries. *Solid State Ionics*, 249-250:105 – 111, 2013. ISSN 0167-2738. doi: https://doi.org/10.1016/j.ssi.2013.07.023.

[91] G. G. Wang, J. M. Wang, W. Q. Mao, H. B. Shao, J. Q. Zhang, and C. N. Cao. Physical properties and electrochemical performance of limn2o4 cathode materials prepared by a precipitation method. *Journal of Solid State Electrochemistry*, 9(7): 524–530, Jul 2005. ISSN 1433-0768. doi: 10.1007/s10008-004-0607-9.

[92] Maurice Cary Powers. A new roundness scale for sedimentary particles. *Journal of Sedimentary Research*, 23(2):117–119, 06 1953. ISSN 1527-1404. doi: 10.1306/D4269567-2B26-11D7-8648000102C1865D.

[93] Kaoru Miura, Atsuo Yamada, and Masahiro Tanaka. Electric states of spinel lixmn2o4 as a cathode of the rechargeable battery. *Electrochimica Acta*, 41(2):249 – 256, 1996. ISSN 0013-4686. doi: https://doi.org/10.1016/0013-4686(95)00304-W.

[94] Pouyan Shafiei Sabet and Dirk Uwe Sauer. Separation of predominant processes in electrochemical impedance spectra of lithium-ion batteries with nickel-manganese-cobalt cathodes. *Journal of Power Sources*, 425:121 – 129, 2019. ISSN 0378-7753. doi: https://doi.org/10.1016/j.jpowsour.2019.03.068.

[95] Fabio Rosciano, Jean-Franois Colin, Fabio La Mantia, Nicolas Tran, and Petr Novk. Electrochemical stress at high potential to investigate phase transitions in li1.1(ni1/3mn1/3co1/3)0.9o2. *Electrochemical and Solid-State Letters*, 12(7): A140–A144, 2009. doi: 10.1149/1.3130042.

[96] Zeshan Hu, Gerko Oskam, R. Lee Penn, Noshir Pesika, and Peter C. Searson. The influence of anion on the coarsening kinetics of zno nanoparticles. *The Journal of Physical Chemistry B*, 107(14):3124–3130, 2003. doi: 10.1021/jp020580h.

[97] R Hanafusa, K Kotani, K Ishidzu, Yoshihiro Oka, and T Nakamura. Electrochemical study of limn1.5ni0.5o4 spinel oxides prepared by two-step process. *Solid State Ionics*, 288, 02 2016. doi: 10.1016/j.ssi.2016.01.037.

[98] S. Grugeon, S. Laruelle, R. Herrera-Urbina, L. Dupont, P. Poizot, and J-M. Tarascon. Particle size effects on the electrochemical performance of copper oxides toward lithium. *Journal of The Electrochemical Society*, 148(4):A285–A292, 2001. doi: 10.1149/1.1353566.

[99] Ling jun LI, Xin hai LI, Zhi xing WANG, Ling WU, Jun chao ZHENG, and Jin hui LI. Synthesis of lini0.8co0.1mn0.1o2 cathode material by chloride co-precipitation method. *Transactions of Nonferrous Metals Society of China*, 20:s279 – s282, 2010. ISSN 1003-6326. doi: https://doi.org/10.1016/S1003-6326(10)60056-8.

[100] Xingde Xiang, James C. Knight, Weishan Li, and Arumugam Manthiram. Understanding the influence of composition and synthesis temperature on oxygen loss, reversible capacity, and electrochemical behavior of xli2mno3-(1 x)licoo2 cathodes in the first cycle. *The Journal of Physical Chemistry C*, 118(41):23553–23558, 2014. doi: 10.1021/jp507687h.

[101] Yuichi Itou and Yoshio Ukyo. Performance of linicoo2 materials for advanced lithium-ion batteries. *Journal of Power Sources*, 146(1):39 – 44, 2005. ISSN 0378-7753. doi: https://doi.org/10.1016/j.jpowsour.2005.03.091. Selected papers pressented at the 12th International Meeting on Lithium Batteries.

[102] Xun-Li Wang, Ke An, Lu Cai, Zhili Feng, Stephen Nagler, Claus Daniel, Kevin Rhodes, Alexandru Stoica, Harley Skorpenske, Chengdu Liang, Wei Zhang, Joon Kim, Yue Qi, and Stephen Harris. Visualizing the chemistry and structure dynamics in lithium-ion batteries by in-situ neutron diffraction. *Scientific reports*, 2:747, 10 2012. doi: 10.1038/srep00747.

[103] Ping-Chun Tsai, Bohua Wen, Mark Wolfman, Min-Ju Choe, Menghsuan Sam Pan, Liang Su, Katsuyo Thornton, Jordi Cabana, and Yet-Ming Chiang. Single-particle measurements of electrochemical kinetics in nmc and nca cathodes for li-ion batteries. *Energy Environ. Sci.*, 11:860–871, 2018. doi: 10.1039/C8EE00001H.

[104] Markus Klinsmann, Daniele Rosato, Marc Kamlah, and Robert M. McMeeking. Modeling crack growth during li extraction in storage particles using a fracture phase field approach. *Journal of The Electrochemical Society*, 163(2):A102–A118, 2016. doi: 10.1149/2.0281602jes.

[105] Qina Sa, Joseph A. Heelan, Yuan Lu, Diran Apelian, and Yan Wang. Copper impurity effects on lini1/3mn1/3co1/3o2 cathode material. *ACS Applied Materials & Interfaces*, 7(37):20585–20590, 2015. doi: 10.1021/acsami.5b04426.

[106] Shaowei Chen. 2 - practical electrochemical cells. In Cynthia G. Zoski, editor, *Handbook of Electrochemistry*, pages 33 – 56. Elsevier, Amsterdam, 2007. ISBN 978-0-444-51958-0. doi: https://doi.org/10.1016/B978-044451958-0.50003-3.

[107] Justin C. Marble, Timothy Corley, M Conklin, and Christopher Fuller. Environmental factors affecting oxidation of manganese in pinal creek, arizona. *Environmental Factors Affecting Oxidation of Manganese in Pinal Creek, Arizona*, 99, 01 1999.

[108] H.D. Deshazer, F. La Mantia, C. Wessells, R.A. Huggins, and Y. Cui. Synthesis of nanoscale lithium-ion battery cathode materials using a porous polymer precursor method. *Journal of The Electrochemical Society*, 158(10):A1079–A1082, 2011. doi: 10.1149/1.3611428. URL `http://jes.ecsdl.org/content/158/10/A1079.abstract`.

[109] R. C. Cope and Y. Podrazhansky. The art of battery charging. In *Fourteenth Annual Battery Conference on Applications and Advances. Proceedings of the Conference (Cat. No.99TH8371)*, pages 233–235, Jan 1999. doi: 10.1109/BCAA.1999.795996.

[110] Jiajun Chen, Shijun Wang, and M. Stanley Whittingham. Hydrothermal synthesis of cathode materials. *Journal of Power Sources*, 174(2):442 – 448, 2007. ISSN 0378-7753. doi: https://doi.org/10.1016/j.jpowsour.2007.06.189. 13th International Meeting on Lithium Batteries.

[111] Binhua Huang, Kun Qian, Yuxiu Liu, Dongqing Liu, Kai Zhou, Feiyu Kang, and Baohua Li. Investigations on the surface degradation of lini1/3co1/3mn1/3o2 after storage. *ACS Sustainable Chemistry & Engineering*, 7(7):7378–7385, 2019. doi: 10.1021/acssuschemeng.9b00621.

[112] Brian H. Toby. R factors in rietveld analysis: How good is good enough? *Powder Diffraction*, 21(1):6770, 2006. doi: 10.1154/1.2179804.

# Appendix A

# Classification of results

The following section contain the supplemental information.

The table used for classification of roundness, angularity and sphericity adapted from [73] is shown in figure A.1.

**Table A.1:** The PDF number, chemical formula, space group and lattice system of the references used for XRD scans.

| **Sample** | **PFD number** | **Formula** | **Space Group** | **Lattice System** |
|---|---|---|---|---|
| NMC111 phase | 04-013-4377 | $LiMn_{1/3}Co_{1/3}Ni_{1/3}O_2$ | $R\overline{3}m$ (166) | Rombo.H.axes |
| Spinel phase | 04-013-0104 | $LiMn_{1.4}\ Co_{0.6}O_4$ | $Fd\overline{3}m$ (227) | Cubic |
| Secondary phase | 04-010-5519 | $Li(NO_3)$ | $R\overline{3}c$ (167) | Rombo.H.axes |
| | 00-017-0510 | $MnO_2$ | I41/m (87) | Tetragonal |
| | 00-001-1127 | $Mn_3O_4$ | I41/amd (141) | Tetragonal |
| | 04-013-8970 | $Li_2\ MnO_3$ | C2/m (12) | Monoclinic |

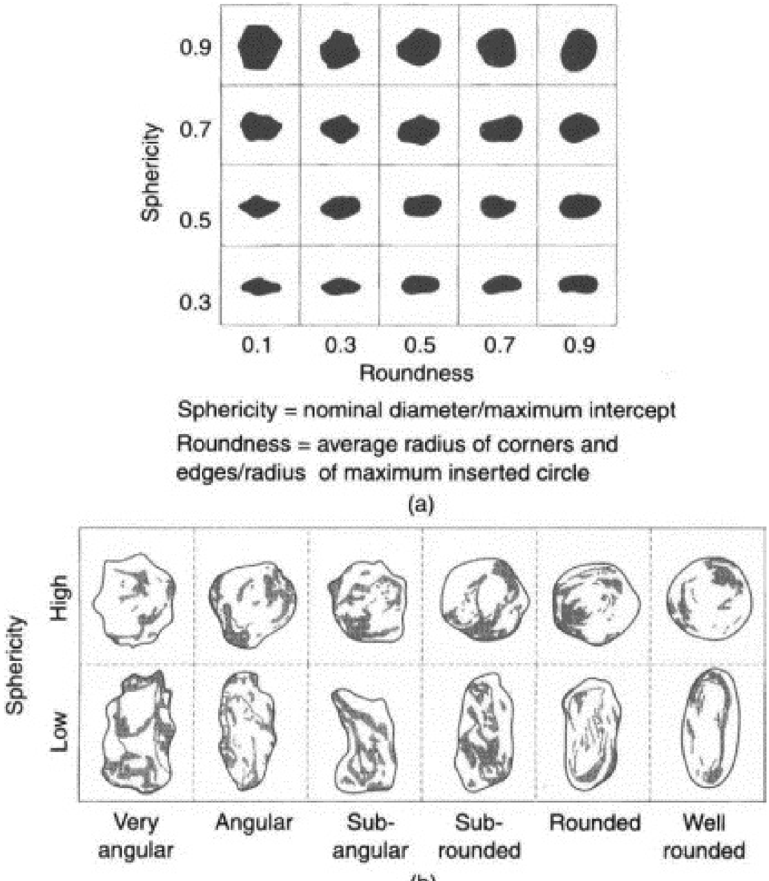

**Figure A.1:** A table showing how to classify particles a) sphericity and roundness and b) sphericity and angularity.

# Appendix B

# Additional results

The B.1 shows the XRD patterns of Air_Cl_HighPLi test 2 and 3 before and after heat treatment. Powders with the same synthesis method as Air_Cl_HighPLi, but with higher temperatures to obtain the high pressure of Li reaction in the autoclave. The temperatures of 160 °C (Air_Cl$_{\#3}$) and 175 °C (Air_Cl$_{\#2}$) were used. A spinel phase, like the one observed in the Air_Cl_HighPLi, is obtained. It is clear that Li reaction does not fully occur during the hydrothermal step at 160 and 175 °C.

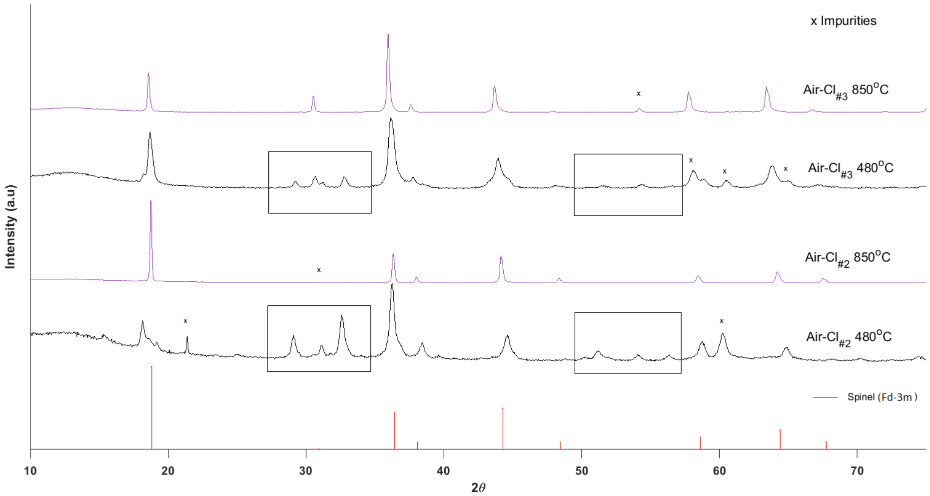

**Figure B.1:** Air_Cl_HighPLi 2 and 3 before and after heat-treatment. The boxes shows the presence of large impurities before the 850 °C heat treatment. After the heat treatment, a spinel phase is obtained.

The cycling data parallel to Inert_Cl and Inert_Aq:

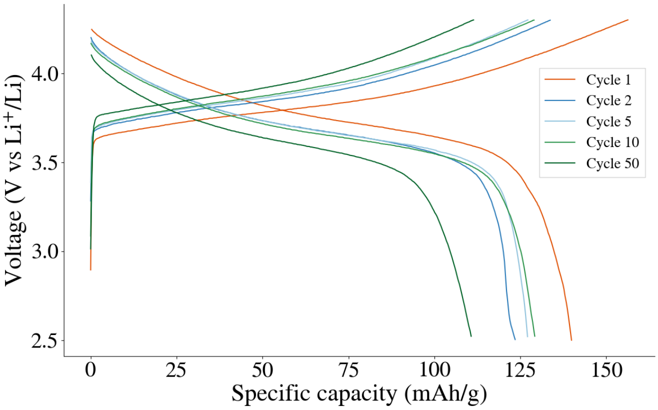

**Figure B.2:** The cycling data from a synthesis route identical to Inert_Aq. Another two coin-cells from this batch showed similar results. The discharge capacity falls from 140 to 111 mAh/g from 1st to 50th cycle.

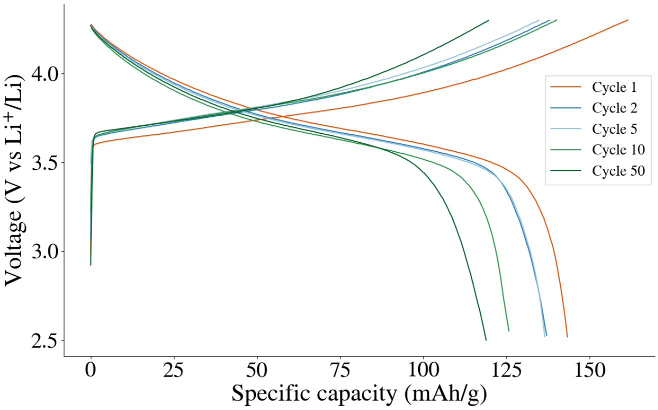

**Figure B.3:** Cycling data from a synthesis route identical to Inert_Cl. Another two coin-cells from this batch showed similar results.

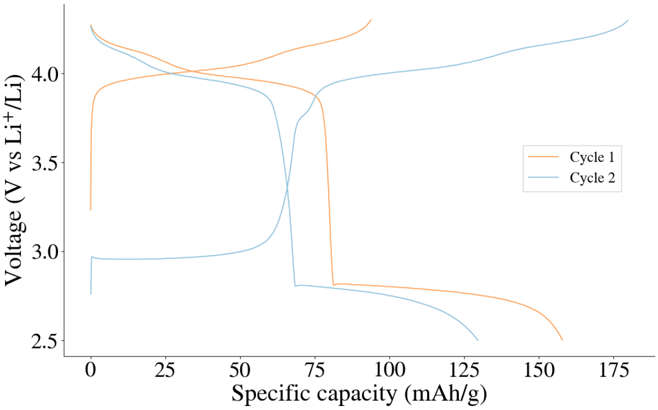

**Figure B.4:** Air_Aq_HighPLi coin cell 1. It has the distinct spinel-shaped charge/discharge curves. The sample fails in 3rd cycle.

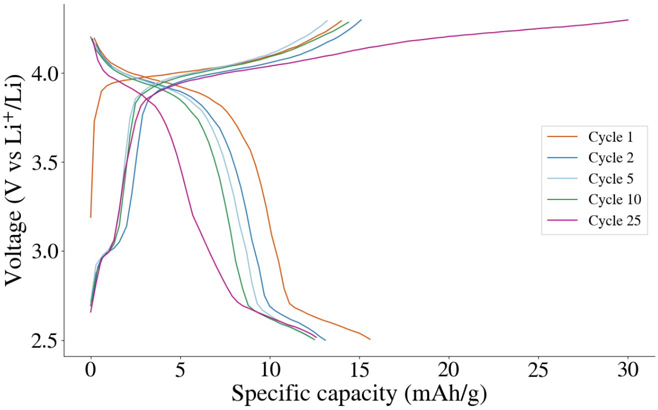

**Figure B.5:** Sample Air_Aq coin cell 2. The cycling data from the synthesis route that deviate from Air_Cl with using Aq-precursors. Initial charge capacity is at 15 mAh/g, and decreases to 12 mAh/g after 25 cycles. The charge capacity reaches $\sim$ 1307 after cycle 26, followed by a total cell failure.

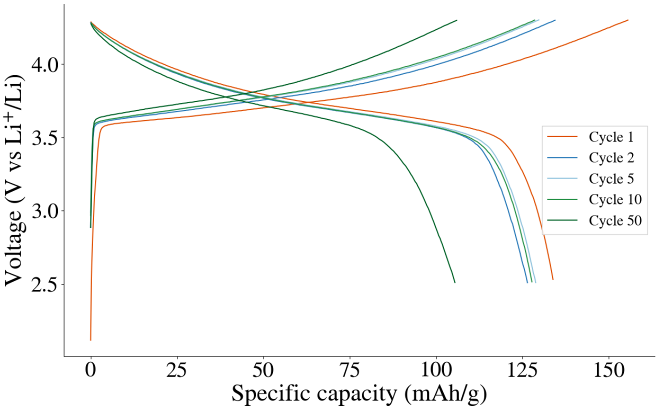

**Figure B.6:** Sample Inert_Cl parallel 3. The cell deviate from parallel 1 and 2 by having a faster decrease in specific discharge capacity, going from 134 to 106 mAh/h after 50 cycles.

NTNU
Norwegian University of
Science and Technology